

Figure 4.1. Description of motion

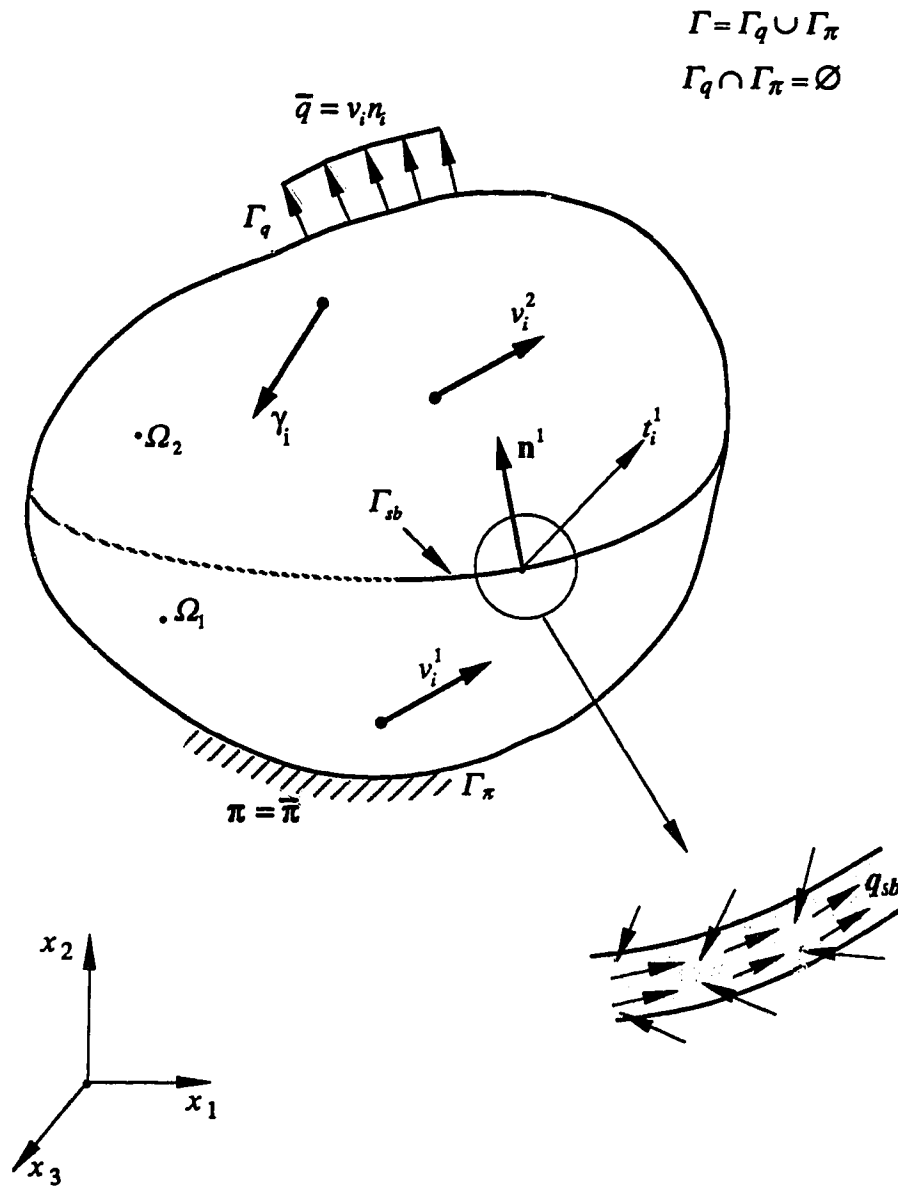


Figure 4.2. Fluid flow through discontinuous medium

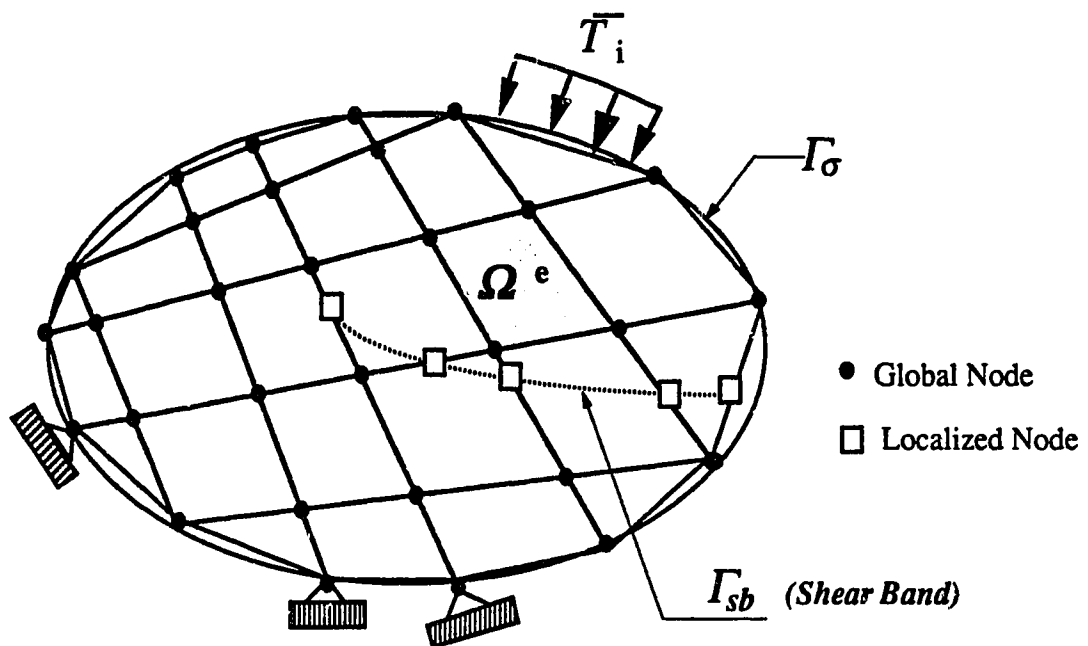


Figure 4.3 Finite element discretization of domain

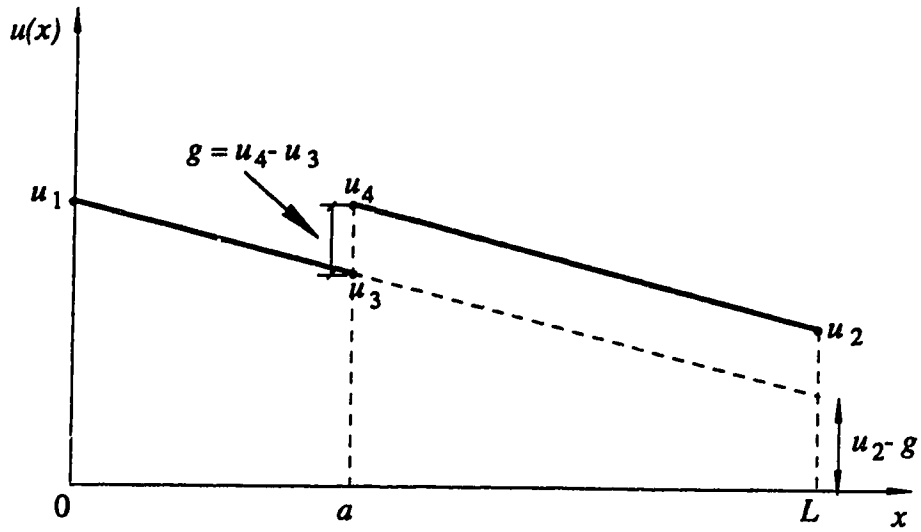


Figure 4.4a. 1-D discontinuous interpolation function

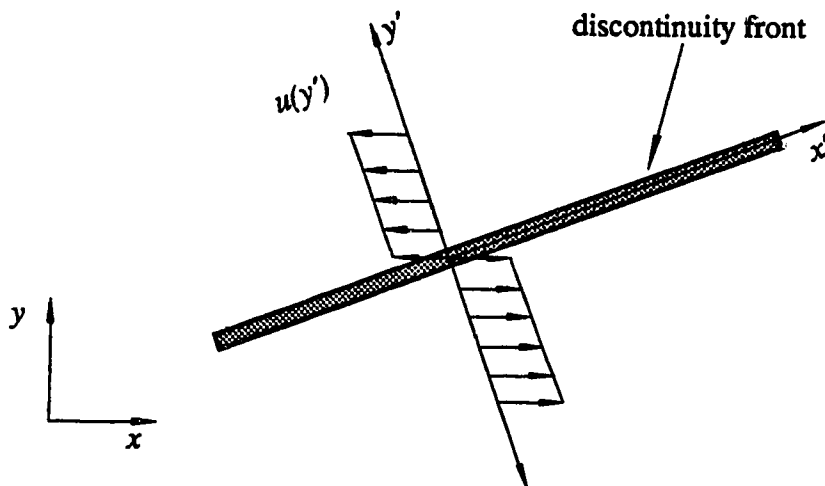
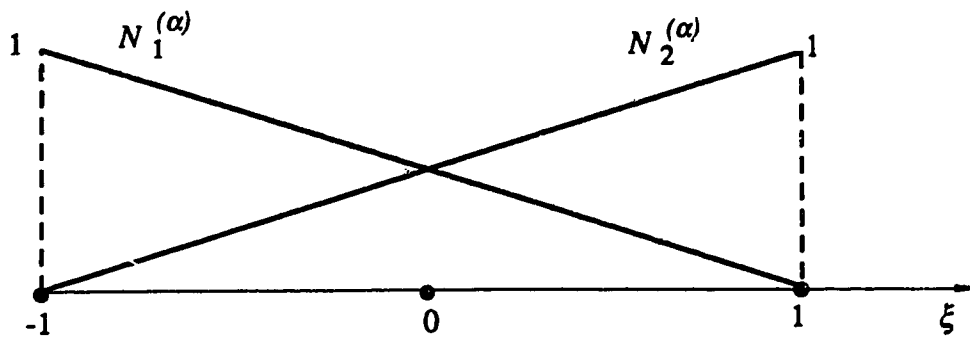


Figure 4.4b. Distribution of displacement across a shear band

Continuous interpolation function $N^{(\alpha)}$



Discontinuous interpolation function $N^{(\beta)}$

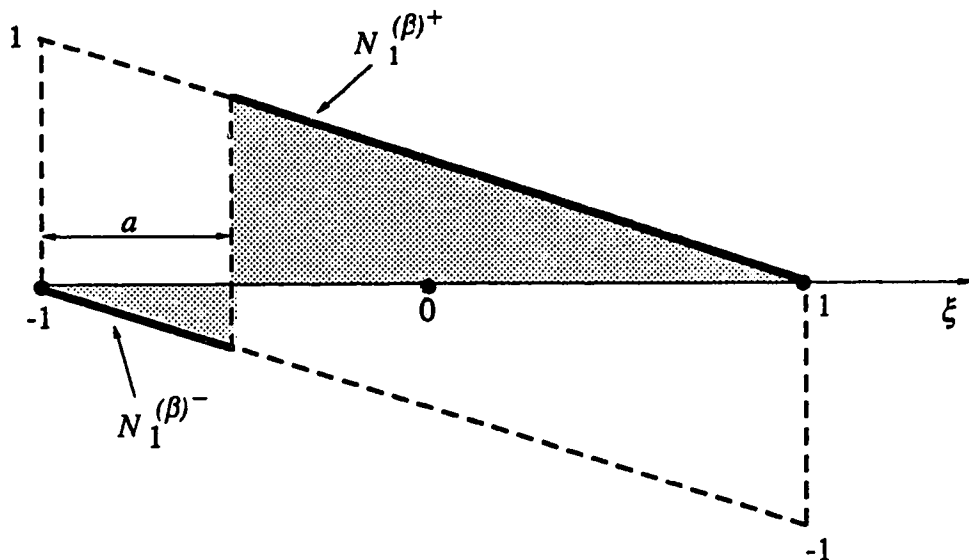


Figure 4.5 Geometrical description of 1-D discontinuous interpolation shape functions

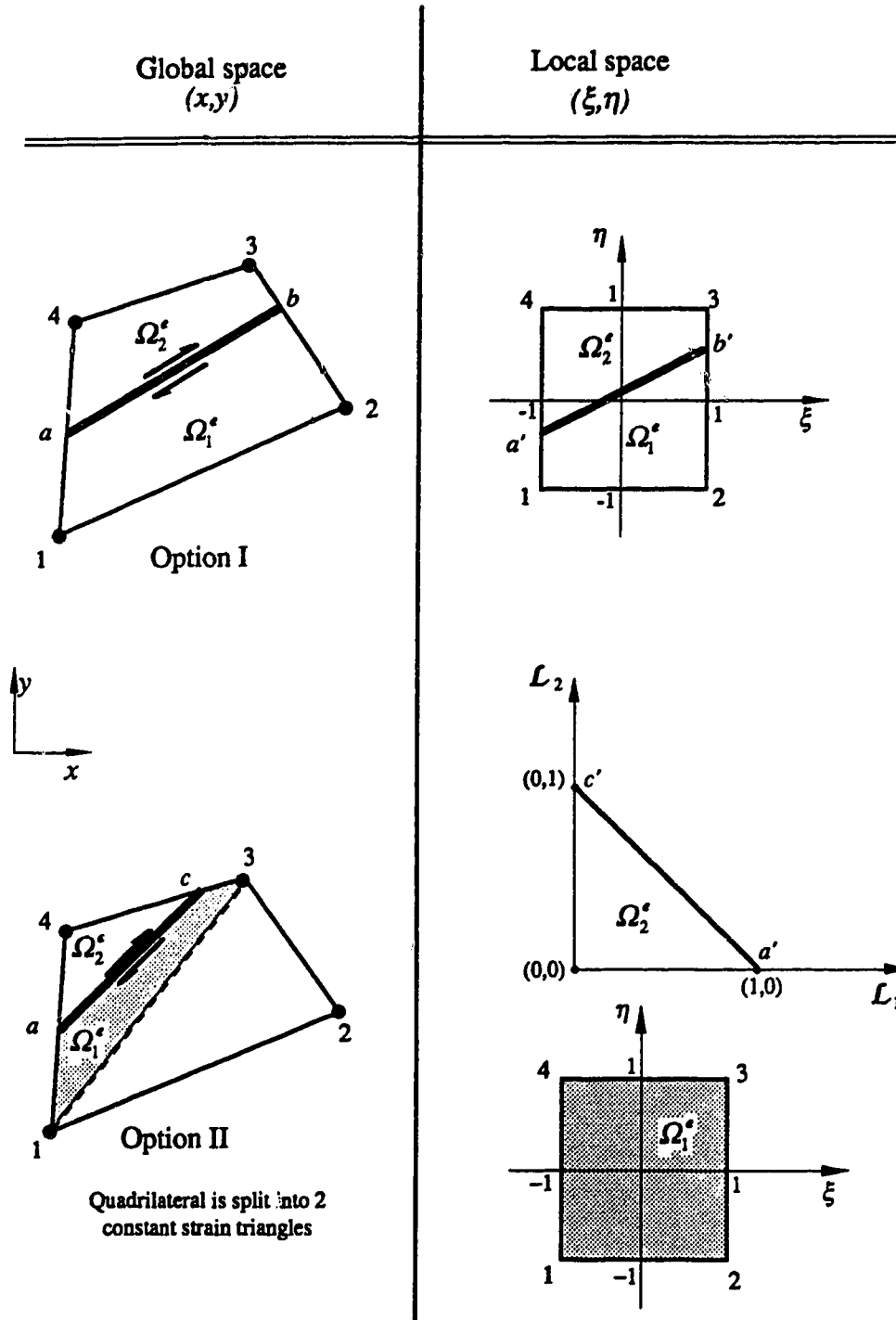
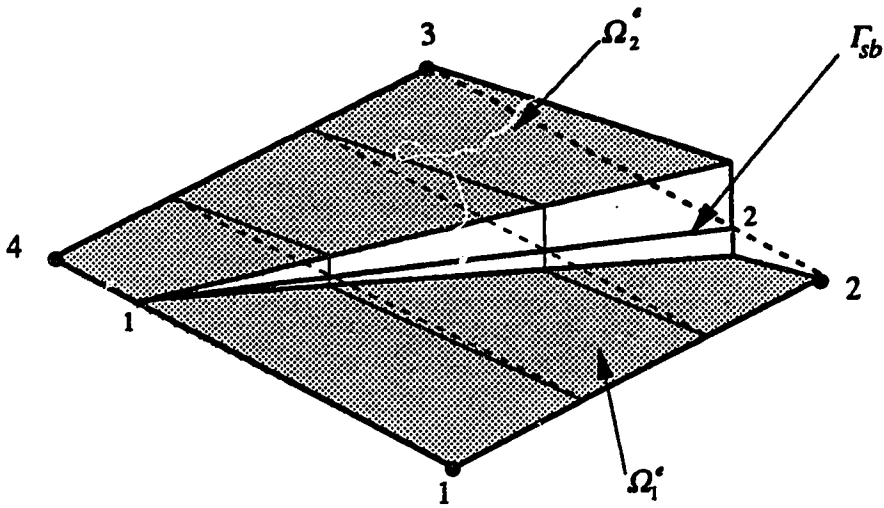
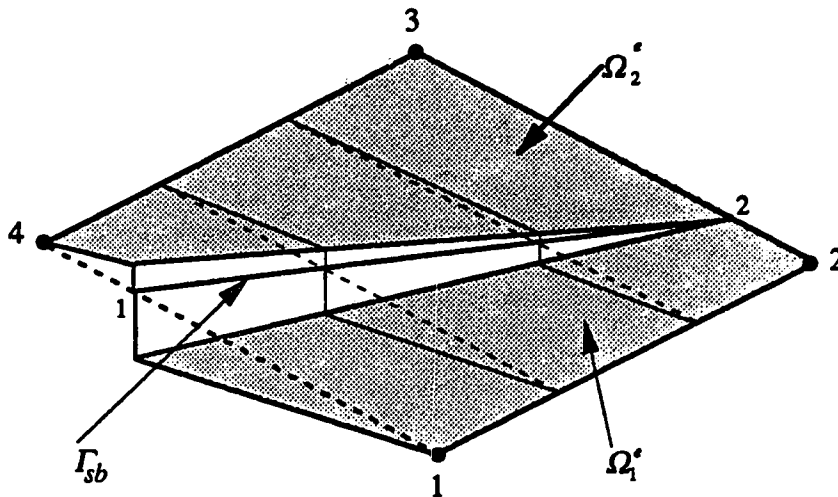


Figure 4.6 Master element configurations for QD4 elements



$$\text{for } (\xi, \eta) \in \Gamma_{sb}^+ \quad N_2^{(\beta)+} = \frac{1}{4}(1-\eta)(1+\xi)$$

$$\text{for } (\xi, \eta) \in \Gamma_{sb}^- \quad N_2^{(\beta)-} = -\frac{1}{4}(1+\eta)(1+\xi)$$



$$\text{for } (\xi, \eta) \in \Gamma_{sb}^+ \quad N_1^{(\beta)+} = \frac{1}{4}(1-\eta)(1-\xi)$$

$$\text{for } (\xi, \eta) \in \Gamma_{sb}^- \quad N_1^{(\beta)-} = -\frac{1}{4}(1+\eta)(1-\xi)$$

Figure 4.7 Discontinuous shape functions for a 4-node quadrilateral element

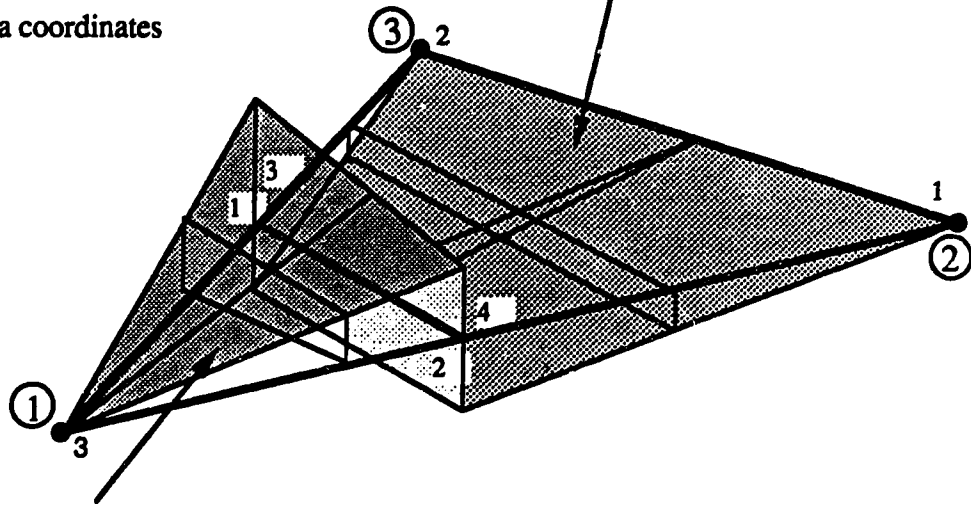
λ_a and λ_b define the intersection locations of the band with element edges

Domain I Ω_1^e

$$N_1^{(\beta)} = (\lambda_a - 1)N_1$$

$$N_2^{(\beta)} = (\lambda_b - 1)N_4$$

L_i area coordinates



Domain II Ω_2^e

$$N_1^{(\beta)} = L_2 \lambda_a$$

$$N_2^{(\beta)} = L_3 \lambda_b$$

$$N_1 = \frac{1}{4}(1 - \xi)(1 - \eta)$$

$$N_4 = \frac{1}{4}(1 - \xi)(1 + \eta)$$

Figure 4.8 Discontinuous Interpolation Function for a 3-node Triangular Element

Chapter 5

Constitutive Relationships

5.1. Preliminary Considerations

It is of main concern to determine the laws that govern the local deformation response of the shear band. Fully developed plastic shear flow is considered and it can be regarded from the continuum stand-point as a plane simple shear flow if the scale of investigation is large compared with the characteristic length of the granular structure. Geometrically speaking, this kind of plastic shear flow can be visualized as the sliding of a set of infinitesimally close planes taking place inside a band of material. According to the scale of investigation, this simple shearing may not be continuous, and suffer discontinuity jumps across a shear plane. If the band is considered as a shear plane, the discontinuity will be rather described by a displacement jump. On the other hand for a relatively thick band, the same discontinuity may be regarded as a weak type, i.e. a jump in the gradient of displacement across the thickness of the band, see Figure 5.1.

From a macroscopic stand-point, the fully developed shear flow translates into paths along which grains over-ride each other over infinite distances; these paths undulate in a random manner about macroscopic shear planes. When considering a macroscopic shear plane element ss in Figure 5.1, it is possible at any instant to associate it with a wavy surface element $s's'$. In other words, the discontinuous shearing on a characteristic

sliding plane will be the limit which a continuous shear flow approaches when the width of the shear zone is made to vanish.

It is appropriate at this point to regard the shear flow phenomenon as a contact friction interaction problem. The oldest and most popular idealization for friction is due to Coulomb. Although originally postulated for contact between dissimilar rigid bodies, it may have an analogous interpretation for contact between deformable similar bodies. It can be stated that the relative motion between two adjacent points in contact will occur whenever the tangential stress attains a value equal in magnitude to the normal compressive stress multiplied by some constant called the friction coefficient which characterizes the interface. Furthermore, it requires the relative tangential motion to be zero prior to frictional slip. However in the case of geomaterials, considerable experimental evidence shows that reversible tangential displacements take place prior to any permanent frictional sliding. This appears specially in rock joints problems, see Rosso [1976].

5.2. Rupture interface rheology

The shear band is visualized as a zone of the soil body within which large structural changes, in the form of either grain crushing or re-orientation, take place during localized shearing. Furthermore, the surfaces demarcating the localized zone are considered planar and parallel to each other separated by a distance which is a function of the grain size of the material. As such the thickness of the band will generally be very small, and typically of the order of 10 to 20 times the mean diameter of the soil grains for granular materials.

5.2.1 Experimental observations

In order to investigate the constitutive behaviour of the shear band, an experiment has to be devised in which the band is allowed to form freely without any kinematic restraint so that one ensures measuring only the mechanical properties of the band just as if it were isolated. A very simple arrangement is the direct shear box apparatus, but there has been much

controversy upon its validity, and interpretation of test results. It is well known that the state of stress is far from being uniform inside the box due to stress concentrations at the edges. As a result, the shear strength is not uniformly mobilized inside the specimen so that the measured stresses can only be considered on an average sense. Figure 5.2 illustrates the initiation of rupture surfaces at the two opposite ends of the box due to progressive failure, and amazingly enough, they are not found to be horizontal in the direction of the physical plane of shearing. Kink bands are initially formed and have been observed by Morgenstern and Tchalenko [1967] who investigated the microscopic characteristics of shear banding in a Kaolin specimen subjected to direct shear. As the loading process progresses towards higher shearing, those microscopic features coalesce and make way to a shear band in the horizontal direction as a result of principal stress rotation, large deformation and improvement of kinematic constraints. In this situation the mobilized shear strength is fairly uniform along the shear band since at each material point, it may be considered that the residual strength has been reached. The relative sliding between the top box and the bottom one, then approximately represents the global behaviour of the shear band along with surrounding material in a rigid passive stress state.

The transition from the two states described is made through a rapid drop of the shear strength from a peak value to a residual one, see Figure 5.3. The rate of drop in strength, or softening rate which one measures depends on many factors. Firstly, due to the non-uniform mobilization of shear stresses along the band, the stress-relative displacement curve will not be unique for any material point. Secondly, the rate of softening will be function of the grain size, thickness of the band and the size of the box as well.

In order to obtain a reasonable representation of the behaviour of the shear band in an experimental device, the end effects errors introduced must be eliminated. It would be convenient to have an infinitely long shear box: a close approximation of it being the ring shear apparatus, see Yoshimi and Kishida [1981]. In this device, the problems caused by

non-uniformity of stress distribution are reduced, but freedom of formation of the shear band is somewhat restricted. However, the stress-relative displacement behaviour in the post-peak range will be obtained within a higher degree of accuracy than can be reached by the direct shear box.

Both the direct shear box and the ring shear tests can be regarded as a surface element test, the dual form of a volume element test. At this scale of investigation, both stress and strain can be viewed as homogeneous along the idealized displacement discontinuity surface. Due to kinematic constraints, the macroscopic shear band does not change configuration and stays horizontal, i.e. the direction of imposed shearing. Several experiments, for example *x*-ray photographs taken in a large shear box confirm this observation, see Scarpelli and Wood [1982]. However, one has to be careful in dealing with the extent of non-homogeneity in the vicinity of the shear band. Although the stress and strain fields can be considered homogeneous along the shear band interface, they may not be so inside it.

5.3 Formulation of stress-relative displacement relationship

The deformational properties of the shear band are in general different from those of a material undergoing general 3-D deformation. This implies that although a constitutive model may be valid for general continuum behaviour, its validity may need analysis and investigation when specialized into shear band behaviour. For instance characterization of large structural changes and dilation inside a shear band may be different from those occurring in a body undergoing general deformation.

Figure 5.4 illustrates the generic shear band problem specialized into a two dimensional configuration. The simple situation involving a shear band parallel to the *x*-*z* plane with normal and shear stresses acting on the surface is considered. Also the stress and strain fields are assumed homogeneous in the *x*-*y* plane and no deformation is allowed

in the z direction. A relationship linking the loading vector, herein boundary stresses $\{\sigma_n, \tau\}$ defined on an average sense, to the response vector which contains the boundary relative normal and tangential slip displacements $\{g_n, g_t\}$ is sought. Mathematically, a functional depending on stresses, relative slip displacements and associated state variables such as density and void ratio must be formulated. A pragmatic approach is herein adopted whereby the functional ideally lumps all variables which may contribute to complex phenomena such as grain crushing, large displacements and distortions and rotations. Thus, ideally

$$\mathcal{F}(\sigma_n, \tau, g_n, g_t, \rho_0, n, \dots) = 0. \quad (5.1)$$

The symbol '.....' refers to other variables that need to be accounted for, see Malvern[1969], based on the *Principle of Equipresence*, which requires that all variables that could possibly influence the response of the shear band be incorporated in \mathcal{F} . In precise terms, \mathcal{F} represents a contact constitutive relationship. Due to the non-linear nature of the problem, an incremental formulation which relates tangential response to tangential load is preferably chosen. Also for simplicity of the formulation, a non-viscous behaviour is considered such that \mathcal{F} is made a homogeneous function of order 1.

There are basically several approaches to determine \mathcal{F} , either by fitting experimental data using sophisticated mathematical techniques, or advocating the classical plasticity formalism. The coming sections will basically review and hence assess the two different approaches in view of applying them to the shear band problem.

5.3.1 Phenomenological approaches

In the phenomenological approach adopted by Ichikawa[1985] for modelling continuum constitutive behaviour, the loading vector is expressed by means of a response functional covering the spectrum of all possible field variables and loading paths. The concept can be

similarly applied to the shear band by postulating the stresses at the limiting boundaries to be solely function of slip displacements. As such, the response of the stress normal to the shear plane is made function of normal slip displacements, and to a lesser degree tangential slip displacements. On the other hand, tangential slip displacements will be the predominant factor governing the shear stress response. This can be mathematically written as:

$$\sigma_n = \Phi(g_n^p, g_t^p) \text{ and } \tau = \Psi(g_t^p, g_n^p), \quad (5.2)$$

in which Ψ and Φ are the response functions to be experimentally determined from fitting and spectrum techniques. Note that superscript 'p' in Eq. (5.2) stands for plastic or irrecoverable component of slip displacement. The incremental form of Eq. (5.2) obtained by simple differentiation thus leads to the stress-slip displacement relationship. However, the difficulty of the formulation lies in the proper determination of Ψ and Φ through experiments. This requires considerable data and mathematical fitting techniques such as spectrum analysis of functions in order to arrive at the final form of the functionals.

Alternatively, the processes characterizing the shear band can be conveniently cast into the framework of damage theory. Damage theory has been recently used in engineering mechanics and is a fairly well established, see Chaboche[1981]. In the same context, the shear force along the boundaries of a shear band of finite thickness can be made to originate from two contributing sources, namely one due to purely frictional effects and the other one due to the extent of damage, i.e grain crushing, particle reorientation and micro-cracking inside the band. This leads to partitioning the contact surface area into frictional and damage components. The frictional component is described by a classical Coulomb law while damage is given by a convenient evolution law. The determination of driving parameters requires very sophisticated experimental techniques. It is usually difficult to experimentally follow the evolution of damage, and hence the mathematical relationship. Consequently, a

damage based formulation will not be contemplated in the present analysis, and as a matter of fact, is not justified.

5.4 Plasticity formalism

In the present study the behaviour of the band can be completely described by means of the plasticity formalism. Both a yield surface and plastic potential are postulated. Softening effects and microfabric changes in the band can be macroscopically modelled by the expedient of making state variables such as mobilized band friction and cohesion degrade with accumulated plastic deformations.

Suppose the behaviour of the surface discontinuity formed by the band be governed by a conventional Coulomb contact law of the form

$$|\tau| = c_d(\gamma^p) - \sigma_n \tan \varphi_d(\gamma^p), \quad (5.3)$$

in which:

- φ_d = characteristic friction angle of discontinuity,
- c_d = characteristic cohesive strength of discontinuity, and
- γ^p = plastic distortion taking place at the discontinuity.

5.4.1 Contact yield and plastic potential functions

The Coulomb yield function can thus be conveniently written in the following alternate form:

$$F_d = \tau^2 - [c_d(\gamma^p) - \sigma_n \tan \varphi_d(\gamma^p)]^2 = 0. \quad (5.4)$$

The flow rule of plasticity requires the incremental plastic strain vectors $\dot{\epsilon}^p$ to be orthogonal to a plastic potential function. The plastic potential function can be formulated much in the

same fashion as in Eq. (5.4) by simply replacing the friction angle φ_d by a dilatancy angle ψ_d , and c_d by \bar{c}_d . Thus,

$$G_d = \tau^2 - [\bar{c}_d(\gamma^p) - \sigma_n \tan \psi_d(\gamma^p)]^2. \quad (5.5)$$

The incremental plastic strains are readily obtained from the flow rule

$$d\epsilon^p = d\lambda \frac{\partial G_d}{\partial \sigma}, \quad (5.6)$$

with $d\epsilon^p = \{d\epsilon_n^p, d\epsilon_{nt}^p\}$ and $\sigma = \{\sigma_n, \tau\}$ in the band local system (n, t) . It is noted that when the thickness of the shear band becomes small compared to the dimensions of the specimen, finite deformations within the shear band may develop and hence materially large deformation measures may be needed in Eq. (5.6).

It can be readily shown that defining the above flow rule leads to imposing a kinematic constraint to the normal slip displacement g_n^p and tangential slip displacement g_t^p , i.e.

$$\frac{dg_n^p}{dg_t^p} = s \tan \psi_d, \quad (5.7)$$

in which $s = -1$ if $\tau < 0$ and $s = 1$ if $\tau > 0$.

5.4.2 Evolution rule

The evolution of deformation inside the band—or at least in its neighbourhood—can be traced by making both friction angle φ_d and cohesion c_d become function of plastic distortion γ^p .

In plane strain conditions, the plastic distortion rate can be conveniently expressed by

$$\dot{\gamma}^p = \sqrt{2\dot{\boldsymbol{\epsilon}}:\dot{\boldsymbol{\epsilon}}}, \quad (5.8)$$

where the deviatoric strain rate $\dot{\boldsymbol{\epsilon}}$ is classically given as

$$\dot{\boldsymbol{\epsilon}} = \dot{\boldsymbol{\epsilon}} - \frac{1}{2}\text{trace}(\dot{\boldsymbol{\epsilon}})\mathbf{1}, \quad (5.9)$$

where in the special case of the simple 2-D band,

$$\text{trace}(\dot{\boldsymbol{\epsilon}}) = \dot{\epsilon}_{nn} + \dot{\epsilon}_{tt} \text{ and } \mathbf{1}_{ij}\mathbf{1}_{ij} = 2 \text{ since } i, j = 1, 2 \text{ (}\mathbf{1} \text{ is the Kronecker delta)}. \quad (5.10)$$

By virtue of the above, and considering that the t axis is a direction of zero extension ($\dot{\epsilon}_{tt} = 0$; pure shear), the plastic distortion simplifies into

$$\dot{\gamma}^p = \sqrt{(\dot{\epsilon}_{nn})^2 + 2(\dot{\epsilon}_{nt})^2}. \quad (5.11)$$

By making use of the shear band thickness d_b , the above in terms of slip displacement rates becomes

$$\dot{\gamma}^p = \frac{1}{d_b} [(\dot{g}_n^p)^2 + (\dot{g}_t^p)^2]^{1/2} = \frac{1}{d_b} \|\dot{\mathbf{g}}^p\|. \quad (5.12)$$

It is seen that the plastic distortion rate degenerates into the norm of the slip displacement vector for a point along the shearing plane.

5.4.3 Elasto-plastic contact constitutive tensor

In general, it can be considered that the deformation of the discontinuity (shear band) is only partially recoverable. As such,

$$d\mathbf{g} = d\mathbf{g}^e + d\mathbf{g}^p. \quad (5.13)$$

The following elasticity relations hold:

$$d\boldsymbol{\sigma} = \boldsymbol{\eta}^e : d\mathbf{g}^e, \quad (5.14)$$

where

$$\boldsymbol{\eta}^e = \begin{bmatrix} K_d & 0 \\ 0 & G_d \end{bmatrix}. \quad (5.15)$$

The parameters K_d and G_d are respectively elastic normal and shear moduli for the discontinuity.

The plastic slip displacements can be explicitly given by use of the alternate form of Eq. (5.5) and Eq. (5.6), i.e.

$$d\mathbf{g}_n^p = d_b \, d\lambda \tan \psi_d, \quad d\mathbf{g}_t^p = d_b \, d\lambda. \quad (5.16)$$

The consistency equation, i.e. $dF_d = 0$, ensures that the stress stays on the yield surface, in other words,

$$\frac{\partial F_d}{\partial \boldsymbol{\sigma}} : d\boldsymbol{\sigma} + \frac{\partial F_d}{\partial \gamma^p} : d\gamma^p = 0. \quad (5.17)$$

Replacing $d\gamma^p$ in the above with the aid of Eqs. (5.11) and (5.16) leads to the expression of the plastic multiplier $d\lambda$, i.e.

$$d\lambda = \frac{1}{H_d} \frac{\partial F_d}{\partial \boldsymbol{\sigma}} : d\boldsymbol{\sigma}, \quad (5.18)$$

in which the hardening modulus H_d is

$$H_d = -\frac{1}{\cos \psi_d} h_d; \quad h_d = \frac{\partial F_d}{\partial \gamma^p}. \quad (5.19)$$

It can be readily shown, that the enforcement of the above consistency leads to the classical rate-independent contact constitutive relation

$$\dot{\boldsymbol{\sigma}} \equiv \dot{\mathbf{t}} = \boldsymbol{\eta}^{sp} : \dot{\mathbf{g}}, \quad (5.20)$$

where $\boldsymbol{\eta}^{sp}$ is a second order tensor with the following expression

$$\boldsymbol{\eta}^{sp} = \frac{1}{d_b} \left[\boldsymbol{\eta}^e - \frac{\left(\boldsymbol{\eta}^e : \frac{\partial F_d}{\partial \boldsymbol{\sigma}} \right) \otimes \left(\frac{\partial G_d}{\partial \boldsymbol{\sigma}} : \boldsymbol{\eta}^e \right)}{H_d + \frac{\partial F_d}{\partial \boldsymbol{\sigma}} : \boldsymbol{\eta}^e : \frac{\partial G_d}{\partial \boldsymbol{\sigma}}} \right]. \quad (5.21)$$

\otimes denotes the tensor product in the sense that $(\mathbf{a} \otimes \mathbf{b})_{ijkl} = (\mathbf{a})_{ij}(\mathbf{b})_{kl}$.

The final explicit form of the above equation, in the special case of the 2-D planar shear band is

$$\boldsymbol{\eta}^{sp} = \frac{1}{d_b} \left\{ \begin{bmatrix} G_d & 0 \\ 0 & K_d \end{bmatrix} - \frac{1}{G_d + K_d \tan \varphi_d \tan \psi_d - h_d \sec^2 \psi_d} \begin{bmatrix} G_d^2 & sG_d K_d \tan \psi_d \\ sG_d K_d \tan \psi_d & K_d^2 \tan \psi_d \tan \varphi_d \end{bmatrix} \right\}. \quad (5.22)$$

In order to get some insight into the above expression, if h_d tends to infinity, the elastic constitutive tensor is recovered. For a purely cohesive shear band, it suffices to replace both friction and dilatancy angles by zero in the very general expression in Eq.(5.22).

The evaluation of the constitutive tensor $\boldsymbol{\eta}^{sp}$ depends explicitly on the shear band thickness d_b . In order to avoid the sensitivity to this dimension, which in fact cannot be

uniquely determined, the problem can be reformulated in terms of strain rates, i.e. the shear band is associated with a velocity discontinuity.

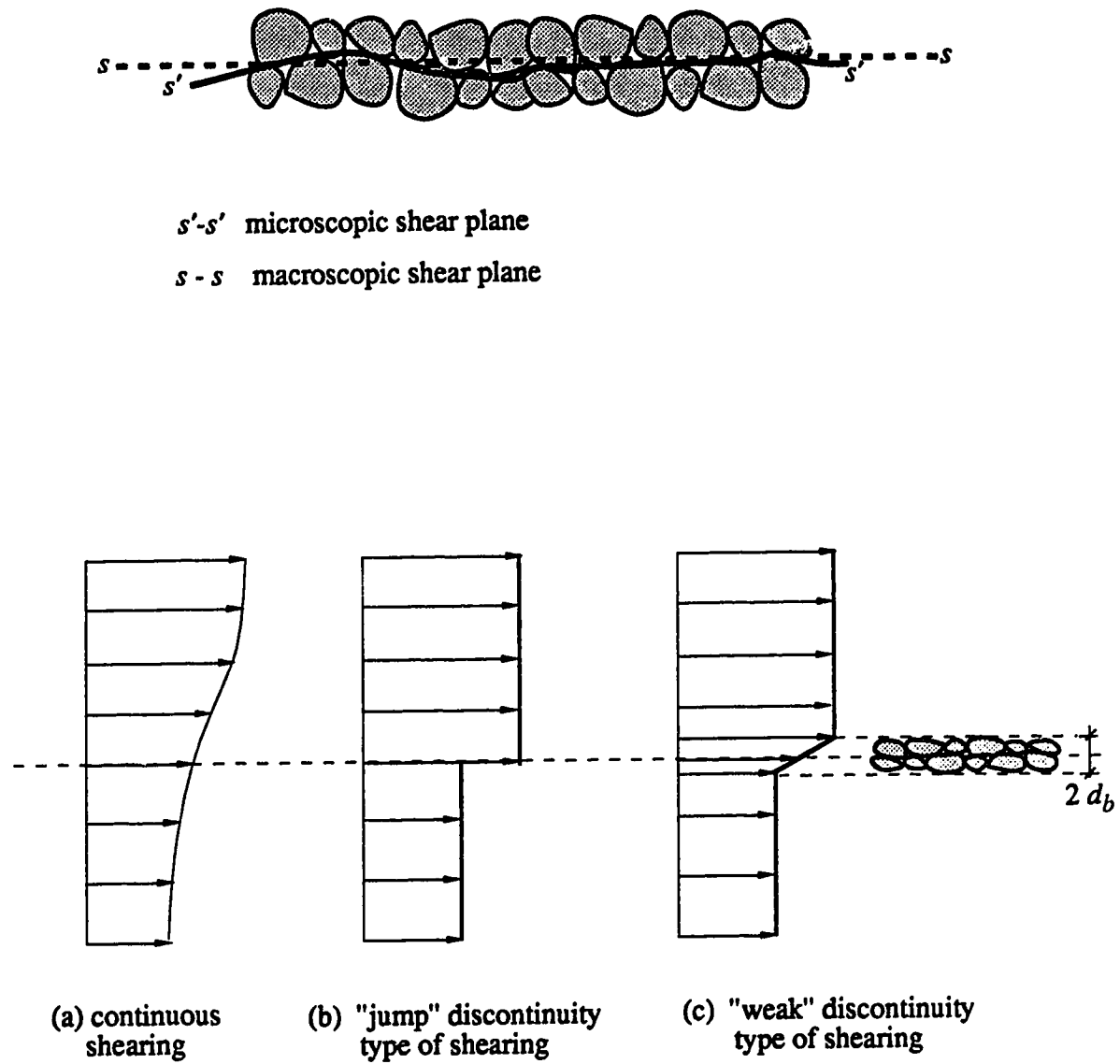


Figure 5.1 Macroscopic schematization of shear flow inside a shear band

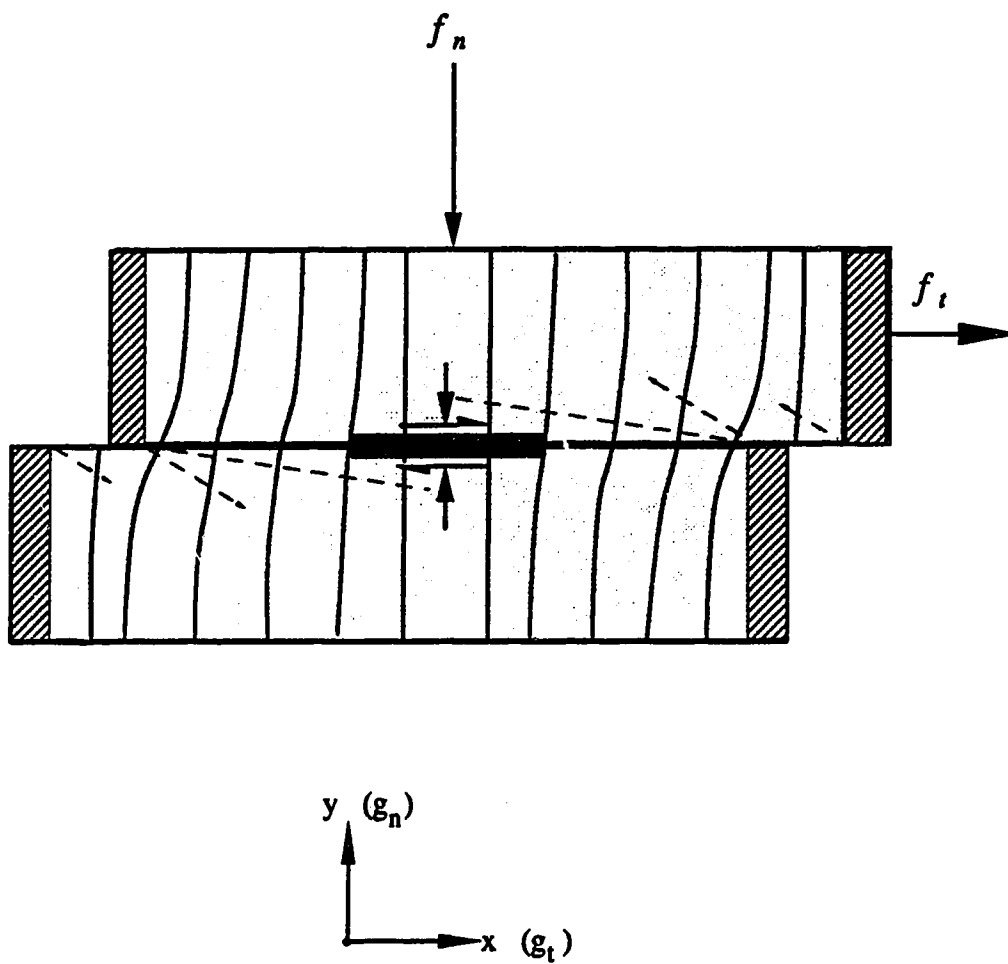


Figure 5.2 Non-uniform stress distribution inside a shear box: progressive failure

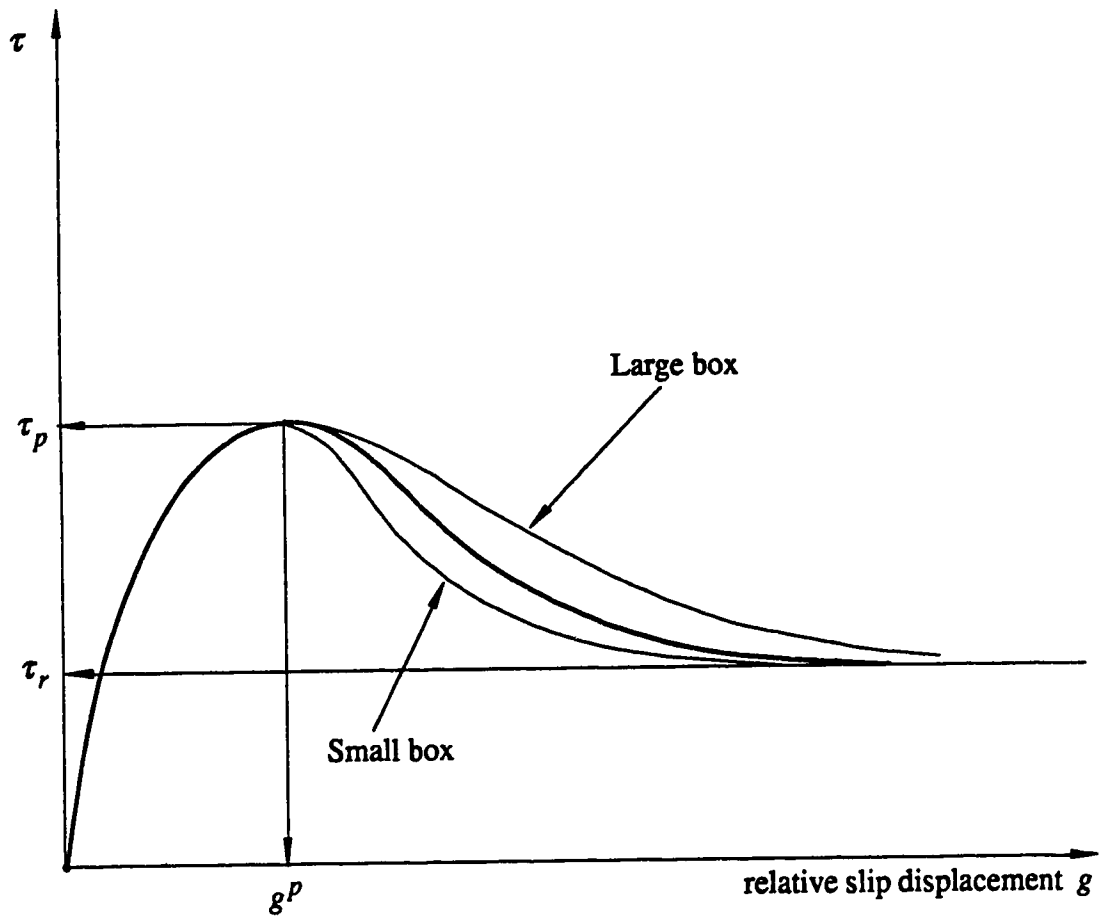


Figure 5.3 Stress-relative displacement relationship in a direct shear box

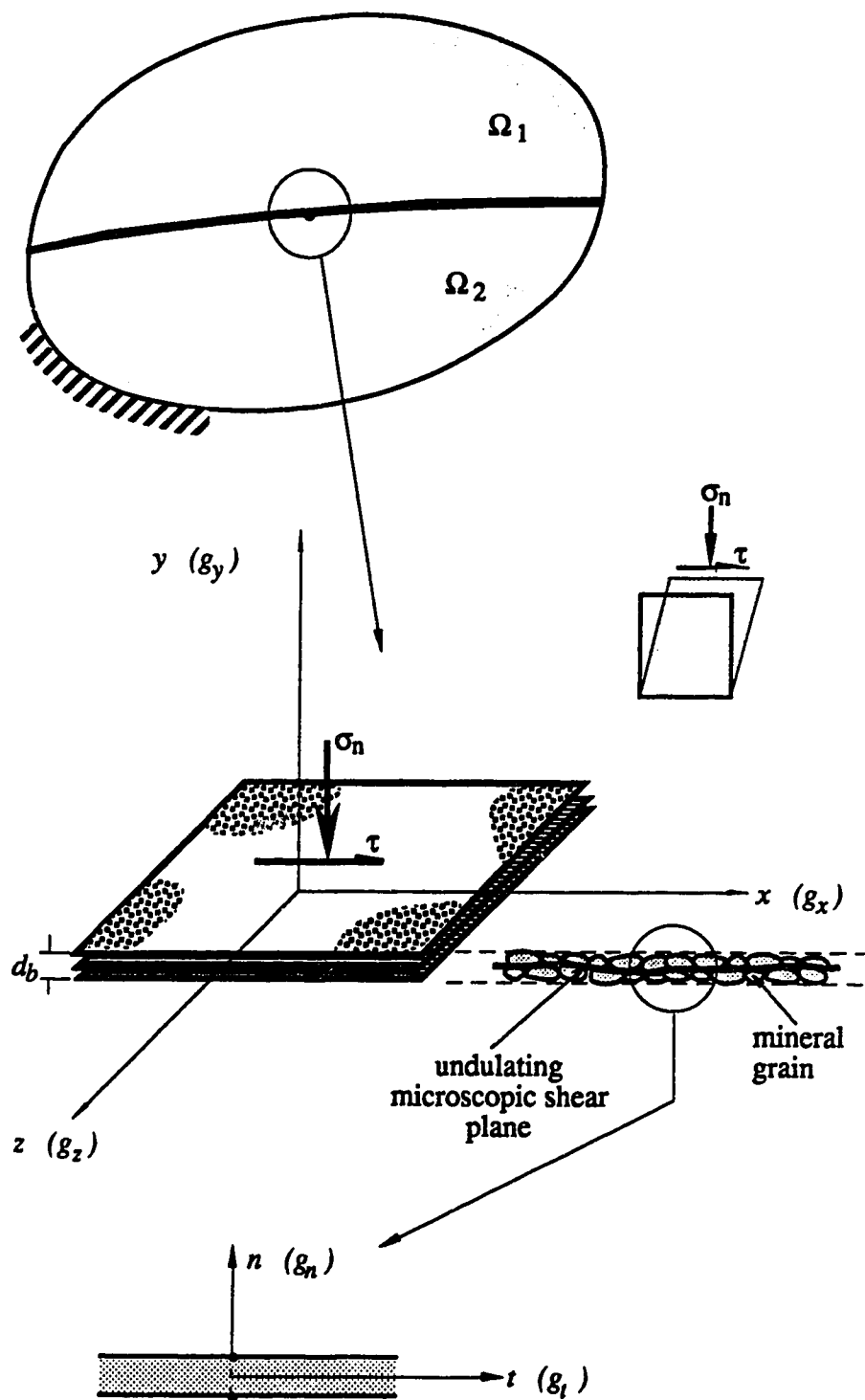


Figure 5.4 Generic representation of shear band in 2-D configuration

Chapter 6

Numerical Strategies

6.1. Introduction

The previous chapters laid the foundation for the establishment of a formalism for shear band inception, ensuing kinematics and basic laws governing its behaviour. In precise terms, it has been shown in Chapter 3, that bifurcation theory is appropriate for predicting localization. Chapter 4 goes on and demonstrates that important features, such as the discontinuous behaviour which arises during localization, can be incorporated into the theory by modifying the Principle of virtual work into an equivalent one for a body traversed by a discontinuity surface representing a shear band.

The pursuit of a finite element oriented framework has led to the design of special finite elements with embedded discontinuities in their interpolation functions to adequately model the real kinematics. Also, in Chapter 5, various contact laws have been reviewed and subsequently adapted to describe the shear band constitutive behaviour.

In this chapter, the implementation of foregoing formulations into a finite element program is discussed together with strategies adopted for the solution of numerical difficulties which inevitably arise in such a complex model.

6.2. Issues on model implementation

The discrete nature of the approach adopted for the modelling of shear bands inevitably introduces problems associated with the proper determination of the geometrical location and inclination of a shear band within a typical element. In a smeared scheme, the band topology is not indeed a real issue—the sole concern is in fact to diffuse the deformations generated inside the band over the entire representative domain, i.e. the element, in order to reproduce an idealized pseudo-uniform mode.

In contrast, the methodology herein followed examines the shear banded element at a discrete level—in more precise terms the kinematics are the primary features which govern the behaviour of the structure. Therefore in the post localized regime, the behavioural response of the element is modelled by introducing pseudo degrees of freedoms meant to enhance its deformational capabilities. As such, the location of the shear band inside the element must be determined as accurately as possible since any deviation from *reality* may cause drastic changes in the predictive behaviour of the element. This is why a scheme has to be found, based on stress values or state variables within the element. Thus in order to arrive at a sensible method, a proper understanding of shear band inception and physical meaning are needed.

The localization of deformation into a shear band is closely connected with the loss of ellipticity (bifurcation) of the governing equilibrium equation. The characteristic equations (surfaces) then indicate the location and shape of the localized zones, but leave the size undetermined. It bears emphasis to say that in this method, localization conditions are considered local, i.e. they can be ascertained into an elementary or point-wise fashion. Turning back to the finite element discretization by a displacement type of formulation, it can be seen that difficulties arise as to the accuracy of locating the band. As well established now, in a displacement type formulation, a displacement field which satisfies inter-element

compatibility is searched so that it makes the potential energy functional achieve a stationary value. As a result, equilibrium conditions will only be satisfied in an average sense, i.e. the computed stress field will be approximate.

Since the loss of ellipticity can be assessed in a discrete manner, i.e. at Gauss sampling points, the inclination predicted will not be representative of the actual ones because they have been determined from stress values which satisfy governing equations of equilibrium only on an average sense. This is the drawback which is usually inherited from a displacement type of formulation. Even if the shear band were to be found accurately, the continuity of stresses at the interface would not be fully satisfied—the analysis may be thereby questionable. However, these problems can be erased by adopting a stress or hybrid type of formulation. For a preliminary study, it is thought that the displacement based formulation can still give fairly accurate results. The hybrid formulation would require much more computational effort both from the analytical and computational standpoints.

It is logical to think about trying to determine the locus of points which will satisfy the bifurcation condition inside the element. The question is whether the shear band directions found for each point on the locus surface really coincide with the tangent to the same point. It is thought that they do not need to coincide since the locus surface can be crossed by an infinite number of shear bands. A reasonable scheme to locate the shear band would most probably involve finding an equivalent or mean value of all shear band inclinations computable along the locus surface. Once this has been found the locus has to be adjusted along the mean shear band inclination. However, the condition of bifurcation along the shear band might not be satisfied any more. This inevitably requires an iterative process similar to the location of a free surface in unconfined flow problems.

6.3. Computational aspects of localization

In the solution of a generalized elasto-plastic boundary value problem, the whole domain is viewed as being elastic at the very beginning of the deformation process. Moreover, as applied external loads are gradually increased, the state of stress at any generic point becomes progressively severe so as to cause a local instability (bifurcation) of the constitutive law which coincides with localization. This condition was mathematically derived in Chapter 3 and is recalled for clarity of exposition:

$$\det(n_i L_{ijkl} n_l) = 0, \quad (6.1)$$

in which the indices i, j, k, l range from 1 to 3 (summation implied upon repeated indices) for 3-D stress conditions, \mathbf{n} is the unit normal vector to an incipient shear band, and L_{ijkl} is the fourth order tensor of the tangential constitutive operator.

Without losing too much generality, only 2-D stress configurations will be addressed in this thesis. Equations (3.4) and (3.11) gave respectively the relation between the tensor components of stress and strain, and the explicit form of the elasto-plastic tangential constitutive tensor which would have to be replaced in Eq. (6.1). For finite element analysis purposes, it is more convenient to express the relationship in matrix form, i.e., in 2-D situations:

$$\{\dot{\sigma}\} = [L] \{\dot{\epsilon}\}, \quad (6.2)$$

where

$$\{\dot{\sigma}\} = \{\dot{\sigma}_{11}, \dot{\sigma}_{22}, \dot{\sigma}_{12}\}, \quad (6.3a)$$

$$\{\dot{\epsilon}\} = \{\dot{\epsilon}_{11}, \dot{\epsilon}_{22}, \dot{\epsilon}_{12}\}. \quad (6.3b)$$

Because of symmetry of the stress and strain tensors, interchanging i and j or k and l in Eq. (6.1) results in the same quantity, thus the matrix $[L]$ is related to tensor L_{ijkl} as follows:

$$[L] = \begin{bmatrix} L_{1111} & L_{1122} & L_{1112} \\ L_{2211} & L_{2222} & L_{2212} \\ L_{1211} & L_{1222} & L_{1212} \end{bmatrix}. \quad (6.4)$$

While the solution of the bifurcation criterion given in Eq. (6.1) has to be checked during the numerical integration of the constitutive equation represented by (6.2), onset of localization will occur at the first point in the deformation history for which non trivial solutions of the determinant exist. Calling the tensor inside the determinant an *acoustic* tensor A_{jk} whose expression after partial expansion is

$$A_{jk} = n_1^2 L_{1jk1} + n_1 n_2 (L_{1jk2} + L_{2jk1}) + n_2^2 L_{2jk2}, \quad (6.5)$$

Eq. (6.1) reduces to

$$\begin{vmatrix} A_{11} & A_{12} \\ A_{21} & A_{22} \end{vmatrix} = 0, \quad (6.6)$$

in which

$$A_{11} = n_1^2 L_{1111} + n_1 n_2 (L_{1112} + L_{2111}) + n_2^2 L_{2112}, \quad (6.7a)$$

$$A_{22} = n_1^2 L_{1212} + n_1 n_2 (L_{1222} + L_{2212}) + n_2^2 L_{2222}, \quad (6.7b)$$

$$A_{12} = n_1^2 L_{1112} + n_1 n_2 (L_{1122} + L_{1212}) + n_2^2 L_{1222}, \quad (6.7c)$$

$$A_{21} = n_1^2 L_{1211} + n_1 n_2 (L_{1221} + L_{2211}) + n_2^2 L_{2212}. \quad (6.7d)$$

Expanding the determinant finally gives rise to a complete fourth order polynomial,

$$f(\theta) = b_0 + b_1 \tan \theta + b_2 \tan^2 \theta + b_3 \tan^3 \theta + b_4 \tan^4 \theta = 0, \quad (6.8)$$

where

$$\begin{aligned} b_0 &= (L_{1111} L_{1212} - L_{1112} L_{1211}) \\ b_1 &= (L_{1111} L_{1222} + L_{1111} L_{2212} - L_{1112} L_{2211} - L_{1211} L_{1122}) \\ b_2 &= (L_{1111} L_{2222} + L_{1112} L_{1222} + L_{1211} L_{2212} - L_{1122} L_{1212} - L_{1122} L_{2211} - L_{1212} L_{2211}) \\ b_3 &= (L_{1112} L_{2222} + L_{1211} L_{2222} - L_{1222} L_{2211} - L_{2212} L_{1122}) \\ b_4 &= (L_{1212} L_{2222} - L_{1222} L_{2212}) \end{aligned} \quad (6.9)$$

and $\tan \theta = n_2/n_1$.

Once the shear band directions are determined, the *acoustic* tensor A is totally defined and its zero eigenvectors are found. If a is an eigenvector whose components are a_1 and a_2 in the Cartesian axes (x_1, x_2) then

$$\begin{bmatrix} A_{11} & A_{12} \\ A_{21} & A_{22} \end{bmatrix} \begin{Bmatrix} a_1 \\ a_2 \end{Bmatrix} = \begin{Bmatrix} 0 \\ 0 \end{Bmatrix}, \quad (6.10)$$

and hence the bifurcation direction ω is given by

$$\frac{a_2}{a_1} = \tan \omega = \frac{-[L_{1111} + (L_{1112} + L_{1211})\tan \theta + L_{1212} \tan^2 \theta]}{[L_{1112} + (L_{1122} + L_{1212})\tan \theta + L_{1222} \tan^2 \theta]} \quad (6.11)$$

The geometrical representation of the shear band direction with respect to the global reference axes (x,y) , together with the corresponding bifurcation direction are given in Fig. 6.1.

6.3.1 Determination of a bifurcation point

Ideally in a finite element analysis, real roots of Eq. (6.8) must be sought to confirm localization conditions. In other words, the bifurcation point must be pin-pointed sometime during the evolution of the loading history. Solving for roots of the polynomial in Eq. (6.8) is tantamount to searching for the normals of the prospective fronts upon which the displacement field may be discontinuous.

Since the bifurcation criterion will have to be checked in a point wise fashion during the course of deformation at Gauss points where stress and strain are most accurately determined, an efficient numerical procedure has to be found. It is proposed to analytically solve the roots of $f(\theta)$ rather than resort to a standard numerical scheme which involves iterations.

Solving Eq. (6.8) is similar to finding the intersection of the quartic function with the θ axis, see Fig. 6.2. If all possible roots of $f(\theta)$ are complex, i.e minima of the quartic are positive, this implies that the solution regime is elliptic. Possible real solutions will only be obtained whenever one of the minima becomes zero or negative, i.e. tangent and past the θ axis respectively. As such, the possible solutions regimes will be obtained according to the stress dependent coefficients b_i given in Eq. (6.9) as the curve $f(\theta)$ moves continuously towards the θ axis. This can be extended to a 3-D situation in which a surface is instead obtained and its minima corresponding to points of tangency of the surface to a horizontal plane passing through the origin are sought.

Keeping the above observation in mind, one has the following algorithm for a 2-D situation, summarized in Table 6.1, which derives from Galois theory (see for example Hungerford [1974]).

Table 6 1. Solution Algorithm for Quartic Equation

Solve for the real roots of:

$$b_0 + b_1 \tan \theta + b_2 \tan^2 \theta + b_3 \tan^3 \theta + b_4 \tan^4 \theta = 0$$

if $b_4 = 0$, then solve the corresponding cubic equation

else let $\lambda = \tan \theta$, $a = b_3/b_4$, $b = b_2/b_4$, $c = b_1/b_4$, $d = b_0/b_4$

solve

$$\lambda^4 + a \lambda^3 + b \lambda^2 + c \lambda + d = 0.$$

1. Form resolvent cubic:

$$\lambda^3 - b\lambda^2 + (ac - 4d)\lambda + (-a^2d + 4bd - c^2) = 0.$$

2. Let

$$p = (b/3)^2 - (ac - 4d) / 3,$$

$$q = (b/3)^3 - b(ac - 4d) / 6 + (a^2d - 4bd + c^2) / 2.$$

3. If $q^2 - p^3 \geq 0$ (resolvent cubic has only one real root) then let

$$y = \sqrt[3]{q + \sqrt{q^2 - p^3}} + \sqrt[3]{q - \sqrt{q^2 - p^3}} + b/3$$

Else let

$$y = 2\sqrt{p} \cos\left(\frac{1}{3} \arccos\left(\frac{q}{p\sqrt{p}}\right)\right) + b/3.$$

4. Solution of two quadratics:

Let

$$Q = \sqrt{\frac{a^2}{4} - b + y}, \quad S = \frac{3a^2}{4} - 2b - Q^2.$$

5. If $Q \neq 0$ then let

$$T = \frac{4ab - 8c - a^2}{4Q}$$

Else let

$$T = 2\sqrt{y^2 - 4d}$$

6. If $T + S \geq 0$ then let the first two roots be

$$\lambda = -\frac{a}{4} + \frac{Q}{2} \pm \frac{\sqrt{S+T}}{2}$$

else if $S - T \geq 0$ then let the two other roots be

$$\lambda = -\frac{a}{4} - \frac{Q}{2} \pm \frac{\sqrt{S-T}}{2}$$



6.3.2 Test problems

The algorithm used to locate shear band inception and its orientation in space is illustrated by examining a single quadratic 4 node element.

Figure 6.3 illustrates one single element whose configuration is such that three nodes are restrained to move in both x and y directions, while the fourth node is subjected to prescribed displacements. The loading condition is of particular interest because the prescribed displacements are consistent with a non uniform field very much prone to localization conditions. In contrast to loading conditions consistent with a constant strain field where all Gauss points bifurcate at the same time, the present configuration allows for non-simultaneous bifurcation of Gauss points due to a non-homogeneous field.

The material is assumed to obey simple J_2 flow plasticity behaviour with a hardening/softening stress-strain law. The material properties used and the explicit expression of the consistent tangent operator are summarized in Table 6.2. It is noted that a negative hardening modulus is used in the analysis to guarantee localization; a feature which has been discussed in Chapter 3.

As displacements are prescribed, the material progressively deforms until plastic yielding first occurs at Gauss point 1. Gauss point 4 subsequently follows while the other Gauss points 2 and 3 are essentially still elastic.

During the stress integration, the tangential operator for the stress-strain law is subjected to bifurcation analysis and the scheme described in the previous section is applied. A bifurcation analysis at an elemental level predicts inception of a shear band at Gauss point 1 with two distinct inclinations. It is understood there, that the two shear band configurations are kinematically possible since the bulk material is deformable and not rigid. Fig. 6.4 shows the force displacement curve for node 4 in the homogeneous situation with the corresponding bifurcation point. The evolution of the determinant of the acoustic tensor during the search of a prospective shear band is depicted in Fig. 6.5, while shear strains at the Gauss points for the homogeneous situation are plotted in Fig. 6.6.

At first, the governing field equations are elliptic in nature and this results into a positive determinant. As the loading conditions become more severe, the equations change regime from elliptic to parabolic. Two possible shear band inclinations are obtained. The analysis necessitates both inclinations to be equally possible since they would both satisfy conditions of statics and kinematics. However, the shear band inclination which dissipates the most energy, and which is fully compatible with loading and boundary conditions will prevail.

6.4 Numerical algorithm

The proposed model requires a special finite element algorithm for the solution of the localized problem. The non-linear problem is solved by applying the load incrementally. Within each load increment, several conditions are checked namely: plasticity, bifurcation and evolution of the shear band. The analysis goes through several iterations until all pertinent criteria—satisfaction of yield and slip conditions for the ambient material and the shear band respectively—are satisfied, and an equilibrium state is reached.

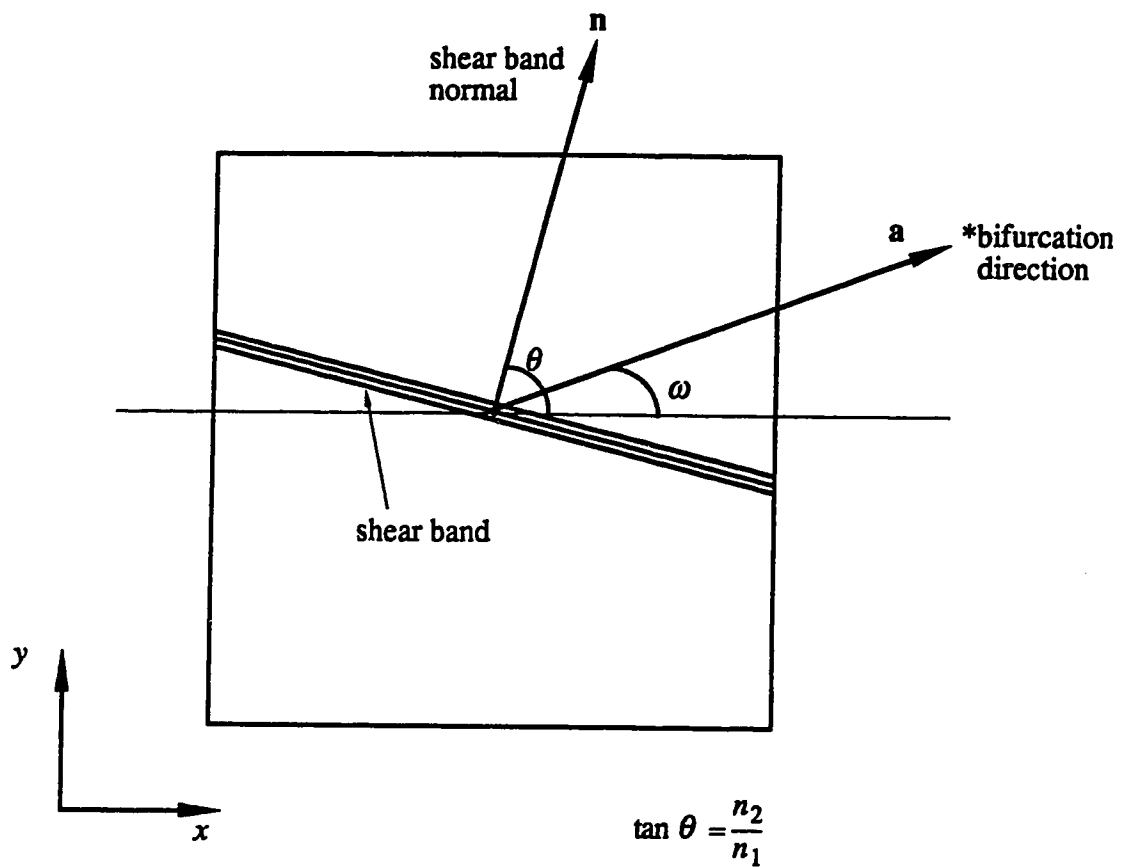
The different steps in the algorithm used are summarized in Table 6.3. For a typical pseudo-time interval of interest $[t_n, t_{n+1}]$, suppose that displacements \mathbf{u}_n , slip displacements \mathbf{g}_n , stresses $\boldsymbol{\sigma}_n$ and internal tractions \mathbf{t}_n are perfectly known for the beginning of the step t_n . As an initial guess (iteration number $i=1$), all field variables are set to previous values as shown in step 2. The load vectors for both the continuous and discontinuous components are then computed. These are next compared with the internal work equivalent forces in order to check for global equilibrium of the system as given in step 5. Since there are two force equilibria to be satisfied, i.e one regarding the continuous displacements, and the other the slip displacements, each criterion has to be treated one at a time until the two conditions are approximately achieved.

The composite stiffness matrix is either updated or expanded (case there is a new band formed) in step 6 in order to evaluate the trial displacements in step 7. The strains are next computed using the standard procedure, except that now there is a contribution from the discontinuous displacement components. The traction forces along the shear band are checked against the Coulomb slip criterion. If slip occurs, the tangential traction forces are limited to the values tolerated by the frictional and cohesive characteristics of the interface. If the traction forces are tensile, then the opening of the interface at the shear band is kept to a limiting value. The analysis continues by incrementing the displacements as well as the slip displacements, and equilibrium is checked once again by going to step 4.

In the event that slip conditions are fulfilled along the shear band, together with equilibrium, bulk convergence is next verified. If yielding of the bulk material occurs, the analysis goes into a classical plasticity algorithm, and residual forces are evaluated iteratively until an equilibrium state is reached.

The next step is to check bifurcation conditions locally for each element. If any new Gauss point bifurcates, this will be taken into account in the next load increment when the stiffness matrix is calculated in step 6. Since there has been a change in configuration, pertinent information at Gauss points such as stresses, strains, plastic strains and other state variables are reset, and appropriate values for new Gauss points required by the new shear band element are found by extrapolation from original Gauss points.

Details on implementation with regards to calculation of the constituent stiffness matrices, load terms and shape functions are given in Appendix B to assist the reader.



*bifurcation direction indicates the direction of relative displacement of points on the shear band.

Figure 6.1 Geometrical representation of shear band in 2-D situation

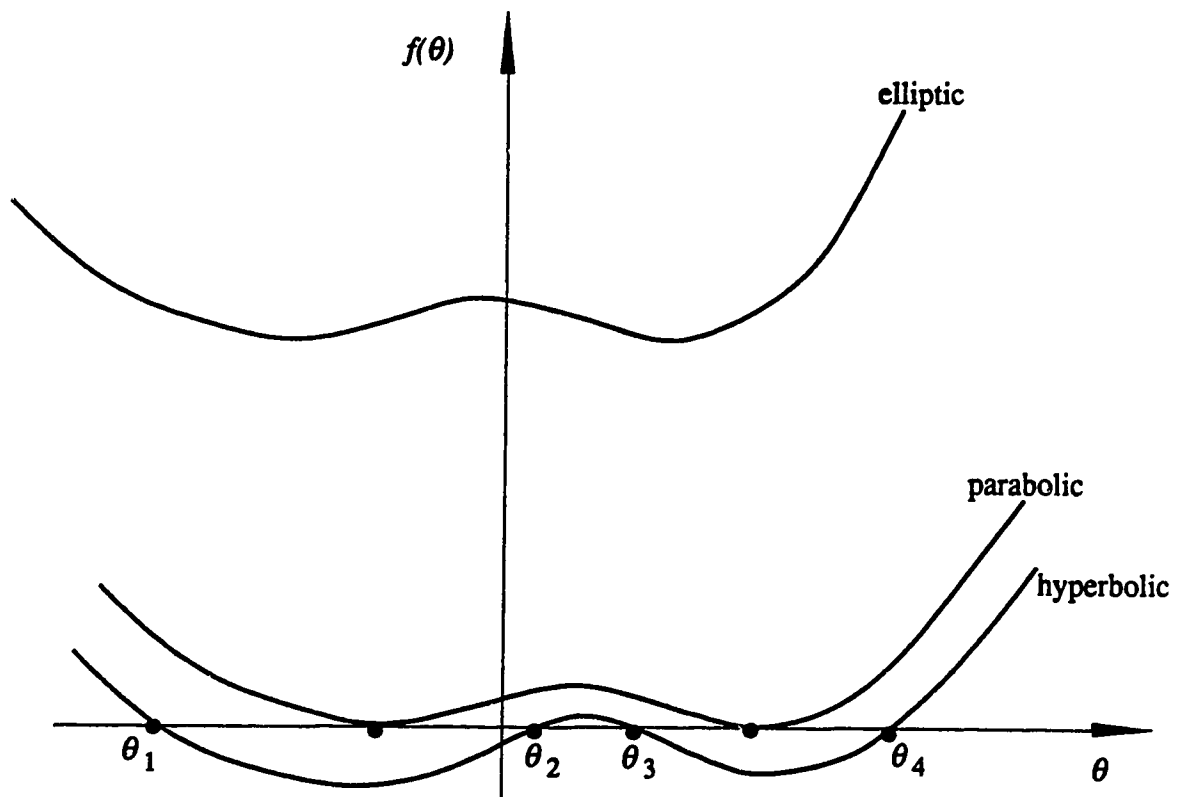


Figure 6.2 Schematic representation of finding shear band inclinations from bifurcation criterion

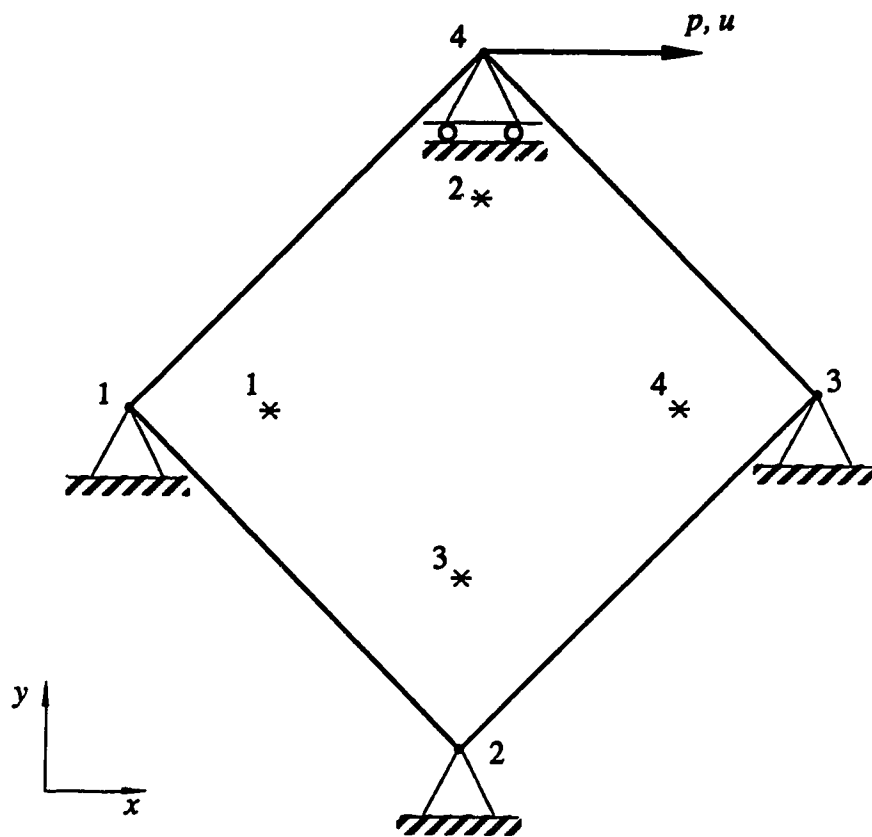


Figure 6.3 Non-uniform shear loading: One element test problem

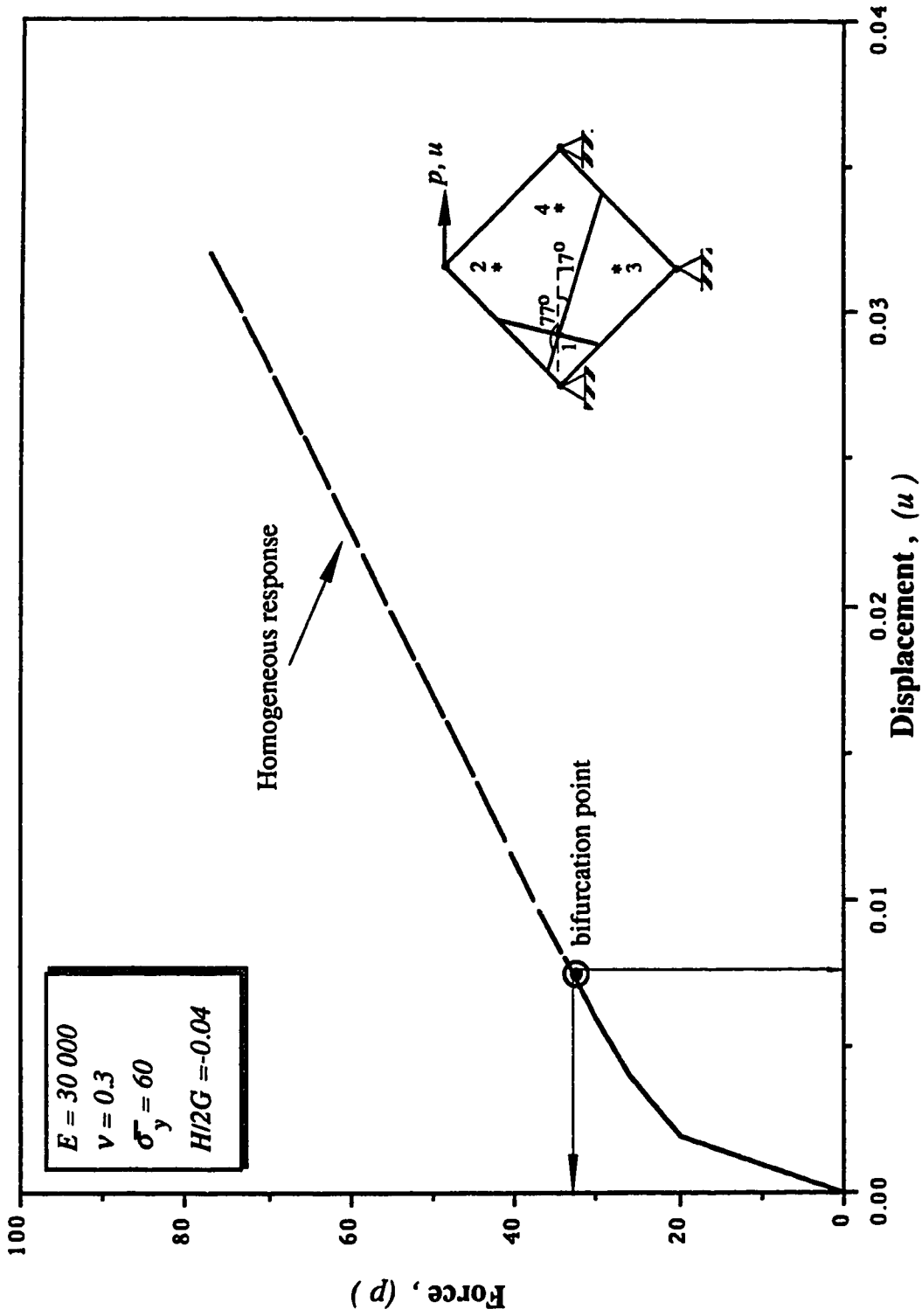


Figure 6.4 Force-Displacement curve for non-uniform shear loading

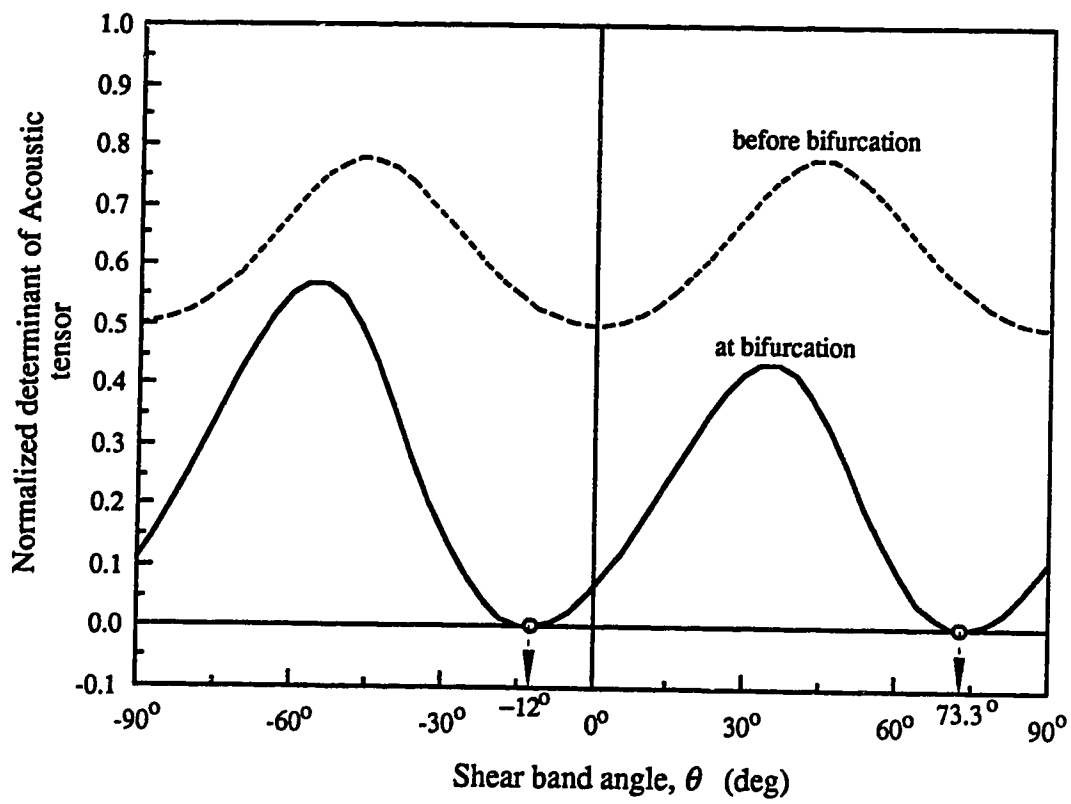


Figure 6.5 Evolution of the determinant of acoustic tensor with loading history

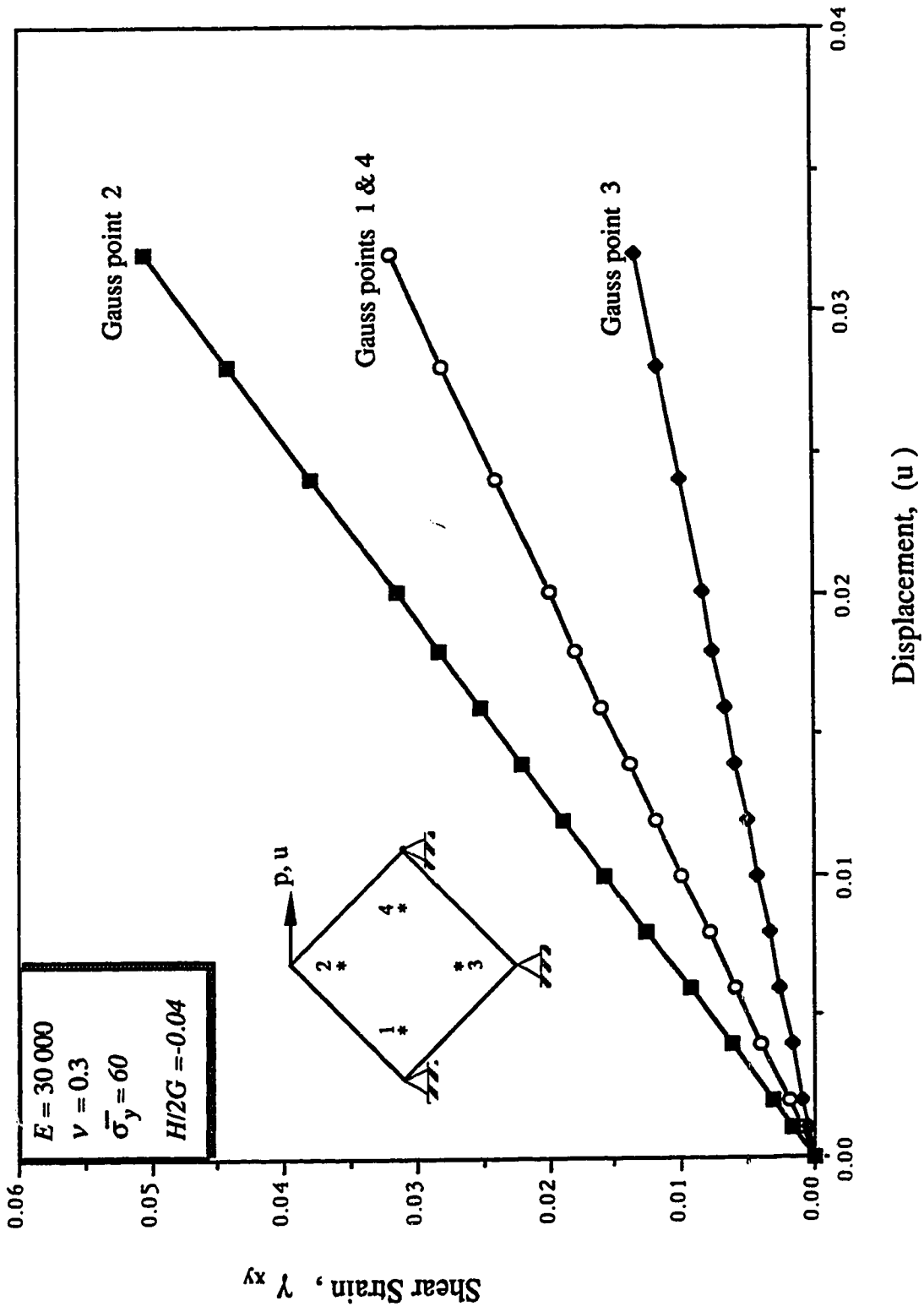


Figure 6.6 Evolution of shear strains at Gauss points for homogeneous analysis

Table 6.2 J_2 flow plasticity

Yield Function:

$$F = \sqrt{3J_2} - \kappa(\bar{\epsilon}^p) = 0.$$

Hardening Rule:

$$\kappa(\bar{\epsilon}^p) = \bar{\sigma}_y + H\bar{\epsilon}^p.$$

Effective Plastic Strain Rate:

$$\bar{\epsilon}^p = \int_0^t \sqrt{\frac{2}{3}} [\dot{\epsilon}^p : \dot{\epsilon}^p]^{1/2} d\tau, \quad \dot{\epsilon}^p = \dot{\epsilon} - \frac{1}{3} \text{trace}(\dot{\epsilon}^p) \mathbf{1}.$$

$$J_2 = \sqrt{3} [\mathbf{s} : \mathbf{s}]^{1/2}, \quad \mathbf{s} = \boldsymbol{\sigma} - \frac{1}{3} \text{trace}(\boldsymbol{\sigma}) \mathbf{1}, \quad \text{and } \mathbf{1} = \text{Kronecker delta}.$$

Incremental Stress - Strain Relationship:

$$\dot{\boldsymbol{\sigma}} = \mathbf{L} : \dot{\boldsymbol{\epsilon}};$$

For a load step between times t_n and t_{n+1} , at iteration k , the consistent modulus becomes:

$$\mathbf{L}_{n+1}^k = K \mathbf{1} \otimes \mathbf{1} + 2G\beta(\mathbf{I} - \frac{1}{3}\mathbf{1} \otimes \mathbf{1}) - 2G\bar{\lambda}_{n+1} \hat{\mathbf{n}} \otimes \hat{\mathbf{n}}$$

where

$$\mathbf{I}_{ijkl} = \frac{1}{2} (\mathbf{1}_{ij}\mathbf{1}_{kl} + \mathbf{1}_{ik}\mathbf{1}_{jl}), \quad \hat{\mathbf{n}} = \frac{\mathbf{s}_{n+1}^r}{\|\mathbf{s}_{n+1}^r\|}, \quad \mathbf{s}_{n+1}^r \text{ the trial deviatoric stress,}$$

$$\text{and } \beta = \sqrt{\frac{2}{3}} \frac{(\bar{\sigma}_y + H\bar{\epsilon}_{n+1}^p)}{\|\mathbf{s}_{n+1}^r\|}, \quad \bar{\lambda}_{n+1} = \frac{1}{1 + H/3G} - (1 - \beta).$$

$\|\cdot\|$ denotes a tensor norm and \otimes the tensor product in the sense that $(\mathbf{a} \otimes \mathbf{b})_{ijkl} = (\mathbf{a})_{ij}(\mathbf{b})_{kl}$.

$$E = 3.0 \cdot 10^4 \text{ units, } \nu = 0.3, \quad \bar{\sigma}_y = 60.0 \text{ and } H/2G = -0.04$$

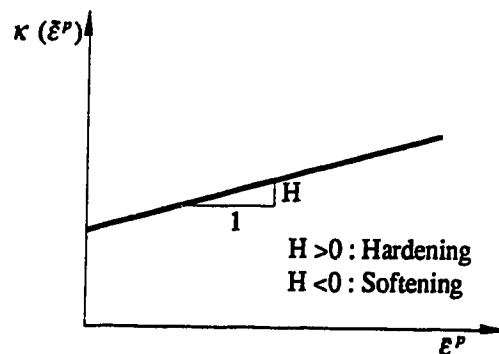
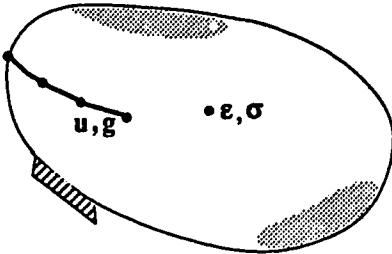
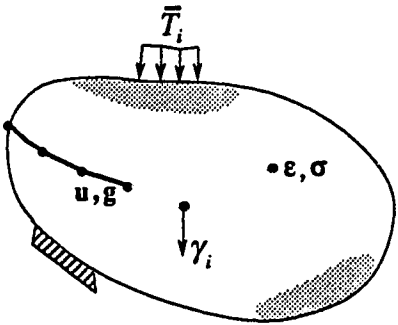


Table 6.3 Flow chart for localization problem algorithm

1. For increment $n+1$, set iteration number $i=1$	
2. As initial guess, set : $\mathbf{u}_{n+1}^i = \mathbf{u}_n$, $\mathbf{g}_{n+1}^i = \mathbf{g}_n$, $\boldsymbol{\sigma}_{n+1}^i = \boldsymbol{\sigma}_n$, $\mathbf{t}_{n+1}^i = \mathbf{t}_n$.	
	
3. Set load level $(\mathbf{f}_\Omega)_{n+1} = \lambda_{n+1}^i \mathbf{f}_\Omega$, $(\mathbf{f}_s)_{n+1} = \lambda_{n+1}^i \mathbf{f}_s$, with $\lambda_{n+1}^i = 1$.	
	$\mathbf{f}_\Omega = \int_\Omega \mathbf{N}^{(\alpha)} \cdot \gamma \, d\Omega + \int_\Gamma \mathbf{N}^{(\alpha)} \cdot \bar{\mathbf{T}} \, d\Gamma,$ $\mathbf{f}_s = \int_\Omega \mathbf{N}^{(\beta)} \cdot \gamma \, d\Omega + \int_\Gamma \mathbf{N}^{(\beta)} \cdot \bar{\mathbf{T}} \, d\Gamma.$
4. Evaluate residual forces:	
$\Psi_\Omega(\mathbf{u}_{n+1}^i) = (\mathbf{f}_\Omega)_{n+1} - \int_\Omega \mathbf{B}^{(\alpha)\top} : \boldsymbol{\sigma}_{n+1}^i \, d\Omega,$ $\Psi_s(\mathbf{g}_{n+1}^i) = (\mathbf{f}_s)_{n+1} - \int_\Omega \mathbf{B}^{(\beta)\top} : \boldsymbol{\sigma}_{n+1}^i \, d\Omega - \int_{\Gamma_s} \mathbf{N}^{(\beta)\top} \cdot \mathbf{t}_{n+1}^i \, d\Gamma.$	
5. Perform convergence check on norm of residual forces:	
$\begin{bmatrix} \ \Psi_\Omega\ \\ \ \Psi_s\ \end{bmatrix} \leq \varepsilon_L \begin{bmatrix} \ (\mathbf{f}_\Omega)_{n+1}\ \\ \ (\mathbf{f}_s)_{n+1}\ \end{bmatrix}.$	
...continued	

Has solution converged?	
NO	YES
<p>6. Set up stiffness matrix or update as required:</p> $\begin{bmatrix} \mathbf{K}_{\Omega\Omega} & \mathbf{K}_{\Omega S} \\ \mathbf{K}_{S\Omega} & \mathbf{K}_{SS} \end{bmatrix}_{n+1}^i$	<p>Bulk Convergence?</p>
<p>7. Evaluate iterative displacements:</p> $\begin{bmatrix} \mathbf{K}_{\Omega\Omega} & \mathbf{K}_{\Omega S} \\ \mathbf{K}_{S\Omega} & \mathbf{K}_{SS} \end{bmatrix}_{n+1}^i \begin{Bmatrix} \delta \mathbf{u}_{n+1}^{i+1} \\ \delta \mathbf{g}_{n+1}^{i+1} \end{Bmatrix} = \begin{Bmatrix} \Psi_{\Omega}(\mathbf{u}_{n+1}^i) \\ \Psi_s(\mathbf{g}_{n+1}^i) \end{Bmatrix}$	<p>YES</p> <p>Set:</p> $\mathbf{u}_{n+1} = \mathbf{u}_{n+1}^{i+1}$ $\mathbf{g}_{n+1} = \mathbf{g}_{n+1}^{i+1}$ $\boldsymbol{\sigma}_{n+1} = \boldsymbol{\sigma}_{n+1}^{i+1}$ $\mathbf{t}_{n+1} = \mathbf{t}_{n+1}^{i+1}$
<p>8. Evaluate iterative strains:</p> $\delta \boldsymbol{\epsilon}_{n+1}^{i+1} = \mathbf{B}^{(\alpha)} \cdot \delta \mathbf{u}_{n+1}^{i+1} + \mathbf{B}^{(\beta)} \cdot \delta \mathbf{g}_{n+1}^{i+1}$ <p>$\delta \mathbf{g}_{n+1}^{i+1}$ = strains in shear band, i.e. slip displacements per unit thickness.</p>	<p>NO</p> <p>Calculate iterative strains</p> <p style="text-align: center;">↓</p> <p>Classical plasticity calculations</p> <p style="text-align: center;">↓</p> <p>calculate residual $\Psi_{\Omega}(\mathbf{u}_{n+1}^{i+1})$ on going to step 4.</p>
<p>9. If relevant, check stress state on shear band:</p> $\delta \mathbf{t}_{n+1}^{i+1} = \boldsymbol{\eta}^e \cdot \delta \mathbf{g}_{n+1}^{i+1}$ $\mathbf{t}_{n+1}^{i+1} = \mathbf{t}_{n+1}^i + \delta \mathbf{t}_{n+1}^{i+1}$ <p>Check following criteria:</p> $ \tau_s \leq c_d s + \tau_n \tan \phi_d \rightarrow \text{slip.}$ $\tau_n \geq -R_T s \rightarrow \text{Tension.}$ <p>R_T = Tensile strength, s = surface area of band.</p>	<ul style="list-style-type: none"> • Check bifurcation locally for each element for converged state, i.e. $(\det(\mathbf{n}:L:\mathbf{n}))=0$ • Go to next load increment with a change in configuration if bifurcation ever occurs. • Reset information concerning element topology, bandwidth, gauss points etc. and go to 1.
<p>slip?</p>	
<p>YES</p>	<p>NO</p>
<p>Truncate \mathbf{t}_{n+1}^i to tolerable values, i.e. $(\tau_s)_{n+1}^{i+1} c_d s \tan \phi_d$</p>	<p>Tension?</p>
	<p>YES</p>
	<p>NO</p>
<p>Update displacements: $\mathbf{u}_{n+1}^{i+1} \quad \mathbf{u}_{n+1}^i \quad \delta \mathbf{u}_{n+1}^{i+1}$ $\mathbf{g}_{n+1}^{i+1} \quad \mathbf{g}_{n+1}^i \quad \delta \mathbf{g}_{n+1}^{i+1}$</p> <p>Update traction forces: $\mathbf{t}_{n+1}^{i+1} \quad \mathbf{t}_{n+1}^i \quad \delta \mathbf{t}_{n+1}^{i+1}$</p> <p>Go to 4 to evaluate $\Psi_s(\mathbf{g})$.</p>	

Chapter 7

Numerical Results

7.1. Introduction

Many practical examples of application become amenable to analysis by means of the model formulated in Chapter 4. In a first stage, in order to pursue an investigation of fundamentals, a numerical assessment of the discontinuity element will be presented by an eigenvalue analysis and a patch test. Then, the model is applied to simple test problems in order to show exactly how it describes phenomena of localization. In a last stage, the numerical tests will shift over to a general boundary value problem. Comparison is made with the conventional continuous formulation in order to illustrate the method. It is important to underscore at this point that all the cases examined herein are restricted to a fairly elementary situation with no fluid flow regime.

7.2. Numerical assessment of the method

7.2.1 Eigenvalue analysis

The soundness and merit of the discontinuity interpolation functions described in Chapter 4 can be verified by an eigenvalue method approach which in other words gives a measure of

strain energy content associated with the element under several deformational modes. The decompositions of the element stiffness matrix into its consistent eigenvectors and associated eigenvalues are a necessary check on the validity of the element. This analysis was conducted to study the net effect of the discontinuous interpolation functions, their ability to reproduce localized modes and sensitivity towards convergence of the solution. The stiffness matrix as derived from the strain energy based upon the modified Principle of Virtual Work is used. A typical form of the element stiffness matrix for a QD4 element is recalled below for clarity of exposition:

$$[\mathbf{K}] = \begin{bmatrix} \mathbf{K}_{\Omega\Omega}^e = \int_{\Omega} \mathbf{B}^{(\alpha)T} : \mathbf{L} : \mathbf{B}^{(\alpha)} d\Omega & \mathbf{K}_{\Omega S}^e = \int_{\Omega} \mathbf{B}^{(\alpha)T} : \mathbf{L} : \mathbf{B}^{(\beta)} d\Omega \\ \mathbf{K}_{S\Omega}^e = \int_{\Omega} \mathbf{B}^{(\beta)T} : \mathbf{L} : \mathbf{B}^{(\alpha)} d\Omega & \mathbf{K}_{SS}^e = \int_{\Omega} \mathbf{B}^{(\beta)T} : \mathbf{L} : \mathbf{B}^{(\beta)} d\Omega \\ & + \int_{\Gamma_{ib}} \mathbf{N}^{(\beta)T} : \boldsymbol{\eta} : \mathbf{N}^{(\beta)} d\Gamma \end{bmatrix} \quad (7.1)$$

Two cases on discontinuity locations have been considered, namely the discontinuity cutting across two opposite sides of the QD4 element, denoted by option 1, and across two adjacent sides, denoted by option 2. The study has been performed on a master element of side length one unit in plane strain elasticity using a Young's modulus of 1.0 unit and Poisson's ratio of 0.3. The corresponding properties for the shear band were 1.0 unit for the shear stiffness and 1000.0 units for the normal stiffness to avoid any separation or penetration modes. Off-diagonal stiffness terms in the shear band matrix were set to zero, implying no coupling between normal and tangential slip displacements at the shear band interface.

Due to element configuration which consists of 8 displacement degrees of freedom at the external nodes and 4 slip displacement degrees of freedom at the localized nodes, the size of the stiffness matrix in Eq. (7.1) becomes a 12x12 matrix.

The eigenvalue problem is mathematically recalled. It states that for an element possessing non-zero eigenvalues, the eigenvectors of the stiffness can be found by solving

$$\begin{bmatrix} K_{\Omega\Omega} & K_{\Omega S} \\ K_{S\Omega} & K_{SS} \end{bmatrix} \begin{Bmatrix} X_{\Omega} \\ X_S \end{Bmatrix} = \lambda_i \begin{Bmatrix} X_{\Omega} \\ X_S \end{Bmatrix} = f_i, \quad (7.2)$$

in which X_{Ω} and X_S are nodal displacements for the continuous and discontinuous components respectively, and f_i are the nodal loads made proportional to the nodal displacements through the constant λ_i , namely the corresponding eigenvalue.

Three zero eigenvalue modes corresponding to the combination of translation and rotation of the continuum part were obtained. Relative displacements at the localized nodes were found to be zero in these particular instances in order to permit rigid body motion, refer to Section 4.9 for more details. From an energy point of view, this implies that the rigid body motion does not produce any straining, and hence stresses are zero.

The remaining nine non-zero eigenvalues and deformation modes emerge as a result of the amalgamation of modes belonging to the continuous and discontinuous components. These are illustrated in Figs. 7.1 and 7.2. with associated energy values. It is interesting to note that the five basic deformation modes pertaining to constant strain and linear strain rates are combined with those of the discontinuity surface.

The amount of strain energy related to the non-zero eigenvalue modes accounts for energies absorbed in deforming the continuum and the interface, as well as the continuum interface interaction. In other words, premultiplying both sides of Eq. (7.2) by the eigen vector results in the following:

$$\langle X_{\Omega} \quad X_S \rangle \begin{bmatrix} K_{\Omega\Omega} & K_{\Omega S} \\ K_{S\Omega} & K_{SS} \end{bmatrix} \begin{Bmatrix} X_{\Omega} \\ X_S \end{Bmatrix} = \lambda_i, \quad (7.3)$$

since the eigenvector is normalized as $\langle X_{\Omega} \quad X_S \rangle \langle X_{\Omega} \quad X_S \rangle^T = 1$. Further expansion of the above leads to:

$$\lambda_i = X_{\Omega}^T K_{\Omega\Omega} X_{\Omega} + X_S^T K_{SS} X_S + X_{\Omega}^T K_{\Omega S} X_S + X_S^T K_{S\Omega} X_{\Omega}, \quad (7.4)$$

i.e, the eigen value corresponds to the sum of twice the continuum strain energy, twice the interface strain energy and continuum interface coupling energy components. This implies that, referring back to the eigen modes in Figs. 7.1 and 7.2, the strain energy associated with modes 11 and 12 in both cases are very high, thus suggesting that they are least likely to occur. Since in general the response of the element during an arbitrary loading will be a linear combination of eigen modes, then separation and penetration of nodes at the interface will not take place so long as the boundary conditions are not in accord with those particular modes.

7.2.2 Patch test

It was proven in Chapter 4 that the assumed strain operator does not reduce the order of convergence of the scheme and that the shear band element should pass the patch test.

In this section, a patch of elements (10 elements), see Fig. 7.3, is subjected to a constant strain field and one investigates if it reproduces exactly the constitutive behaviour of the material and correct stresses as the patch becomes infinitesimally small. Interior nodes have been included in the region and an irregular mesh has been chosen to avoid any fortuitous self correction by symmetry. A plane strain problem is considered on the patch with the material governed by linear isotropic elasticity whose properties are summarized in Fig. 7.3. The finite element procedure is based on the displacement formulation using

classical 4-noded and 3-noded isoparametric shape functions, and linear discontinuous shape functions for the shear band.

Since the stiffness computation includes only first derivatives of displacements, and no derivative for slip displacements, the formulation converges provided the patch test is satisfied for all linear polynomial solutions of displacements. The patch test is performed using a 2x2 Gaussian, standard quadrature to compute each element stiffness. Nodes 1 and 2 are restrained both horizontally and vertically, while nodal displacements values of -0.1 unit are prescribed at nodes 3 and 4. The patch of elements is compared with a one single element, using option 1 in which the shear band cuts across two opposite edges the same way as in the patch of elements.

The values of displacements, hence strains and stresses, computed for the interior of the patch verify a constant field and satisfy the patch test. The solution obtained for displacements u, v and slip displacements g_x and g_y are given as :

$$\begin{aligned} u &= -0.18784 \cdot 10^{-2} \\ v &= 0.09962 y + 0.37665 \cdot 10^{-3} \\ \left. \begin{aligned} g_x &= -0.18784 \cdot 10^{-2} \\ g_y &= -0.37667 \cdot 10^{-3} \end{aligned} \right\} \text{uniform along shear band} \end{aligned}$$

This displacement field with the accompanying slip displacement field (g_x and g_y), see also Table 7.1, produce zero body forces and zero stresses except for

$$\sigma_y = -0.09962$$

and interface traction forces

$$t_s^1 = -0.01916$$

$$t_n^1 = -0.09579$$

The same solution can be reproduced from the one element patch test which involves the use of discontinuous shape functions for a quadrilateral. Alternatively forces compatible with the state of stress obtained in the previous tests were applied to nodes 3 and 4 and exactly the same results for stresses and strains were recovered.

Table 7.1 Patch test solution for Figure 7.3

Nodes			Displacements		Slip displacements	
	x	y	u	v	g_x	g_y
1	0.0	0.0	0.0000000	0.0000000		
2	0.0	0.0	0.0000000	0.0000000		
3	1.0	1.0	-0.0018784	-0.1000000		
4	0.0	1.0	-0.0018784	-0.1000000		
5	0.31	0.69	-0.0018784	-0.069117		
6	0.80	0.80	-0.0018784	-0.080075		
7	0.20	0.25	0.0000000	-0.024906		
8	0.65	0.35	0.0000000	-0.034868		
9	0.0	0.40			-0.0018784	-0.00037665
10	0.152	0.430			-0.0018784	-0.00037665
11	0.250	0.450			-0.0018784	-0.00037665
12	0.50	0.50			-0.0018784	-0.00037665
13	0.714	0.543			-0.0018784	-0.00037665
14	0.857	0.571			-0.0018784	-0.00037665
15	1.000	0.600			-0.0018784	-0.00037665

7.3 Simple boundary value problems

Many practical examples of application become amenable to analysis by use of the foregoing special discontinuity element. However in order to pursue an investigation of fundamentals, the cases herein presented are restricted to fairly elementary configurations for a preliminary study.

7.3.1 Mini-footing problem

An initially homogeneously stressed region is made to succumb to localization phenomena by artificial generation of shear bands within it, see Figure 7.4. A uniformly distributed load is applied on the element edge denoted by nodes 4 and 5. The medium is considered elastic and all geometric and material non-linearity is assumed concentrated in the shear band.

Shear bands are artificially made to branch from different sites in the mesh involving elements 1, 3, 2 and 4. Initiation and orientation of the shear band are dictated by a Mohr-Coulomb type of criterion based on the principle of maximum stress obliquity. Furthermore, in the event of conjugate directions, the orientation compatible with prevailing kinematic constraints is chosen. In order to establish compatibility between discontinuous (shear band) elements and adjacent continuum elements, the tip of the band is prescribed as a *node* of zero slip in the computations. Figure 7.5 depicts the distribution of typical displacements in such situation when the shear band is not fully developed, with the tip located at the boundary of two elements.

The mobilized slippage tendency indicates that most of the movement occurs in the vicinity of the applied loads. Also the stress distribution with the shear band in place reveals a substantial difference from the one expected for the unfaulted case, i.e, stresses are released and principal stress rotations reduced in regions outside the band. For example the rotation of principal stresses adjacent to line 1-4 in Figure 7.4 may be noted. This suggests that loads tend to localize along the band leaving the surrounding areas in an

unloading state. Moreover, stresses in element 2 are very small in comparison with others while some tension develops in elements 1 and 4 as one segment of corresponding shear band elements tries to detach itself from the rest of the elements. Here the normal stiffness of the shear band has been prescribed at a high enough value that tensile opening or separation is prohibited although the shear band curves upwards or downwards. If the load were to be incremented further in the analysis, a new stress field would have to be found and a new equilibrium configuration established with the band penetrating further into element 5. However the shear band orientation in other elements would have to be adjusted until a new equilibrium state is reached. Finally the mobilized shear stresses plotted at Gauss integration points along the shear band typically show the well known trend of peak values at the leading tip with lesser values at sites where most movement has taken place.

7.3.2 Mini-embankment problem

The numerical example shown in Figure 7.6 relates to a slope problem involving an embankment subjected to loads at the crest. A very coarse mesh is used since the object of the analysis is to illustrate the effectiveness of the kinematics. An elastic analysis was performed. Based upon the principle of maximum stress obliquity or the bifurcation expression in equation (3.7), shear bands were artificially embedded in the mesh by activating the discontinuity shape functions which interpolate the slip displacements.

A noteworthy outcome of the analysis is the promotion of enhanced kinematics under shear band mode of deformation. By way of contrast, a conventional analysis does not capture the discontinuous behaviour since localization tends to be diffused and smeared out in the mesh, unless the latter is properly designed. Figure 7.7 shows the distribution of internal traction forces, hence mobilized shear stresses along the shear band. However, due to bending of the shear band as it daylight to the free surface, the element tends to lock itself at kinks. This explains the drop in internal traction distribution. In fact for a finer mesh, the distribution would smooth out. Figure 7.8 illustrates the levels of contours of

shear strains. It is observed that the gradient of shear strains becomes higher in the enhanced analysis when compared with a conventional continuum run in Figure 7.9. This demonstrates the promotion of localization and highlights the significance of such calculations.

7.4 Rigid punch problem

The classical punch problem is presented in this section. The material is the conventional incompressible isotropic elastic hardening/softening plastic Prandtl-Reuss material. Figure 7.10 shows the two-dimensional finite element representation of the problem geometry and notation. The punch is represented by a strip of elements ten thousand times stiffer than the supporting medium and loading is achieved by a central vertical force P . The strip footing elements correspond to a total width of B while the supporting medium extends $10B$ wide and $5B$ deep so as to preclude any boundary effects.

7.4.1 Continuous case

A perfectly plastic medium—plastic modulus H equals 0—is considered in the first case with the conventional finite element scheme. The load P was applied incrementally to the maximum failure load. In order to avoid problems of convergence, a consistent linearization of the finite element equations as proposed by Simo and Taylor[1985] is adopted. It has been proven that the use of a consistent tangent coefficient matrix derived consistently from the integrated constitutive equation—combined with a closest point projection—results in an iterative scheme which preserves the asymptotic rate of convergence of Newton's method.

The computed load-displacement curve is shown in Figure 7.11. The failure load is captured quite accurately by the numerical solution but one should note that no localization occurs because of the symmetry of the loading, geometry and homogeneity of the material properties. The development of the plastic zone under the punch with increasing settlement

is shown in Figure 7.12. The plastic growth spreads about $2.5B$ deep under the footing and extends one full width B on either side of the punch. It is seen that the plastic growth is slightly less extensive than the one postulated by Hill's slip mechanism.

An attempt to promote localization in the medium was done by making the medium initially inhomogeneous by placing a weak element with plastic modulus ratio $H/2G = 0.048$ beneath the left corner of the rigid footing. The elastic shear modulus is herein denoted by G and the material strength characterized by c , the cohesion, or σ_y^0 , the uniaxial yield strength. Figure 7.13 shows the constitutive relationship relevant to the weak element. It was found that the load-displacement curve basically remains identical to the one obtained for the homogeneous case. Also, the spreading of the yield zones follows sensibly the same trend shown in Fig. 7.12 for the homogeneous case. This shows that localization effects are difficult to capture using the classical finite element formulation—this even if artificial inhomogeneities such as a weak element are introduced.

7.4.2 Discontinuous case

The finite element method with the possibility of an internal discontinuity is next tried out to examine the performance of the proposed method.

The domain of interest is initially discretized with ordinary elements and the bifurcation criterion is checked at every loading step. Once bifurcation is detected, the standard element is replaced by the discontinuous one, and the stress-strain as well as the other history dependent state quantities must be then extrapolated from original Gauss points into the new integration points required by the new element. A detailed description of the integrating scheme is given in Appendix B. Alternatively, one could possibly find the band orientation and its location from a preliminary analysis, and then place the discontinuous element there from the beginning of the analysis. However, this alternative method does not represent the actual locations of the shear band segments as they develop

during loading because the determination of the path is history dependent. The direction the next band segment takes depends on the already in place previous bands in the mesh.

In the present study, as the developments are still at a preliminary stage, the complexities involved in locating and constructing the shear band, as it evolves in the mesh, are by-passed by using the simple discontinuous triangular element presented in Chapter 4. As such, it suffices only to check bifurcation criterion at the centroid (also single Gauss point) of the element. The very first shear band in the analysis is made to pass through the centroid of the element. For subsequent loadings, the newly formed shear band in the adjoining element is simply shifted and made to connect with the leading tip of the previous band since the stress-strain quantities are supposed to be constant over the element just prior to localization.

Bifurcation conditions which emerge from equation (3.7) are numerically checked at each Gauss integration point during the loading process. Details of the numerical procedure were previously covered in Section 6.3 of this thesis. A shear band is precisely located in the weak element, and an inclination of 4.5° with respect to the vertical is computed. Conjugate shear band directions are usually obtained. The direction which is consistent with the prevalent boundary conditions is chosen. However, in less obvious situations, the strain rate prior to localization and the one at the onset of bifurcation are compared. The direction which gives more or less the same strain rate at the point under consideration just before bifurcation is considered as the one the shear band will eventually follow. This should be equivalent to choosing the direction which produces the most dissipation through inelastic dissipation in the band, in other words, the one which minimizes the potential energy of the system.

As soon as the bifurcation criterion is satisfied the discontinuous shape functions are triggered with relative displacements along the shear band following a simple Coulomb contact law with a cohesive strength of 10 units, and no frictional resistance. The normal stiffness of the shear band is made of the order of 10^8 units to avoid separation of the band,

and a shear stiffness of 10^5 units is chosen, which is within the same magnitude of the modulus of the bulk material. The features of the governing constitutive relationship for the shear band is given in Fig. 7.14.

Figure 7.15 shows the progression of the shear band at three selected stages, as the footing load is gradually increased. At an early stage of the punch, Figure 7.15a, four elements have already bifurcated, and the shaded area shows the yield zone. It is clear that yielding localizes in the vicinity of the shear band, although some yielding also occurs beneath the right corner of the footing. This is probably due to stress concentrations at the corners.

As the load is further increased (Figure 7.15b), more yielding occurs and the plastic zone migrates to adjacent elements as the tip of the band penetrates further into the mesh. The resulting footing load must increase since plastic deformations can still take place—at least in the neighbourhood and in the shear band. There is a tendency for the ambient zone to plastify together with the shear band.

At an advanced stage of the loading (Figure 7.15c), the plastic zone has now become quite extensive, but is still clustered around the shear band. Consequently, this provokes a levelling-off of the load-displacement curve. Since, the achievement of a stable solution becomes more and more difficult, displacements are instead prescribed as opposed to loads. Figure 7.16 illustrates the kinematics of the problem with the shear band fully developed. Note the discontinuous nature of the displacement field, and the tilt of the footing to accommodate the rotational nature of the kinematics.

The curves of slip displacements along the shear band at selected normalized footing displacements are plotted in Fig. 7.17. The results show that the slip displacements are significantly affected by the presence of kinks between two connecting shear band segments. The slip displacement tends to drop at these kinks, but the general trend follows a gradual decrease of slip towards the tip of the band where there is no movement. As the tip advances in the mesh, the slip displacements generally increase as shown by the shift of

the curves. When the band has daylighted, it is noticed that very little slip occurs in the upper segment near the free surface. There is a phenomenon of locking of the mesh in the lower segment where the material is squeezed.

Figure 7.18a shows the fully developed shear band together with the Prandtl's slip lines. The shear band computed is very close to those slip lines, thus indicating that the model can capture similar mechanisms as postulated by Prandtl. The behaviour of the shear band can be elucidated by examining the distribution of traction forces along the interface, as shown in Fig. 7.18b. It is noted that the force distribution trend is consistent with the strength of the shear band. In regions of the shear band located near point A, considerable slip has occurred such that the corresponding traction force is kept to a limiting value of 10 units, the strength of the shear band. However, the segments of the shear band near point B undergo less slippage, to such an extent that the corresponding traction forces are low. It is observed that this phenomenon is somewhat disturbing due to the fact that slippage should have been uniform throughout the shear band as it daylights. This is attributed to the fact that there are kinks at the connections of the shear band segments at locations with an abrupt change in orientation. These kinks seem to hinder slippage such that further deformation in the form of plastic flow spread in the ambient region instead of in the band itself. The phenomenon apparently produces a spurious plastification which appears to lead to an unrealistically high footing load.

The new load-displacement curve is finally shown in Figure 7.19. The bearing capacity is marginally lower than the one obtained without any shear band because of the allowance made for a discontinuous displacement field and the tilt of the footing. Also, it is thought that the low cohesive strength of the shear band may be a contributing factor which led to such a low bearing capacity value. It seems that a substantially lower value should have been obtained considering the low resistance of the shear band compared to the ambient material strength. This is partly due to the problem of locking of slippage at kinks between two shear band segments, which makes the surrounding material yield instead of

constricting plasticity into the band. Thus, the introduction of this error together with the nature of the analysis lead to a bearing capacity which is higher than the theoretical limit load and this is consistent with an upper bound solution.

The load-displacement relation seems to show some softening in the ultimate range, but this may be apparent and purely due to the switching of scheme from loading to prescription of displacement. The last point on the load-displacement curve in Figure 7.19 represents an equilibrium state which has not fully converged, most probably due to the shear band having daylighted.

The effective plastic strain history for a point 'A' in the element number 44 (see Fig. 7.18) found just below the left hand corner of the footing is given in Figure 7.20. During the initial phase, both the strain fields in the localized and non-localized zones are identical since there is no shear band. During subsequent deformation, the effective plastic strain for a point in the shear band increases steadily, while plasticity is less extensive for a point outside the localized zone. In the localized zone, the increase in effective plastic strain indicates a continuous plastification. On the other hand, in the non-localized zone, the effective plastic strain increases slowly but remains at a relatively low value when compared with the extent of plasticity in the shear band. It seems that one would expect very low plastic strains or values close to zero in the non-localized zone so as to produce an unloading phenomenon with a decrease in effective stresses. However, in this present analysis, there is still some residual plastic strains in the non-localized zone due to the locking phenomenon occurring at kinks. Even though this shortcoming may look serious in the sense that it may mask the influence of localization, Fig. 7.20 certainly illustrates the general tendency of having higher plastic strains in the band and less extensive plasticity in the ambient region. This is a definite improvement over the conventional (continuous) analysis in which the plastic strains would steadily increase in a diffuse way with loading history.

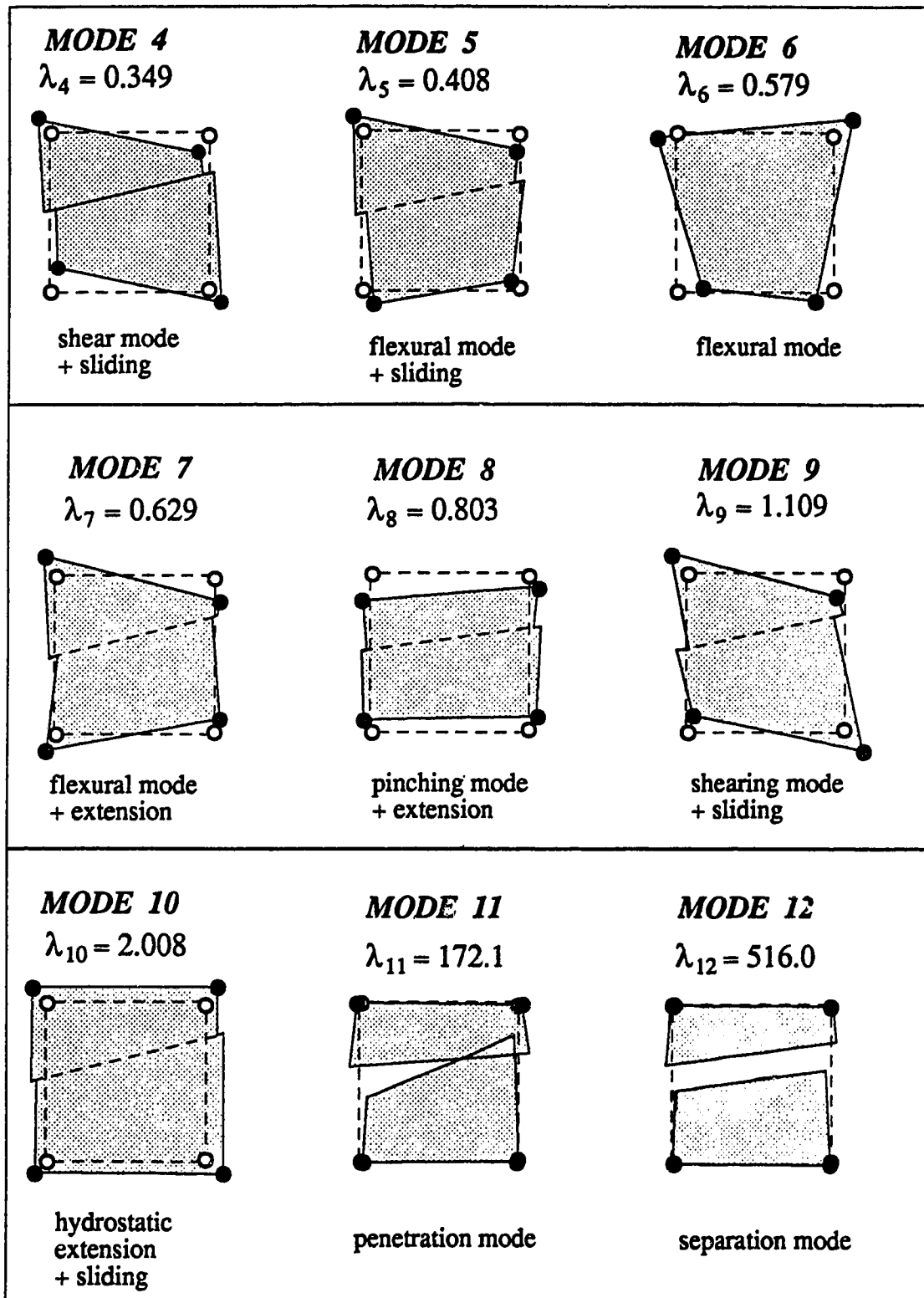


Figure 7.1 Non-zero eigen-modes for Shear Band Element QD4 (option 1) in plane strain

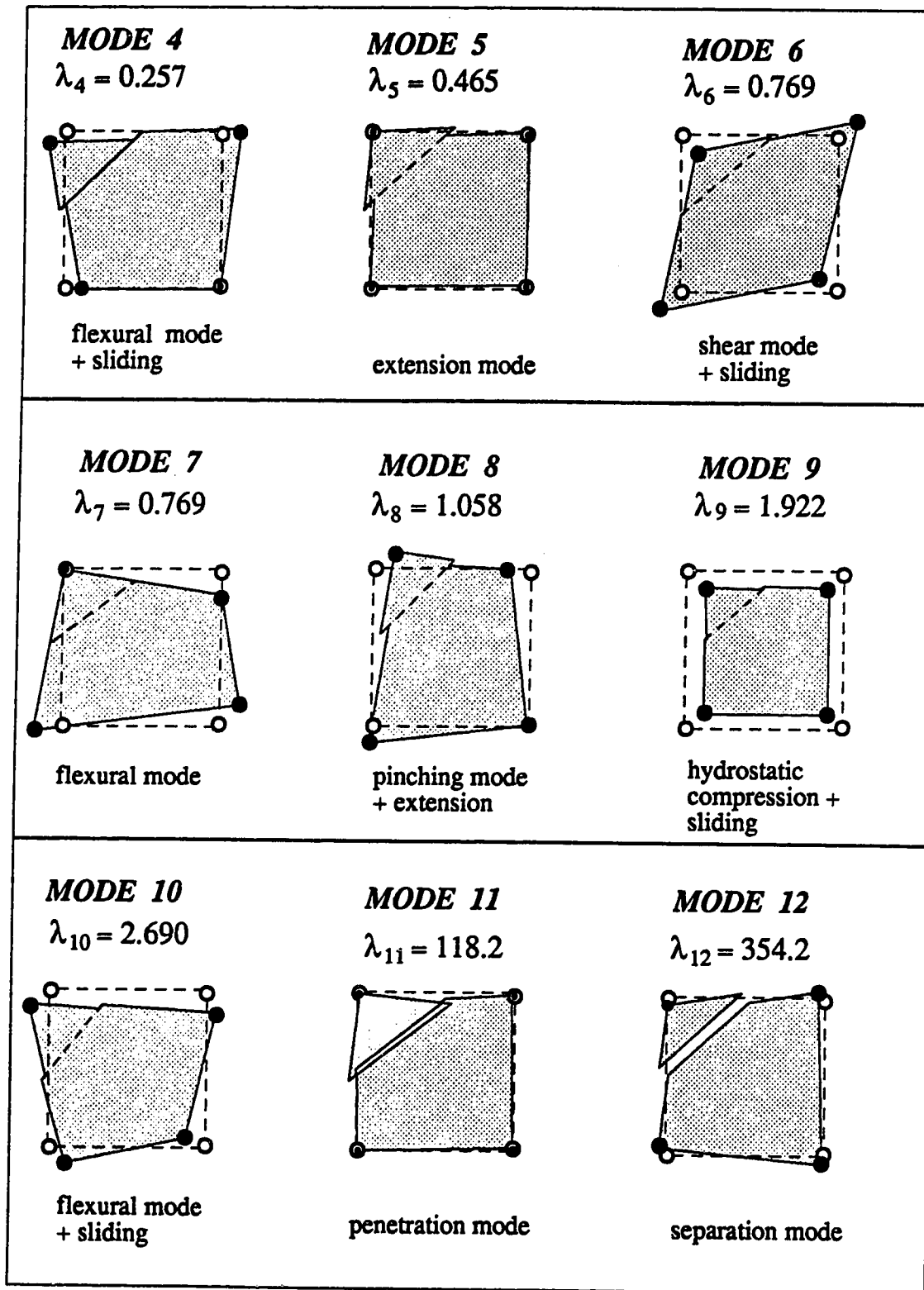


Figure 7.2 Eigen-modes for Shear Band Element QD4 (option 2)

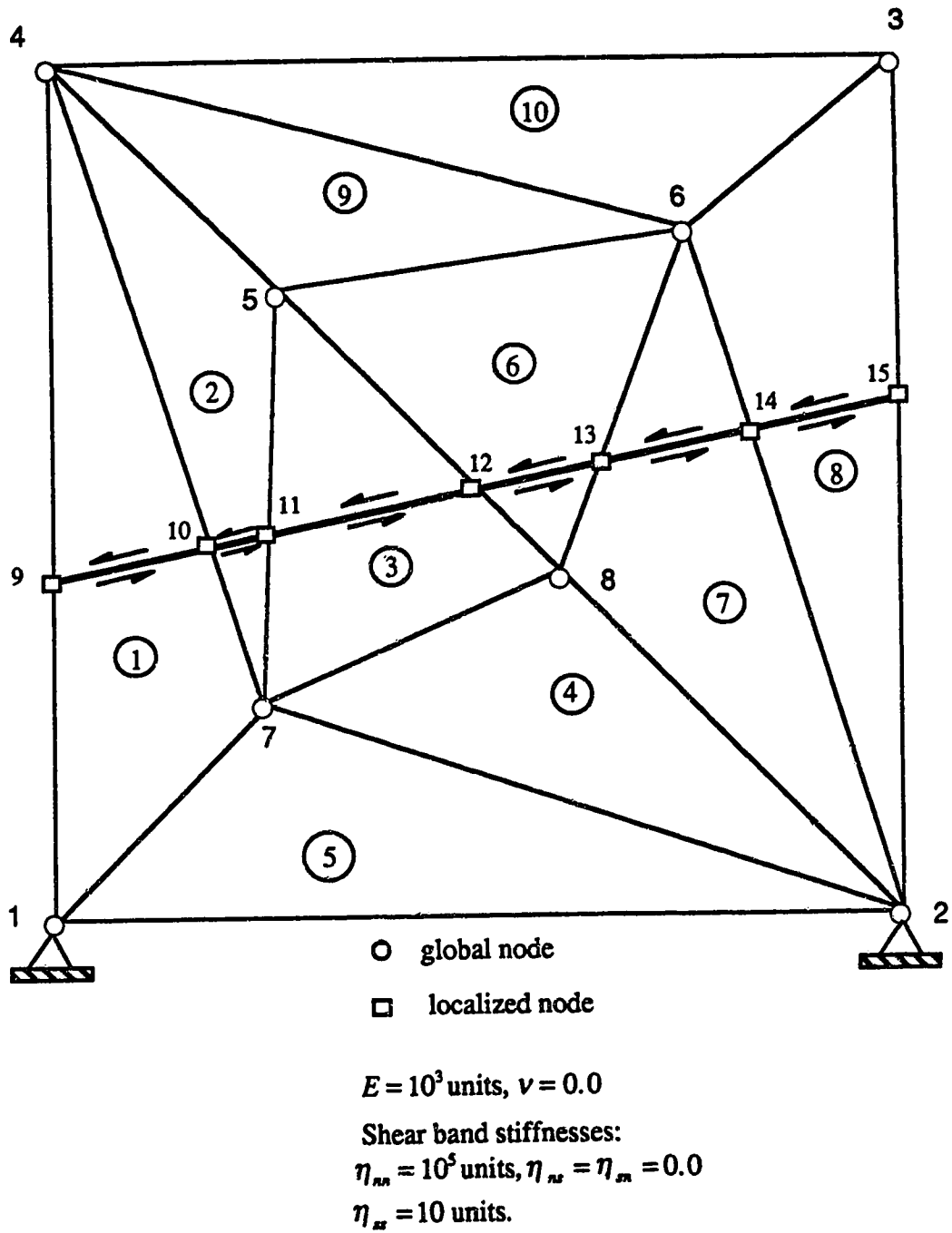


Figure 7.3 Patch of triangular discontinuous elements

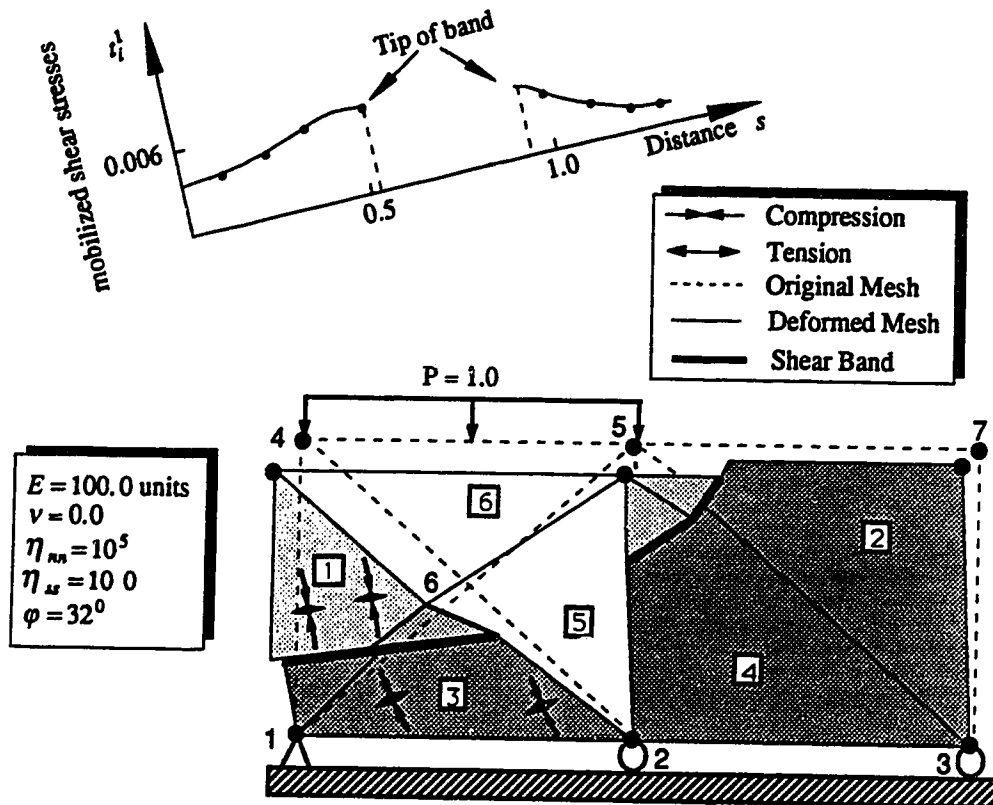


Figure 7.4. Finite element schematization of slippage along shear band

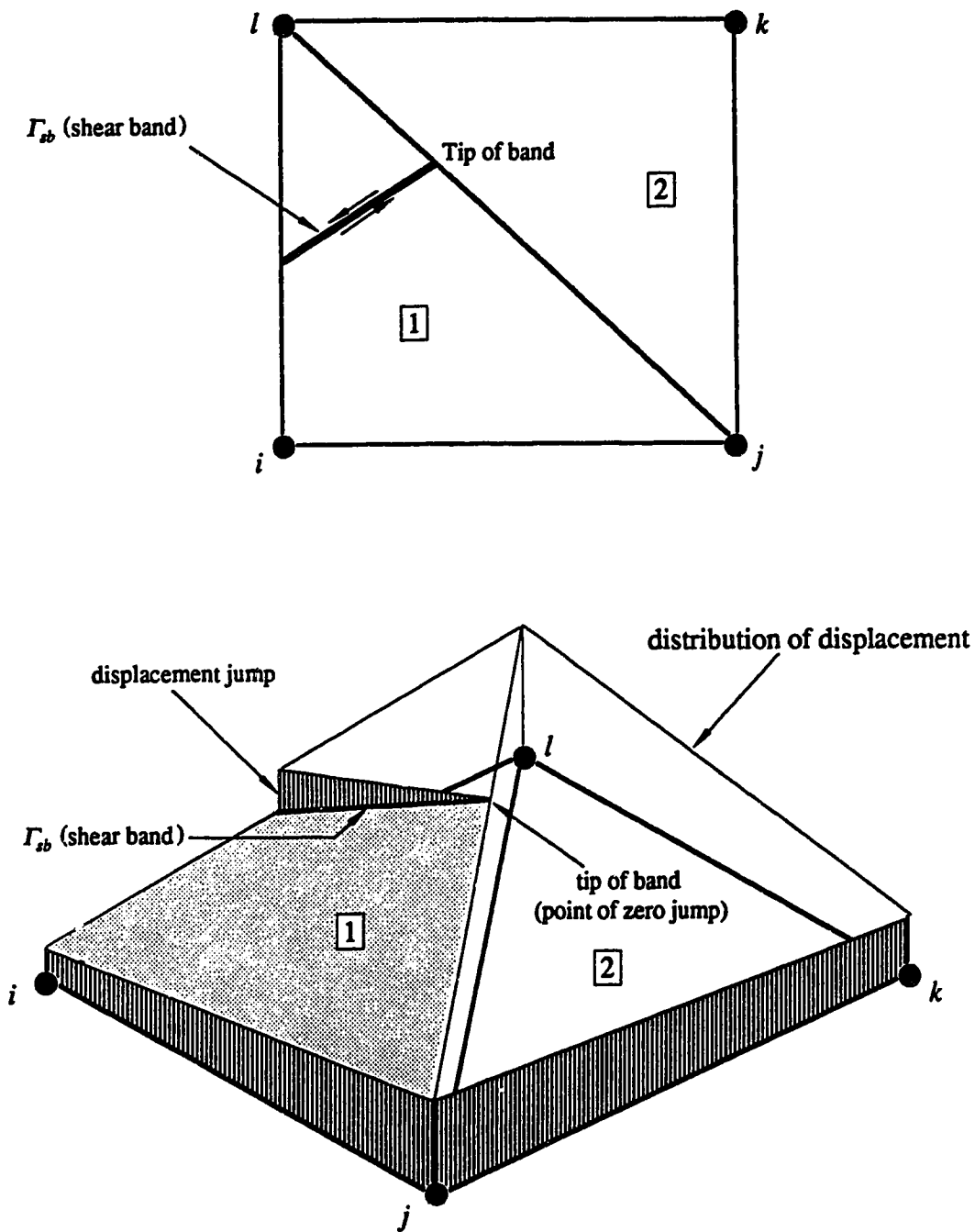


Figure 7.5 Condition of displacement field compatibility at the junction between discontinuous and continuum elements

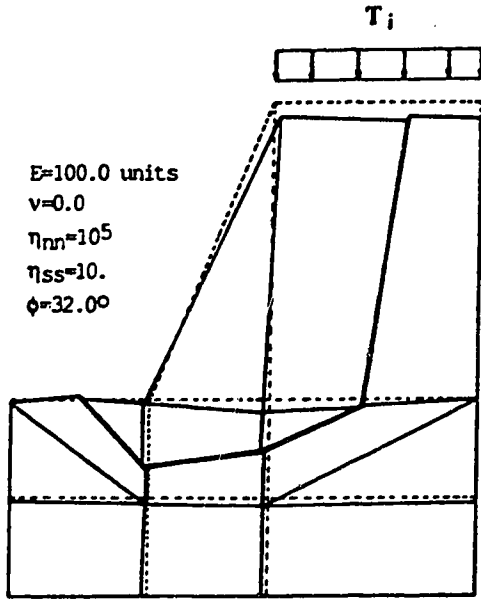


Figure 7.6 Kinematics of embankment under shear band mode of deformation

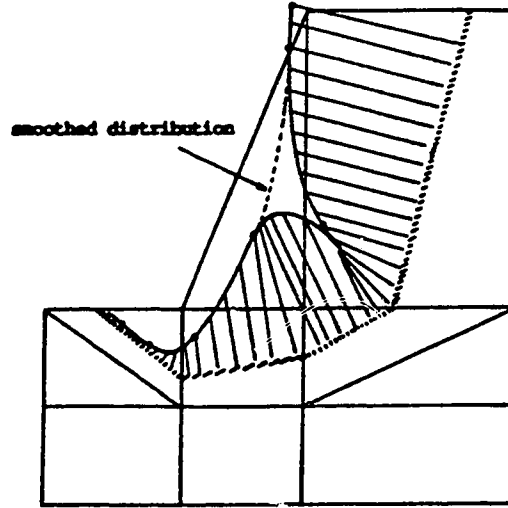


Figure 7.7 Distribution of internal tractions along shear band

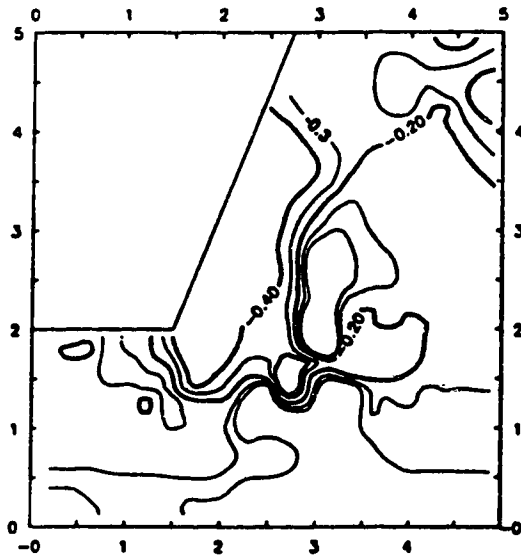


Figure 7.8 Contours of shear strains (%) as computed from proposed formulation

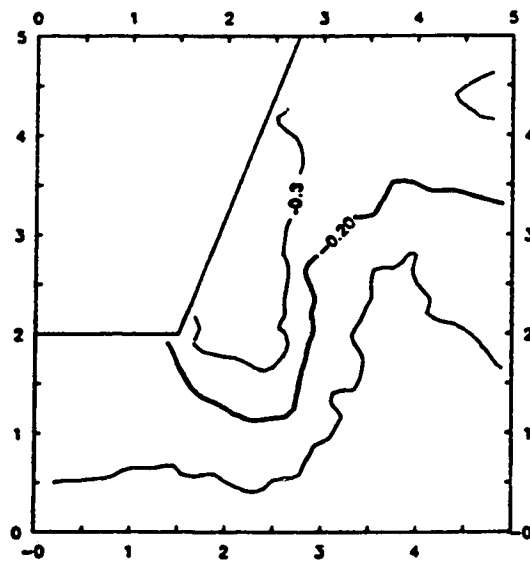


Figure 7.9 Contours of shear strains (%) as computed from conventional finite element method formulation

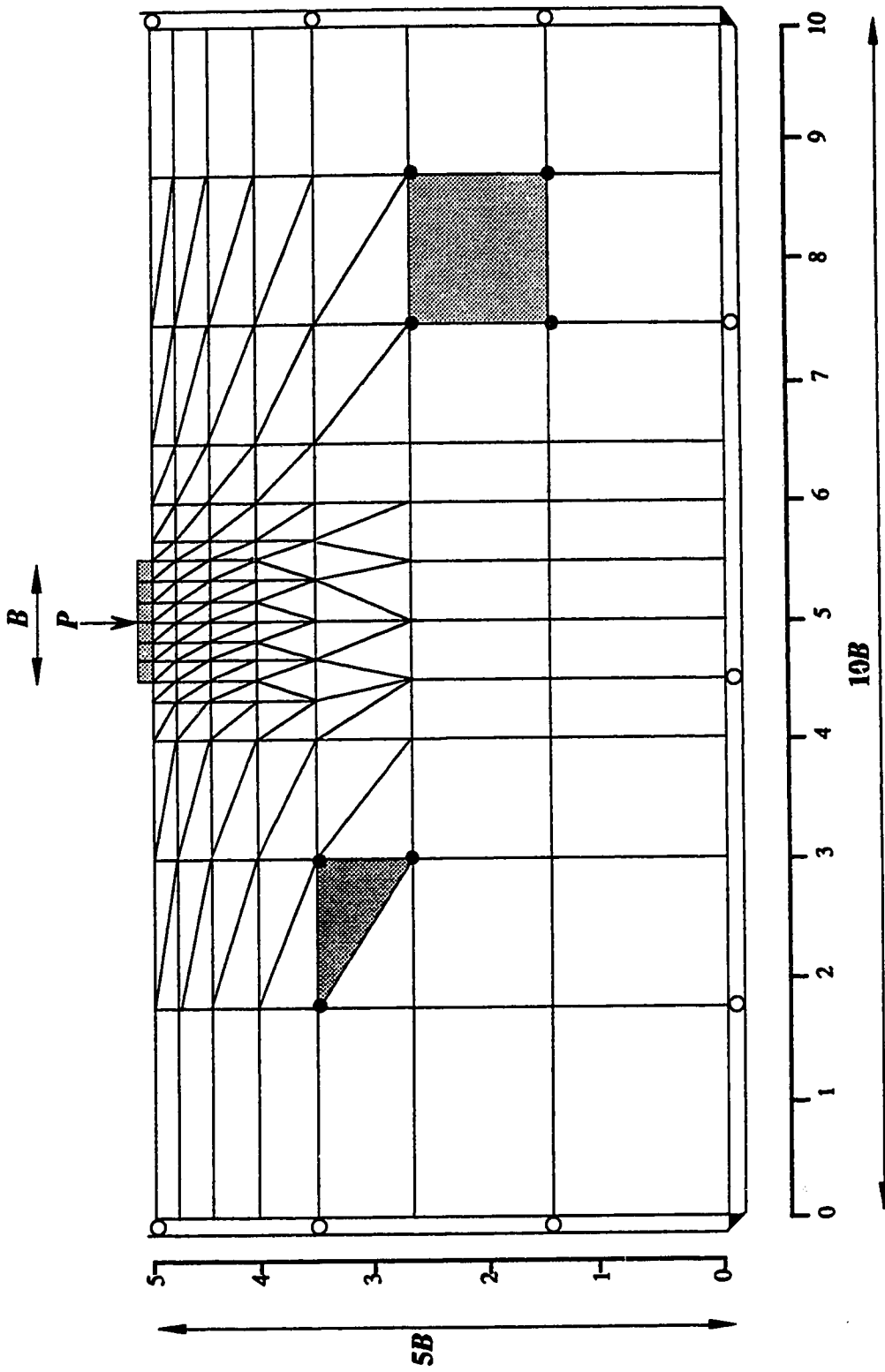


Figure 7.10 Rigid punch problem: finite element mesh

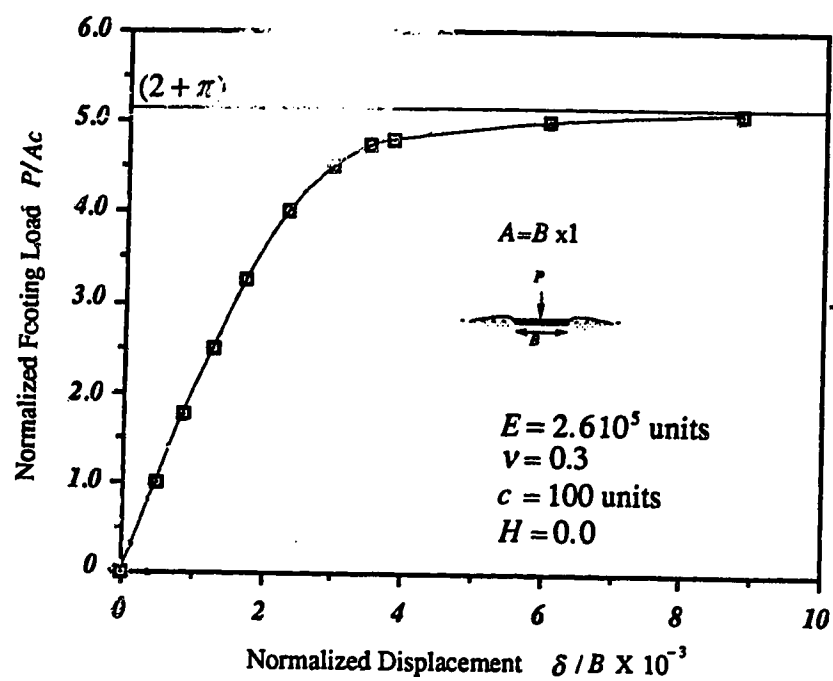


Figure 7.11 Load-displacement curve for rigid footing

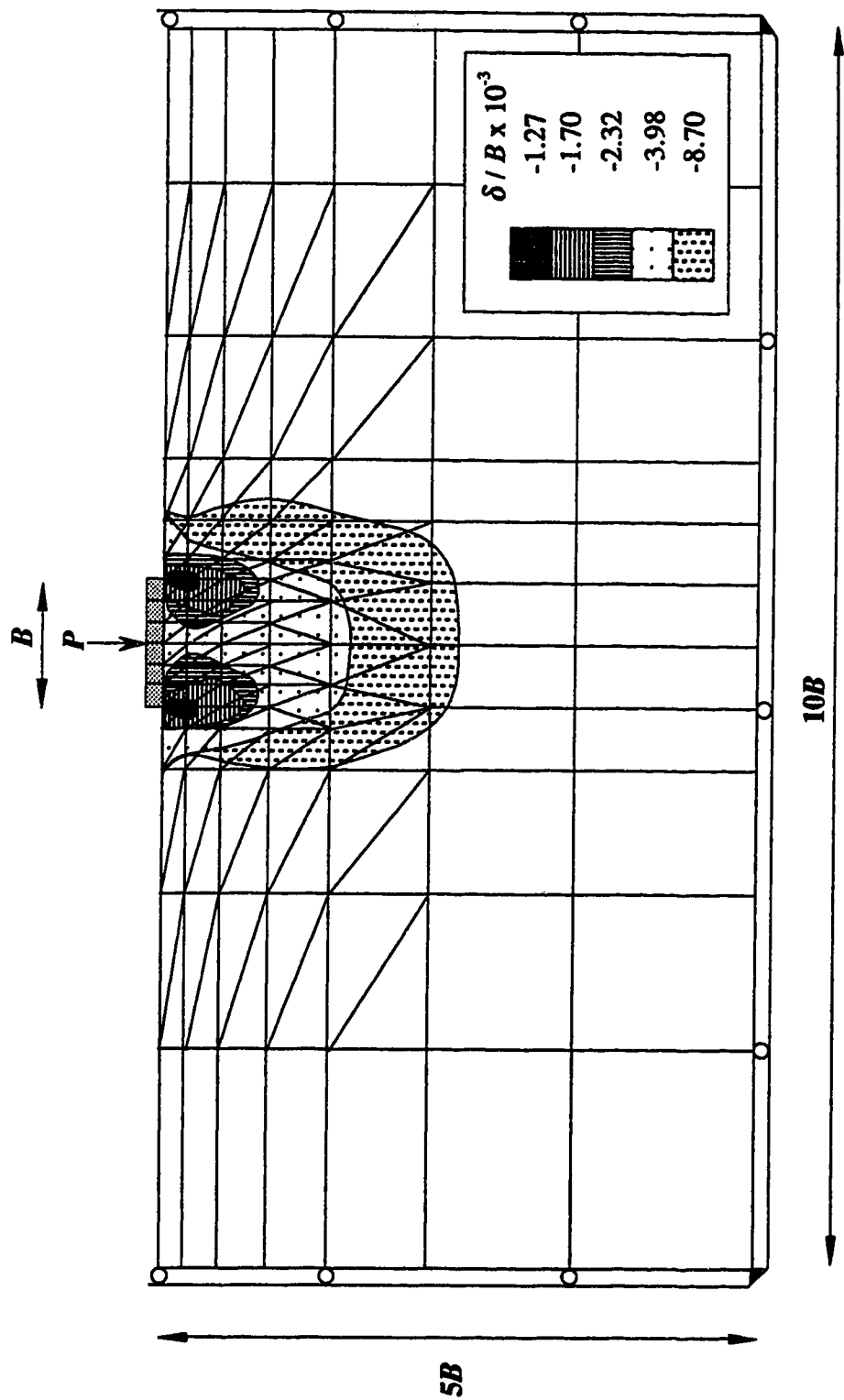


Figure 7.12 Rigid punch problem: growth of plastic zone

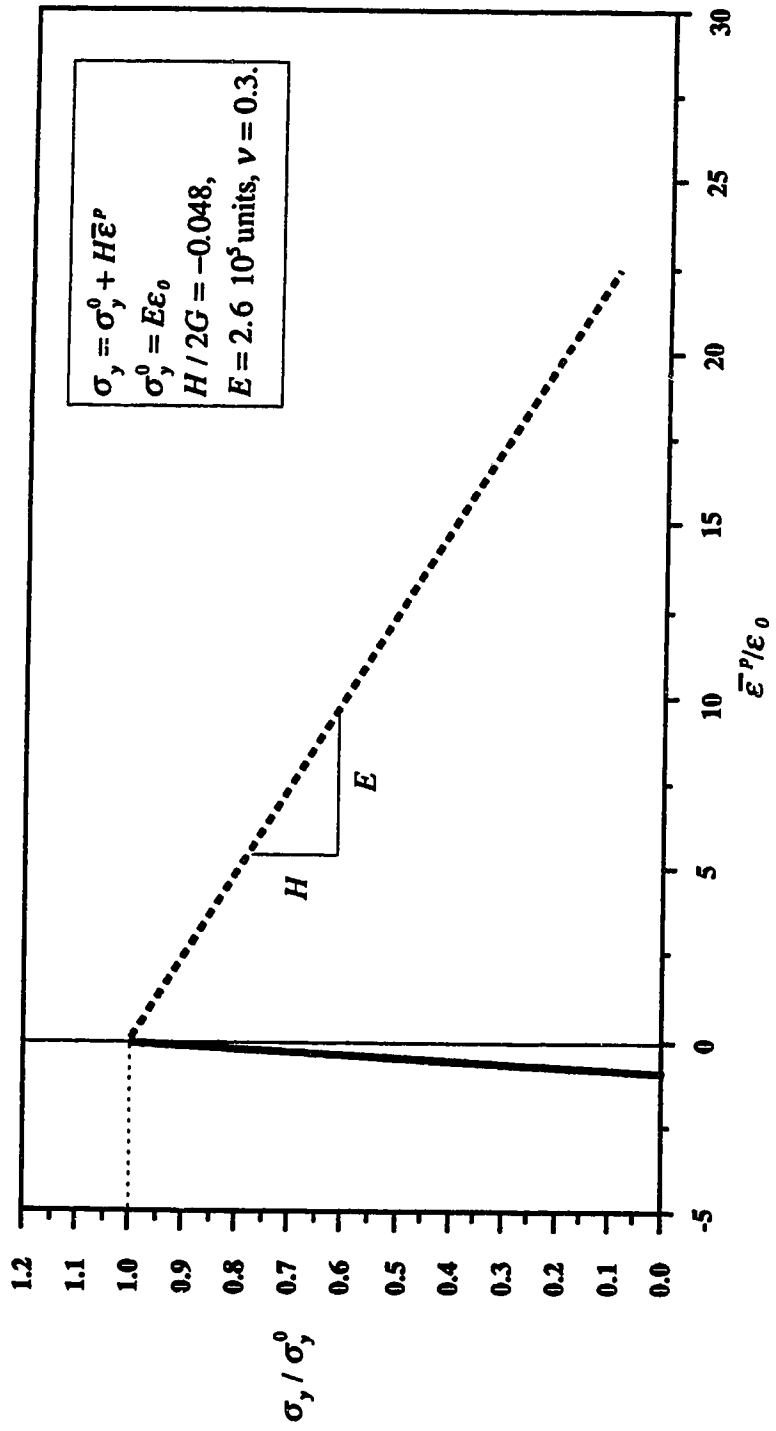
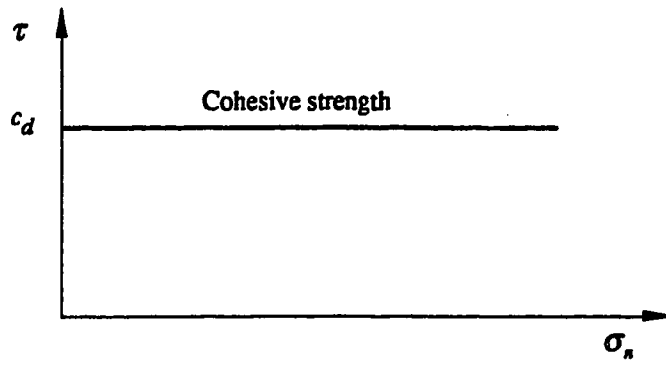
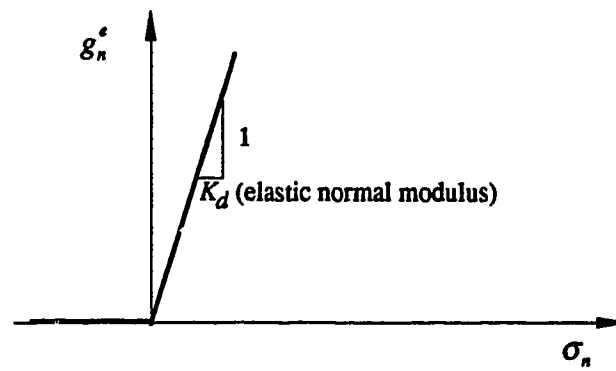


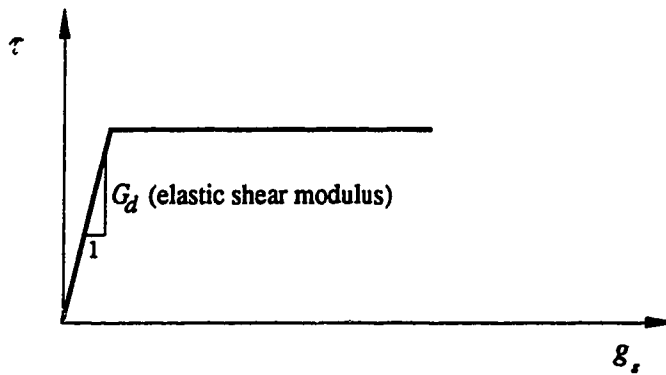
Figure 7.13 Constitutive relationship for strain-softening behaviour



(a) Shear stress versus normal stress

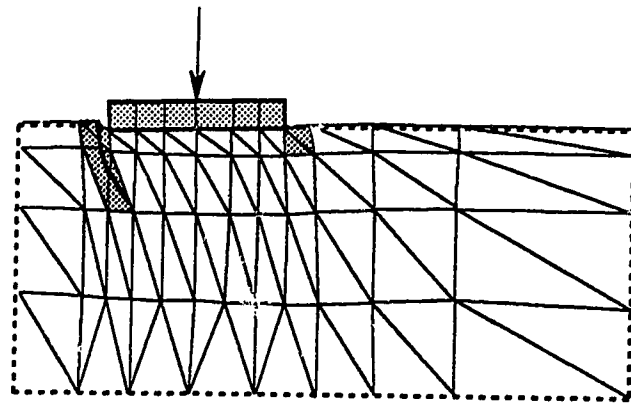


(b) elastic closing versus normal stress

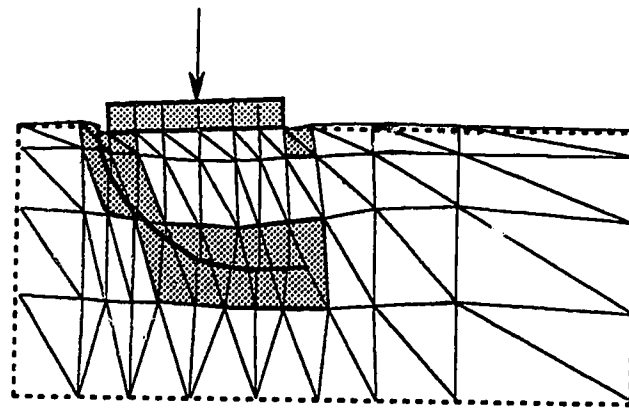


(c) shear stress versus tangential slip displacement

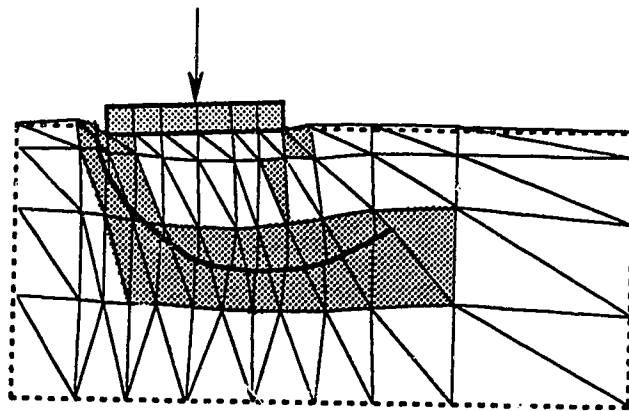
Figure 7.14 Constitutive law for shear band



(a) $\delta / B = 2.105 \cdot 10^{-3}$



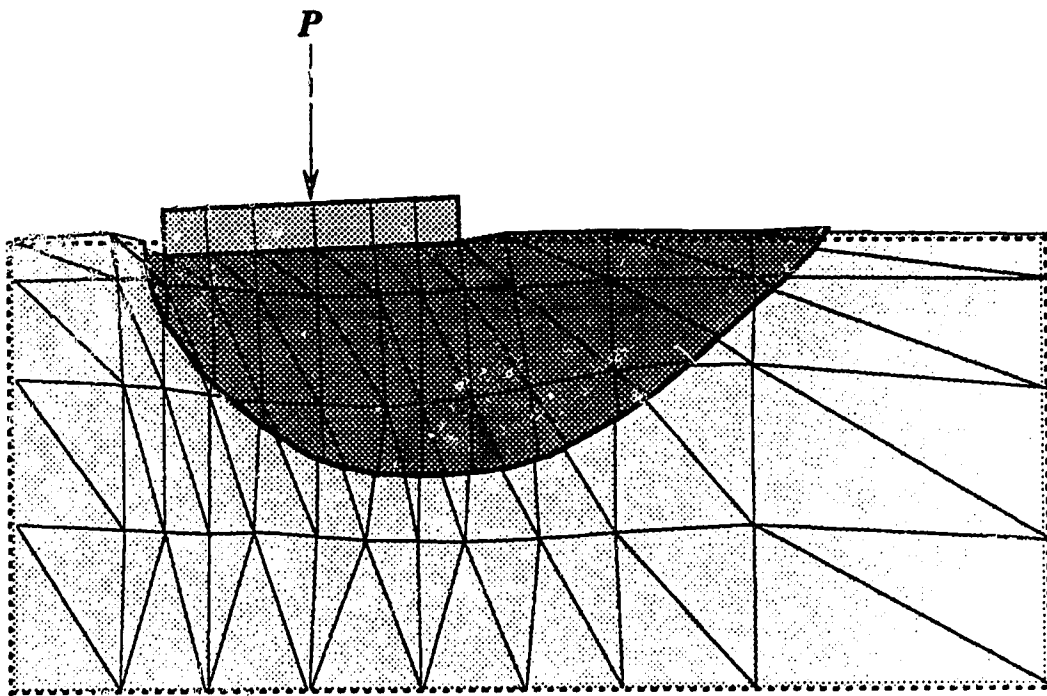
(b) $\delta / B = 3.680 \cdot 10^{-3}$



(c) $\delta / B = 4.842 \cdot 10^{-3}$

Note that only part of the whole mesh is shown in all three diagrams

Figure 7.15 Progression of shear band during loading history



Note that only part of the whole mesh is shown

Figure 7.16 Kinematics of rigid punch problem using proposed method

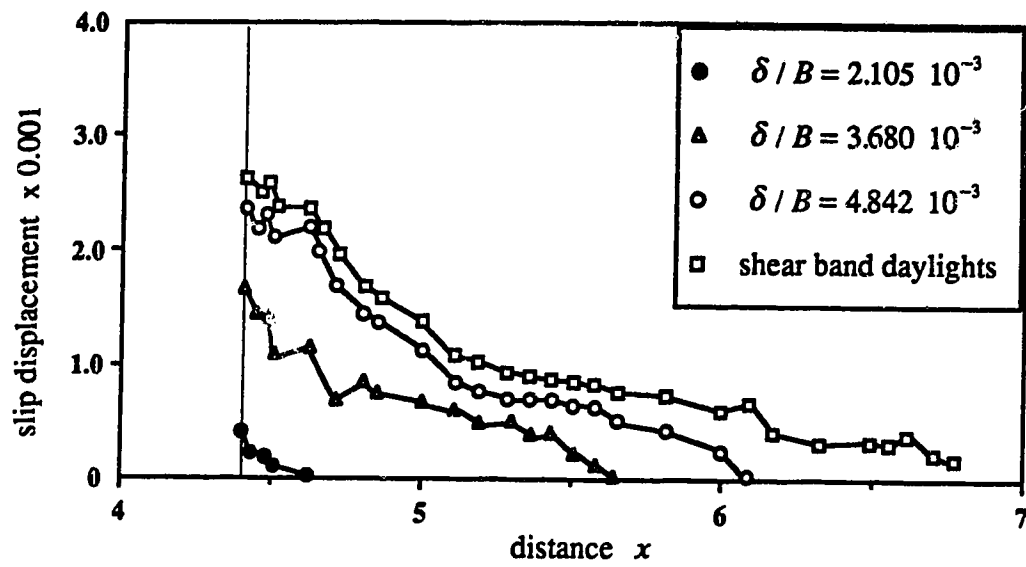
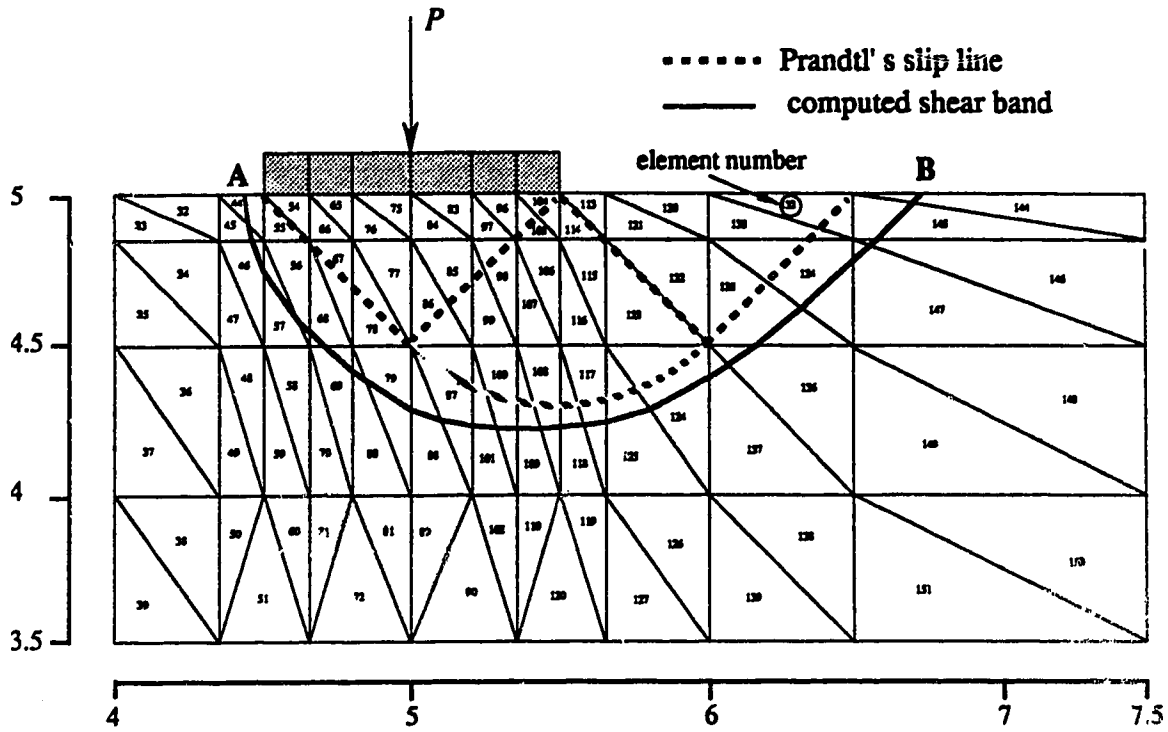
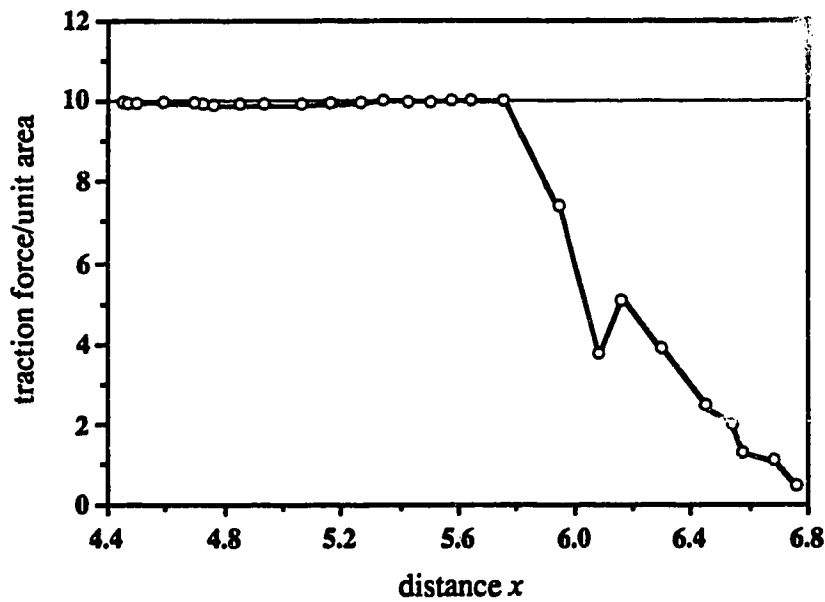


Figure 7.17 Evolution of slip displacement along shear band with loading history



(a) part of finite element mesh with fully developed shear band



(b) shear resistance along shear band AB

Figure 7.18 Variation of shear resistance along shear band

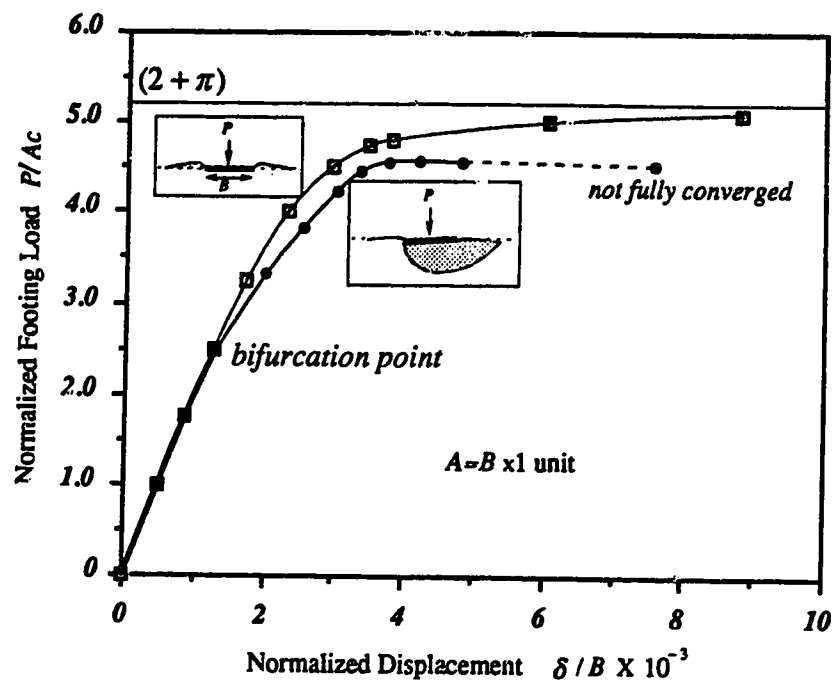


Figure 7.19 Load-displacement curve for rigid footing with localization

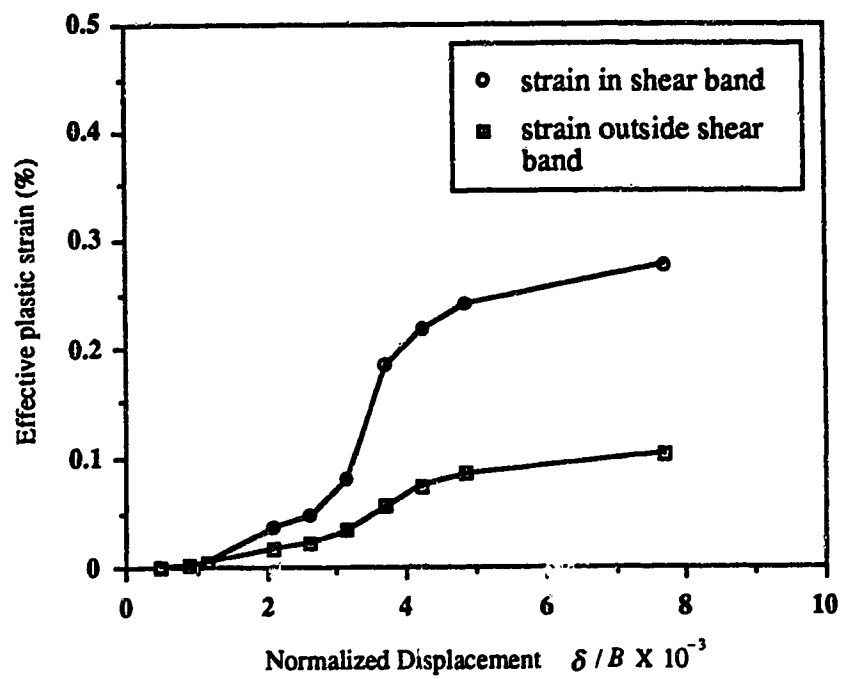


Figure 7.20 Effective plastic strain for element 44 below left hand corner of footing

Chapter 8

Conclusions and Recommendations

8.1 Conclusions

A method has been developed by which a shear band in a soil medium can be adequately modelled in a numerical analysis. The approach consisted of writing a modified principle of virtual work equation which accounts for discontinuities in the domain of interest. The formulation was then supplemented with governing fluid flow equations for a fluid saturated porous medium. Controlling field variables in the variational principle became continuous displacement, discontinuous displacement and pore fluid pressure. The finite element discretization led to the development of a special 2-D element with implicit discontinuity in its interpolation function to obviate the need to update the mesh topology during progression of an internal discontinuity surface.

The derived formulations were implemented into a finite element code to demonstrate the validity of the proposed modelling technique. In this thesis, only the drained case has been implemented—fluid pressures were excluded, and only global and slip displacements were retained as principal variables. The plasticity equations— J_2 plasticity—for the bulk material have been solved by a Newton Raphson algorithm using

the notion of consistent tangent operator for rate independent elasto-plasticity which resulted in an asymptotically quadratic convergence rate. Post peak failure—engendered by the spreading of the shear band—was governed by a simple interface relationship for rupture with constant cohesive strength. In the special shear band element developed in this study, the stresses at the shear band interface were made continuous and therefore equilibrium of internal tractions was satisfied. This feature, due to the superiority of the shape functions used, has a definite advantage over the traditional joint element where stresses being not continuous often lead to instability in convergence.

According to the various numerical examples presented, the following conclusions could be derived from the results. First of all, the developed formulation for the simulation of a discontinuous body is theoretically sound. It was shown from an eigen value analysis in elasticity that the specially developed elements were very conducive in capturing the slip mechanism produced by an internal shear band. Also, the patch test ensured the stability of the shape functions for an assembly of arbitrarily arranged elements. It was further demonstrated that discontinuous behaviour could be captured whenever shear banding occurred with deformations subsequently localized in a restricted zone. Besides modelling shear bands, the convergence of the elasto-plastic solution obtained for the bulk material by using the consistent tangent operator was found to be very efficient and proved to be quadratically convergent.

Secondly, the model provides a framework for incorporating bifurcation concepts for the inception of shear bands. A procedure has been devised for the detection of shear bands by which the equations can be solved analytically in the program in an efficient fashion. The classical punch problem was analyzed, and the model demonstrated that the possibility of a shear band spreading into the supporting medium can lead to a consistently lower bearing capacity. This bears an important consequence on the validity of the classical finite element method analysis of structures undergoing localization. The approximation to a diffuse type of yielding may lead to an over-estimation of the bearing capacity in contrast

to a more realistic case in which yielding, taking place in a localized fashion, leads to a lower collapse load.

Thirdly, the model accounts for dissipation of energy even with a vanishing zone of localization because of the consistency of the variational principle. It is notorious that classical models, fail to do so and consequently tend to make the localization analysis mesh dependent—different levels of mesh refinements would give different localization patterns with different amounts of dissipation. Since the proposed formulation avoids this shortcoming, it can be regarded as a non-local model—prescribing an arbitrary thickness for the band in the equations provides the internal characteristic length. In this research work, a shear band thickness of unity was used. It is difficult to determine this parameter experimentally: anyway its evolution with loading history is not fully known. Finally, it is emphasized that even though the model is non-local, mesh dependency inherited from the finite element discretization/linearization of the variational principle for the evaluation of stresses cannot be avoided.

The above developments and results are significant because for the first time, to the knowledge of the author, a consistent numerical approach has been established to account for the development of a shear band in a discrete manner (not in a smeared fashion) in a soil medium.

8.2 Recommendations for future work

The modelling technique developed in this research represents a starting basis for the analysis of shear bands in geological media. However, the model is still in an embryonic state, and in order to fully realize its potential application to real engineering problems, a number of additional issues should be addressed. It is necessary to include in the analysis, the formulation of an element with an internal curvilinear shear band to better describe the geometry, and hence the kinematics of the shear band. In this research effort, the shear

band is approximated by linear segments along which the slip displacements (jumps in displacement) vary linearly. This restricts the formation of a shear band for which slip displacements are zero at both tips—the situation occurs for an isolated shear band in the interior of the finite element mesh. Also, linear shear band elements tend to produce a locking phenomenon at kinks produced at the junction of two adjoining tips of the band. This locking problem may prevent plastic deformations to develop extensively in the shear band by forcing the ambient material to plastify rather than unload elastically. An expedient solution to the above shortcoming is to refine the mesh or resort to a higher order shear band element.

A possible avenue of research leading to the improvement of the model is to contemplate the possibility of formulating a stress-displacement or hybrid shear band element. It is well-known that using a displacement type of formulation does not ensure continuity of stresses at the element boundaries. Since at the interface formed by the shear band, the stress vector has to be continuous, the displacement type of formulation may be awkward. The solution lies in writing a hybrid formulation, or imposing some internal constraint in the form of continuity in displacement gradient in a certain direction at the discontinuity front. The latter technique was employed in this research.

Stress and localization induced anisotropy are not included in the model. In other words, as the shear band forms, the bulk material surrounding the shear band does not become anisotropic due to damage. This could be partially solved by considering a damage based formulation. Also, the model is restricted to proportional loading conditions under which the behaviour of the structure changes smoothly, and not in a chaotic manner.

Although the herein algorithm—by which the shear band position once determined from trial stresses, is not corrected as the stress regime changes—works for simple cases, the model still needs considerable enhancements with regard to the correction of the shear band position with loading history. It seems that the problem of self correction for the shear band position is very similar to the search of a free surface in the analysis of unconfined

flow. However, it is thought that the propagation of the shear band cannot be fully automatized and has still to be carried out manually in the sense that at each load step, the shear band evolution has to be visually checked. Problems specially arise when there are conjugate directions for the shear band orientation. In this thesis, the orientation which is more obvious to the boundary conditions is chosen. However, it seems that the use of a more profound criterion for the choice of the correct orientation is preferable. One possibility could be evaluating the entropy of the mechanical system according to the second law of thermodynamics: for a change in state the second order change in work or entropy must be positive. Therefore to achieve a stable state, the second order entropy change must be negative. Using this concept, the shear band direction which maximizes the entropy or energy dissipation—thus minimizes the Helmholtz free energy—will be the one which prevails.

Another issue which is worth examining is the consideration of the possibility of unifying the concepts of shear banding with tensile fracture. In this research work, it has to be emphasized that the fracture aspect, i.e possibility of the shear band opening in a tensile mode, has been overlooked and tacitly solved by prescribing a very high normal stiffness to the shear band. In the case of fracture, the driving mechanism which establishes the crack advance is the tip where the material undergoing degradation provokes a release of energy whose magnitude is congruous with the one involved in extending the crack by a certain length. In contrast, the mechanism behind the shear band mode of failure is rather associated with a material instability phenomenon.

In closure, the development of a more robust algorithm for the search of equilibrium states could result in better solutions. In this thesis, close to ultimate loads, displacements are prescribed instead in order to achieve a solution. Perhaps, a solution strategy such as the arc length method could be used. This treatment would seemingly give better results for more difficult problems than the ones examined in this thesis.

REFERENCES

- Arthur, J.R.F., and T. Dunstan, [1982], "Rupture layers in granular media", *IUTAM Symposium on Deformation and Failure of Granular Materials*, Delft, pp. 453-459.
- Bazant, Z.P and Feng-Bao Lin, [1988], "Non-local yield limit degradation", *Int. J. Num. Meth. Engng.*, 26, pp. 1805-1823.
- Bazant, Z.P and G. Pijaudier-Cabot, [1987], "Modelling of distributed damage of non-local continuum with local strain", In *Numerical Methods in Fracture Mechanics, Proceedings of the 4th. International Conference held at San Antonio, Texas, USA*, A.R Luxmoore, D.R. Owen, Y.P.S Rajapakse and M.F Kanninen, Editors, pp. 411-432.
- Bazant, Z.P and G. Pijaudier-Cabot, [1988], "Non-local continuum damage, localization instability and convergence", *J. Applied Mechanics*, 55, pp. 287-293.
- Belytschko, T., J. Fish, and B.E Englemann, [1988], "A finite element with embedded localization zones", *Comp. Meth. in Appl. Mech. and Eng.*, 70, pp. 59-89.
- Bicanic, N., E. Pramono, S. Sture and K.J Willam, [1985], "On numerical prediction of concrete fracture localization", *Proceedings of the NUMETA Conference*, Ed. J. Middleton and G.N Pande, Balkema, Rotterdam, pp. 385-391.
- Biot, M.A., [1941], "General theory of three dimensional consolidation", *Journal of Applied Physics*, 12, pp. 155-164..
- Bishop, A.S., G.E. Green, V.K Garga, A. Andersen, and J.D Brown, [1971], "A new ring-shear apparatus and its application to the measurement of residual strength", *Geotechnique*, 21, No. 4, pp. 273-328.
- Boulon, M., and C. Plytas, [1986], "Soil structure directionally dependent interface constitutive equation application to the prediction of shaft friction along piles", In

- 2nd. Int. Symp. on Num. Models in Geom.*, ed. G.N Pande and W.F Van Impe, M. Jackson & Sons, Cornwall, England, pp. 43-54.
- Burridge, P. B [1987], *Failure of Slopes*, Ph. D thesis, California Institute of Technology, Pasadena, California, USA.
- Chaboche, J.L., [1981], "Continuous damage mechanics—A tool to describe phenomena before crack initiation", *Nucl. Eng. Des.*, 64, pp. 233-247.
- Chan, D.H.K, [1985], *Finite Element Analysis of Strain-Softening Material*, Ph.D thesis, University of Alberta, Edmonton, Alberta.
- Chazy, C., and P. Habib, [1961], "Les piles du quai de Floride", *5ème. Congrès International de Mécanique des Sols*, Paris, Com. 6/27, 669.
- Coulomb, C.A., [1773], "Essai sur une application des règles de maximis et minimis à quelques problèmes de statique relatifs a l'architecture", *Mém. Académie Royale des Sciences*, Paris, 3, p.38.
- Eringen, A.C., and D.G.B Edelen, [1972], "On non local elasticity"; *International Journal of Engineering Science*, 10, pp. 233-248.
- Goodman, R.E., R.L Taylor and T.L Brekka, [1968], "A model for the mechanics of jointed rocks", *Journal of the Soil Mechanics and Foundation Engineering Division, ASCE*, 94, SM3, pp.637-659.
- Hadamard, J., [1903], "Leçons sur la propagation des ondes et les équations de l'hydrodynamique", Paris.
- Hansen, B., [1958], "Lines ruptures regarded as narrow rupture zones, basic equations based on kinematic considerations", *Proceedings of Conference on Earth Pressure Problems*, Brussels, Belgium, pp. 39-51.
- Hill, R., [1958], "A general theory of uniqueness and stability in elastic-plastic solids"; *Journal of the Mechanics Physics and Solids*, 6, pp. 236-249.

- Hill, R., [1962a], "Acceleration waves in solids"; *Journal of the Mechanics Physics and Solids*, **10**, pp. 1-16.
- Hill, R., [1962b], "Constitutive laws and waves in rigid-plastic solids"; *Journal of the Mechanics Physics and Solids*, **10**, pp. 89-98.
- Hoeg, K., [1972], "Finite element analysis of strain softening clay", *Journal of the Soil Mechanics and Foundation Engineering Division, ASCE*, **98**, SM1, pp. 43-58.
- Hungerford, T.W., [1964], *Algebra*, Springer-Verlag, New-York.
- Ichikawa, Y., T. Kyoya, and T. Kawamoto, [1985], "Incremental theory of plasticity for rocks", *Proceedings of the 5th. International Conference on Numerical Methods in Geomechanics*, T. Kawamoto and Y. Ichikawa, Editors, pp. 451-462.
- Kroner, E., [1967], "Elasticity theory of materials with long range cohesive forces", *International Journal of Solid and Structures*, **3**, pp. 731-742.
- Lade, P., R. Nelson, and M. Ito, [1987], "Non-associated flow and stability of granular materials", *Journal of Engineering Mechanics, ASCE*, **113**, No. 9, pp. 1302-1318.
- Leroy, Y., A. Needleman, and M. Ortiz, [1988], "An overview of finite element methods for the analysis of strain localization", In *Cracking and Damage: Strain localization and size effect*", Ed. J. Mazars and Z.P Bazant, Elsevier Applied Science, pp. 269-294.
- Lo, K.Y., and C.F Lee, [1973], "Stress analysis and strain softening materials", *Geotechnique*, **23**, No. 1, pp. 1-11.
- Malvern, L.E., [1969], *Introduction to the Mechanics of a Continuous Medium*, Prentice-Hall, New-Jersey.

- Mandel, J., [1966], "Conditions de stabilité et postulat de Drucker"; *Proceedings of the IUTAM Conference on Rheology on Soil Mechanics*, J. Kravtchenko and P. Sirieys, Ed. Springer-Verlag.
- Melan, E., [1938] "Zur Plastizität des räumlichen Kontinuums", *Ingenieur-Archiv*, **9**, pp.116-126.
- Morgenstern, N.R., and J.S Tchalenko, [1967], "Microscopic structures in kaolin subjected to direct shear", *Geotechnique*, **17**, pp. 309-328
- Mühlhaus, H.B., Vardoulakis, I., [1987], "The thickness of shear bands in granular materials", *Geotechnique*, **37**, No. 3 pp. 271-283.
- Nayak, G.C., and O.C Zienkiewicz, [1972], "Elasto-plastic stress analysis: A generalization of various constitutive relations inducing strain-softening", *Int. J. Num. Meth. Engng.*, **5**, pp. 113-135.
- Needleman, A., [1987], "Material rate dependence and mesh sensitivity in localization problems", *Computer Methods in Applied Mechanics and Engineering*, **67**, pp.68-85.
- Ortiz, M., Y. Leroy and A. Needleman, [1987], "A finite element method for localized failure analysis", *Comp. Meth. in Appl. Mech. and Engng.* , **61**, pp. 189-214.
- Peck, R.B., [1967], "Stability of natural slopes", *Journal of the Soil Mechanics and Foundation Engineering Division, ASCE*, **93**, SM4, pp. 403-417.
- Pietruszczak, S.T., and Z. Mroz, [1981], "Finite element analysis of deformation of strain softening materials", *Int. J. Num. Meth. Engng.*, **10**, No. 17, pp. 327-334.
- Pietruszczak, S.T., and D.F.E Stolle, [1987], "Deformation of strain-softening materials, Part II: Modelling of strain softening response", *Computers and Geotechnics*, **4**, pp. 109-123.
- Prevost, J.H., and K. Hoeg, [1975a], "Effective stress-strain-strength model for soils", *Journal of the Geotechnical Engineering Division, GT3, ASCE*, pp. 259-278.

- Prevost, J.H., and K. Hoeg, [1975b], "Soil mechanics and plasticity analysis of strain softening", *Geotechnique*, **25**, No. 2, pp. 279-297.
- Rankine, W. [1857], "On the stability of loose earth", *Phil. Trans. Roy. Soc.*, London, **17**, Part 1, pp. 9-27.
- Read, H.E and G.P Hegemier, [1984], "Strain softening of rock, soil and concrete—a review article", *Mechanics of Materials*, **3**, No. 4, pp. 271-294.
- Rice, J.R., [1976], "The localization of plastic deformation", In *Theoretical and Applied Mechanics*, Ed. W.T Koiter, North-Holland, Amsterdam, pp. 207-220.
- Roscoe, K.H., [1970], "The influence of strains in soil mechanics", Tenth Rankine Lecture, *Geotechnique*, **20**, No. 2, pp. 129-170.
- Rosso, R., [1976], "A comparison of joint stiffness measurements in direct shear, triaxial and in-situ", *International J. Rock. Mech. Min. Sci. and Geomech. Abstr.*, **13**, pp. 167-172.
- Rowe, P.W., [1962], "The stress dilatancy relation for static equilibrium of an assembly of particles in contact.", *Proceedings of the Royal Society, Series A*, **269**, pp. 500-527.
- Rudnicki, J.W and J.R Rice.,[1975], "Conditions for the localization of deformation in pressure sensitive dilatant material", *J. Mech. Phys. Solids*, **23**, pp. 371-394.
- Rudnicki, J.W., [1977], "The inception of faulting in a rock mass with a weakened zone", *Journal of Geophysical Research*, **82**, No. 5, pp. 844-854.
- Sandler, I and J. Wright, [1984], "Summary of strain softening", *Theoretical foundations for large scale computations of non-linear material behaviour*, DARPA-NSF workshop, Ed. S. Nemat-Nasser, North Western University.

- Scarpelli, G., and D.M Wood, [1982], "Experimental observations of shear band pattern in direct shear tests". *IUTAM Symposium on Deformation and Failure of Granular Materials*, Delft, pp. 473-484.
- Schreyer, H.L, Z. Chen, [1986], "One-Dimensional softening with localization", *ASME Journal of Applied Mechanics*, **53**, No. 4, pp 791-797.
- Simo, J.C and R.L Taylor, [1985]. "Consistent tangent operators for rate-independent elasto-plasticity", *Comp. Meth. in Appl. Mech. and Eng.*, **48**, pp.101-118.
- Simo, J.C., [1988], "Strain softening and dissipation: A unification of approaches", In *Cracking and Damage: Strain localization and size effect*", Ed. J. Mazars and Z.P Bazant, Elsevier Applied Science, pp. 440-461.
- Skempton, A.W., [1964], "Long-term stability of clay slopes", *Geotechnique*, **14**, NO. 2, pp. 77-101.
- Sokolovski, V.V., [1965], *Statics of Granular Media*, London, Pergamon.
- Tanaka, T., Kawamoto, O., [1989], "Plastic collapse analysis of slopes of strain softening materials", *Proceedings of the 3rd. International Symposium on Numerical Models in Geomechanics [NUMOG III]*, Ed. S. Pietruszczak and G.N Pande, Elsevier Applied Science, pp.667-674.
- Tatsuoka, F., S. Nakamura, C.C Huang and K. Tani, [1990], "Strength anisotropy and shear band direction in plane strain tests of sand", *Soils and Foundations*, **30**, No. 1, pp. 35-54.
- Terzaghi, K., [1923], "Die Berechnung der Durchlassig Keitsziffer des Tones aus dem Verlauf der Hydrodynamischen Spannungserscheinungen", *Sitzber. Akad. Wiss. Wien*, **132**, 125.
- Thomas, T.Y., [1961], *Plastic Flow and Fracture in Solids*, Academic Press, New York.

- Triantafyllidis, N., and E.C. Aifantis, [1986], "A gradient approach to localization of deformation, I: Hyperelastic Materials", *Journal of Elasticity*, **16**, pp. 225-237.
- Truesdell, C. and R. Toupin, [1960], *The Classical Field Theories of Mechanics*, Handbuch der Physik, vol III/1, Springer.
- Vardoulakis, I., [1979], "Bifurcation analysis of the triaxial test on sand samples", *Acta Mechanica*, **32**, pp. 35-54.
- Vardoulakis, I., [1980], "Shear band inclination and shear modulus of sands in biaxial tests", *Int. J. Num. Anal. Meth. in Geomechanics*, **4**, pp. 103-119.
- Vardoulakis, I., M. Goldshieder, and G. Gudehus, [1978], "Formation of shear bands in sand bodies as a bifurcation problem". *Int. J. Num. Anal. Meth. in Geomechanics*, **2**, pp. 99-123.
- Vermeer, F.A., [1982]. "A simple shear band analysis using compliances", *IUTAM Symposium on Deformation and Failure of Granular Materials*, Delft, pp. 493-499.
- Yatomi, C., A. Yashima, A. Iizuka, and I. Sano, [1989], "General theory of shear bands formation by a non-coaxial Cam-Clay model", *Soils and Foundations*, **29**, No. 3, pp. 41-53.
- Yoshimi, Y., and T. Kishida, [1981], "A ring torsion apparatus for evaluation of friction between soil and metal surfaces", *Geotechnical Testing Journal*, GTJG00J, **4**, No. 4, pp.145-152.
- Zienkiewicz, O.C and K. Morgan, [1982], *Finite Elements and Approximation*, John Wiley and sons, New-York.
- Zienkiewicz, O.C and R.L Taylor, [1989], *The Finite Element Method*, Fourth Edition, Volume 1, Mc-Graw-Hill, New-York.

Appendix A

Derivation of Flow and Deformation Equations

A.1. Theory of mixtures

Consider a 2-phase medium in which the 2 phases interact so that their behaviours give average response. Let ρ_s and ρ_f represent respectively the density of the solid and fluid phases, $\rho^{(s)}$ and $\rho^{(f)}$ the corresponding relative densities (the ones we actually measure experimentally). Thus, the total density ρ can be defined as the sum of the densities of each constituent phase, i.e.

$$\rho = \rho^{(s)} + \rho^{(f)}, \quad (\text{A.1})$$

$$\rho^{(s)} = \frac{dM_s}{dV} = \frac{dM_s}{dV_s} \frac{dV_s}{dV} = \frac{dM_s}{dV_s} \frac{dV - dV_f}{dV} = (1 - n)\rho_s, \quad (\text{A.2})$$

$$\rho^{(f)} = \frac{dM_f}{dV} = \frac{dM_f}{dV_f} \frac{dV_f}{dV} = n\rho_f. \quad (\text{A.3})$$

Each constituent phase has to satisfy the mass balance equation, i.e.

$$\dot{\rho}^{(\alpha)} + \rho^{(\alpha)} \frac{\partial v_i^{(\alpha)}}{\partial x_i} = 0, \quad (\text{A.4})$$

in which (α) stands for the fluid phase and the superimposed dot represents the material derivative. This mass balance or continuity condition written for the solid phase becomes:

$$\frac{\partial(1-n)\rho_s}{\partial t} + \frac{\partial(1-n)\rho_s v_i^{(s)}}{\partial x_i} = 0. \quad (\text{A.5})$$

Expanding Eq. (A.5) and using the operator $\frac{d(\cdot)}{dt} = \frac{\partial(\cdot)}{\partial t} + v_i \frac{\partial(\cdot)}{\partial x_i}$ the following is

obtained:

$$\frac{dn}{dt} = \frac{(1-n)}{\rho_s} \left[\frac{d\rho_s}{dt} + \frac{\partial v_i^{(s)}}{\partial x_i} \right], \text{ for } \rho_s \neq 0. \quad (\text{A.6})$$

Lets define a bulk relative fluid velocity q_i as

$$v_i = n(v_i^{(f)} - v_i^{(s)}). \quad (\text{A.7})$$

The continuity equation for the fluid phase can be written as

$$\frac{\partial(n\rho_f)}{\partial t} + \frac{\partial(n\rho_f v_i^{(f)})}{\partial x_i} = 0. \quad (\text{A.8})$$

Using Eq. (A.7) to eliminate $v_i^{(f)}$ and with the aid of Eq. (A.6), one gets after some algebra

$$-\frac{1}{\rho_f} \frac{\partial(\rho_f v_i)}{\partial x_i} = (1-n) \frac{1}{\rho_s} \frac{d\rho_s}{dt} + n \frac{1}{\rho_f} \frac{d\rho_f}{dt} + \frac{\partial v_i^{(s)}}{\partial x_i}. \quad (\text{A.9})$$

But

$$\frac{\partial v_i^{(s)}}{\partial x_i} = \frac{\partial}{\partial x_i} \frac{du_i}{dt} = \frac{d}{dt} \left(\frac{\partial u_i}{\partial x_i} \right) = \dot{\epsilon}_{ii}. \quad (\text{A.10})$$

Darcean flow can be written as

$$v_i = -k_{ij} \left[\frac{\partial \pi}{\partial x_j} + \rho_f g_j \right], \quad (\text{A.11})$$

in which π is the pore fluid pressure and g_j is the j th. component of gravity. When Eq. (A.11) is substituted into (A.9), one gets:

$$\frac{1}{\rho_f} \frac{\partial}{\partial x_i} \rho_f \left[k_{ij} \frac{\partial \pi}{\partial x_j} + \rho_f g_j \right] = (1-n) \frac{1}{\rho_s} \frac{d\rho_s}{dt} + n \frac{1}{\rho_f} \frac{d\rho_f}{dt} + \dot{\epsilon}_{ii}. \quad (\text{A.12})$$

For incompressible solid and fluid phases, Eq. (A.12) obviously reverts to the following well-known form:

$$\frac{\partial}{\partial x_i} \left[k_{ij} \frac{\partial \pi}{\partial x_j} + \rho_f g_j \right] - \dot{\epsilon}_{ii} = 0. \quad (\text{A.13})$$

A.2. Flow equations

• Strong form

Consider the fluid flow described in Chapter 4 for a discontinuous medium as previously illustrated in Figure 4.2. The strong form (S) or the classical statement of the flow problem is mathematically represented by physical laws that govern the phenomenon, i.e.

• Mass conservation:

$$v_{i,i} + \dot{u}_{i,i} = 0. \quad (\text{A.14})$$

• **Darcean flow:**

$$v_i = -k_{ij}(\pi_j + \gamma_j). \quad (\text{A.15})$$

• **Boundary conditions:**

$$\pi(\mathbf{x}) = \bar{\pi}(\mathbf{x}) \text{ on } \Gamma_\pi, \quad (\text{A.16})$$

$$\bar{q} = v_i n_i \text{ on } \Gamma_q, \quad (\text{A.17})$$

$$[v_i^{(1)} - v_i^{(2)}]n_i^{(1)} = -\dot{g}_i n_i^{(1)} + \bar{q}_{sb} \text{ on } \Gamma_{sb}. \quad (\text{A.18})$$

If pore fluids are principal unknowns, then the equation of mass balance combined with Darcean flow becomes:

$$[k_{ij}(\pi_j + \gamma_j)]_{,i} - \dot{u}_{i,i} = 0 \text{ in } \Omega_1 \cup \Omega_2, \quad (\text{A.19})$$

$$\pi(\mathbf{x}) = \bar{\pi}(\mathbf{x}) \text{ on } \Gamma_\pi, \quad (\text{A.20})$$

$$-k_{ij}(\pi_j + \gamma_j)n_i = \bar{q}, \quad (\text{A.21})$$

$$[k_{ij}^{(2)}(\pi_j^{(2)} + \gamma_j) - k_{ij}^{(1)}(\pi_j^{(1)} + \gamma_j)]n_i^{(1)} = -\dot{g}_i n_i^{(1)} + \bar{q}_{sb} \text{ on } \Gamma_{sb}. \quad (\text{A.22})$$

• **Weak form : Problem statement:**

The weak form (W) or the variational counterpart of (S) involves the following: find $\pi(\mathbf{x})$ such that Eq. (A.19) is satisfied everywhere inside $\Omega = \Omega_1 \cup \Omega_2$ with boundary conditions specified by Eqs. (A.20) to (A.22). Note that the pore fluid π is discontinuous across the shear band interface.

Variational statement:

A Galerkin approximation of the problem is obtained by posing the variational problem on a finite dimensional subspace \mathfrak{H} of the space of hydraulically admissible functions, i.e. those which satisfy the homogeneous essential boundary conditions and are smooth enough. In particular, \mathfrak{H} is defined as

$$\mathfrak{H} = \{ \pi^* = \pi^*(\mathbf{x}) / \bar{\pi}^* = 0 \text{ on } \Gamma_\pi \}. \quad (\text{A.23})$$

The differential equation in (A.6) with associated boundary conditions can be cast in an integral form by multiplying it by the admissible pore fluid field $\pi^*(\mathbf{x})$ in order to obtain a weak form. By virtue of the weighted residual method which aims at minimizing the error on an average weighted sense,

$$\int_{\Omega} [k_{ij}(\pi_{,j} + \gamma_j)]_{,i} \delta\pi^* \, d\Omega + \int_{\Omega} \dot{u}_{i,i} \delta\pi^* \, d\Omega = 0. \quad (\text{A.24})$$

Noting that

$$[k_{ij}(\pi_{,j} + \gamma_j)]_{,i} \delta\pi^* = [k_{ij}(\pi_{,j} + \gamma_j)\delta\pi^*]_{,i} - k_{ij}(\pi_{,j} + \gamma_j)\delta\pi^*_{,i}, \quad (\text{A.25})$$

integration by parts yields:

$$\int_{\Omega} k_{ij}(\pi_{,j} + \gamma_j)\delta\pi^*_{,i} \, d\Omega + \int_{\Omega} \dot{u}_{i,i} \delta\pi^* \, d\Omega = \int_{\Gamma_q \cup \Gamma_b} k_{ij}(\pi_{,j} + \gamma_j)n_i \, d\Gamma. \quad (\text{A.26})$$

This boundary integral on the right hand side of the above equation can be broken down into the following components, with the aid of Eq.(A.15)

$$-\int_{\Gamma_q} v_i n_i \delta\pi^* d\Gamma + \int_{\Gamma_{ab}} [v_i^{(1)} n_i^{(1)} + v_i^{(2)} n_i^{(2)}] \delta\pi^* d\Gamma. \quad (\text{A.27})$$

Considering $n_i^{(1)} = -n_i^{(2)}$, the above integral becomes

$$-\int_{\Gamma_q} \bar{q} \delta\pi^* d\Gamma - \int_{\Gamma_{ab}} [-g_i n_i^{(1)} + \bar{q}_{ab}] \delta\pi^* d\Gamma, \quad (\text{A.28})$$

which yields boundary conditions (A.17) and (A.18). The final form of the Galerkin expression emerges as:

$$\begin{aligned} \int_{\Omega} k_{ij} \pi_{,j} \delta\pi_{,i}^* d\Omega + \int_{\Omega} \dot{u}_{i,i} \delta\pi^* d\Omega - \int_{\Gamma_{ab}} \dot{g}_i n_i^{(1)} d\Gamma = & - \int_{\Omega} k_{ij} \gamma_j \delta\pi_{,i}^* d\Omega - \int_{\Gamma_q} \bar{q} \delta\pi^* d\Gamma \\ & - \int_{\Gamma_{ab}} \bar{q}_{ab} \delta\pi^* d\Gamma. \end{aligned} \quad (\text{A.29})$$

Appendix B

Numerical Implementation

B.1. Evaluation of composite element stiffness matrix

Consider the expanded form of the stiffness matrix as obtained from the discretization of the variational principle in Chapter 4. Fig. B.1. shows the typical size of the stiffness matrix for a QD4 type of element and the different partitions which have to be computed during a numerical analysis.

Explicit forms of the compatibility matrices $\mathbf{B}^{(\alpha)}$, $\mathbf{B}^{(\beta)}$, constitutive tensors \mathbf{L} and $\boldsymbol{\eta}$ as well as the geometrical location of the discontinuity are required for the numerical integration of the various stiffnesses in the composite stiffness matrix. In plane strain conditions, the compatibility matrix $\mathbf{B}^{(\alpha)}$ is traditionally given by

$$[\mathbf{B}_i^{(\alpha)}]^{(e)} = \begin{bmatrix} \left(\frac{\partial N_i^{(\alpha)}}{\partial x}\right)^{(e)} & 0 \\ 0 & \left(\frac{\partial N_i^{(\alpha)}}{\partial y}\right)^{(e)} \\ \left(\frac{\partial N_i^{(\alpha)}}{\partial y}\right)^{(e)} & \left(\frac{\partial N_i^{(\alpha)}}{\partial x}\right)^{(e)} \end{bmatrix} \text{ with } i = 1, \text{ node,} \quad (\text{B.1})$$

in which node takes the value of 4 for a quadrilateral element and 3 for a constant strain triangular element.

If one envisions a linear variation of slip displacement along the shear band by having two localized nodes, the compatibility matrix $\mathbf{B}^{(\beta)}$ for the discontinuity is

$$[\mathbf{B}_i^{(\beta)}]^{(e)} = \begin{bmatrix} \left(\frac{\partial N_i^{(\beta)}}{\partial x}\right)^{(e)} & 0 \\ 0 & \left(\frac{\partial N_i^{(\beta)}}{\partial y}\right)^{(e)} \\ \left(\frac{\partial N_i^{(\beta)}}{\partial y}\right)^{(e)} & \left(\frac{\partial N_i^{(\beta)}}{\partial x}\right)^{(e)} \end{bmatrix} \text{ for which } i = 1, 2. \quad (\text{B.2})$$

The *discontinuous* shape functions $N_i^{(\beta)}$ whose derivatives exist on either side of the discontinuity front were defined in Chapter 4. The form of the shape matrix $(\mathbf{N}^{(\beta)})^e$ which is suitable for a numerical implementation is

$$(\mathbf{N}^{(\beta)})^e = \begin{bmatrix} N_1^{(\beta)} & 0 & N_2^{(\beta)} & 0 \\ 0 & N_1^{(\beta)} & 0 & N_2^{(\beta)} \end{bmatrix}. \quad (\text{B.3})$$

For plane strain elasticity, the constitutive tensor \mathbf{L} and $\boldsymbol{\eta}$ are simply

$$\mathbf{L} = \frac{E}{(1+\nu)(1-2\nu)} \begin{bmatrix} (1-\nu) & \nu & 0 \\ \nu & (1-\nu) & 0 \\ 0 & 0 & \frac{(1-\nu)}{2} \end{bmatrix}; \quad (\text{B.4})$$

$$\boldsymbol{\eta}_{\nu} = \begin{bmatrix} \eta_{xx} & \eta_{xx} \\ \eta_{xx} & \eta_{xx} \end{bmatrix}. \quad (\text{B.5})$$

In a more general case, the tensors \mathbf{L} and $\boldsymbol{\eta}$ would take the classical elasto-plastic form similar to that presented in Eq. (3.11).

B.2. Quadrature rule for element stiffness integration

A numerical quadrature scheme that accommodates for the proposed displacement and strain fields must be considered in order to achieve accurate results and handle the effect of the localized zone as well. A standard quadrature scheme, say 2x2 Gauss integration will not capture the presence of the jump inside the element provided a large number of quadrature points is used.

Consider the QD4 element with the embedded shear band as shown in Fig. B.2. The sought effect is to have strains localized along the shear band and non-localized strains in regions outside the band. A normal 2x2 Gauss integration scheme will result in the smearing of the displacement field jump over the element so that a bilinear distribution similar to the classical Q4 element will be obtained rather than a distribution with an intrinsic jump.

The integration scheme adopted herein guarantees accuracy in capturing the jump inside the element by using standard numerical integration over separate domains demarcated by the shear band boundary, see Fig. B.3. This procedure inevitably introduces a large number of integration points, i.e. 10 in all for a QD4 element (4 over each domain adjacent to the shear band and 2 other ones along the shear band itself).

A typical integral over the area of the element for a discontinuous function $f(\mathbf{x})$ is given by

$$I = \int_{\Omega} f(\mathbf{x}) \, d\Omega. \quad (\text{B.6})$$

Since $f(x)$ takes up different values depending on whether x is in region Ω^{e+} or Ω^{e-} , the integral has to be discretized over each separate domain, i.e.

$$I = \sum_{i=1}^{NGAUS} \sum_{j=1}^{NGAUS} f^+(r_i, s_j) (\det J)_{ij} (\det J^*)_{ij} w_i w_j + \sum_{i=1}^{NGAUS} \sum_{j=1}^{NGAUS} f^-(r_i, s_j) (\det J)_{ij} (\det J^*)_{ij} w_i w_j. \quad (B.7)$$

(ξ_i, η_j) are the coordinates in the local reference system, (r_i, s_j) the coordinates in the sub-local reference system, J the Jacobian of the transformation between the local and global systems, J^* the Jacobian of the transformation between the sub-local and local coordinates and w_i the weights, see Fig. B.3 for details.

The different constituent stiffnesses of the composite matrix given in Fig. B.3 are evaluated on the basis of the foregoing scheme.

- Bulk stiffness $\mathbf{K}_{\Omega\Omega}^{(e)}$

$$\begin{aligned} \mathbf{K}_{\Omega\Omega}^{(e)} &= \int_{\Omega^e} \mathbf{B}^{(\alpha)T}(x, y) : \mathbf{L}(x, y) : \mathbf{B}^{(\alpha)}(x, y) \, dx \, dy \\ &= \int_{\Omega^{e+}} \mathbf{B}^{(\alpha)+T}(\xi, \eta) : \mathbf{L}(\xi, \eta) : \mathbf{B}^{(\alpha)+}(\xi, \eta) \det J \, d\xi \, d\eta \\ &\quad + \int_{\Omega^{e-}} \mathbf{B}^{(\alpha)-T}(\xi, \eta) : \mathbf{L}(\xi, \eta) : \mathbf{B}^{(\alpha)-}(\xi, \eta) \det J \, d\xi \, d\eta. \end{aligned} \quad (B.8)$$

When integrated in the local system,

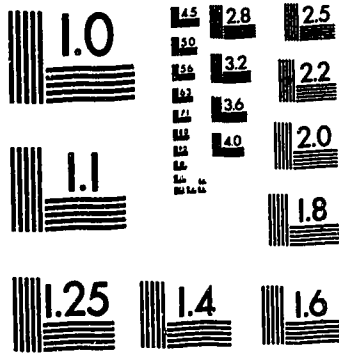
$$\mathbf{K}_{\Omega\Omega}^{(e)} = \sum_i \sum_j \mathbf{B}^{(\alpha)T}(\xi_i, \eta_j) : \mathbf{L}(\xi_i, \eta_j) : \mathbf{B}^{(\alpha)}(\xi_i, \eta_j) (\det J)_{ij} w_i w_j. \quad (B.9)$$

Note that $\mathbf{B}^{(\alpha)+}$ and $\mathbf{B}^{(\alpha)-}$ are the same and the integration may be accomplished in the (ξ, η) space.

3

of/de

3



MICROCOPY RESOLUTION TEST CHART
NATIONAL BUREAU OF STANDARDS
STANDARD REFERENCE MATERIAL 1010a
(ANSI and ISO TEST CHART No. 2)

- Bulk - shear band interaction stiffnesses $\mathbf{K}_{\Omega S}^{(\epsilon)}$ and $\mathbf{K}_{S\Omega}^{(\epsilon)}$

The numerical integration of stiffness terms $\mathbf{K}_{\Omega S}^{(\epsilon)}$ and $\mathbf{K}_{S\Omega}^{(\epsilon)}$ is performed in the same fashion as in Eq. (B.6). It is noted that the symmetry $\mathbf{K}_{\Omega S}^{(\epsilon)} = \mathbf{K}_{S\Omega}^{(\epsilon)T}$ is destroyed as soon as \mathbf{L} ceases to be symmetric.

$$\begin{aligned} \mathbf{K}_{\Omega S}^{(\epsilon)} = & \sum_i \sum_j \mathbf{B}^{(\alpha)+T}(r_i, s_j) : \mathbf{L}(r_i, s_j) : \mathbf{B}^{(\beta)+}(r_i, s_j) (\det J)_{ij} (\det J^{*+})_{ij} w_i w_j \\ & + \sum_i \sum_j \mathbf{B}^{(\alpha)-T}(r_i, s_j) : \mathbf{L}(r_i, s_j) : \mathbf{B}^{(\beta)-}(r_i, s_j) (\det J)_{ij} (\det J^{*-})_{ij} w_i w_j, \end{aligned}$$

$$\forall (r_i, s_j) \in \Omega^{\epsilon+} \text{ or } \Omega^{\epsilon-}.$$

(B.10)

- Global shear band stiffness $\mathbf{K}_{SS}^{(\epsilon)}$

$$\begin{aligned} \mathbf{K}_{SS}^{(\epsilon)} = & \sum_i \sum_j \mathbf{B}^{(\beta)+T}(r_i, s_j) : \mathbf{L}(r_i, s_j) : \mathbf{B}^{(\beta)+}(r_i, s_j) (\det J)_{ij} (\det J^{*+})_{ij} w_i w_j \\ & + \sum_i \sum_j \mathbf{B}^{(\beta)-T}(r_i, s_j) : \mathbf{L}(r_i, s_j) : \mathbf{B}^{(\beta)-}(r_i, s_j) (\det J)_{ij} (\det J^{*-})_{ij} w_i w_j \\ & + \int_{\Gamma^{\epsilon}} \mathbf{N}^{(\beta)T} [\boldsymbol{\eta}]_{n \rightarrow s} d\Gamma. \end{aligned}$$

(B.11)

B.3. Calculation of cartesian derivatives of shape functions

The dual transformation described in the previous section, i.e.

$$(x, y) \xrightarrow{J} (\xi, \eta) \xrightarrow{J^*} (r, s)$$

requires the evaluation of two Jacobians which are

$$J = \begin{bmatrix} \frac{\partial x}{\partial \xi} & \frac{\partial y}{\partial \xi} \\ \frac{\partial x}{\partial \eta} & \frac{\partial y}{\partial \eta} \end{bmatrix}, J^* = \begin{bmatrix} \frac{\partial \xi}{\partial r} & \frac{\partial \eta}{\partial r} \\ \frac{\partial \xi}{\partial s} & \frac{\partial \eta}{\partial s} \end{bmatrix}. \quad (\text{B.12})$$

The cartesian derivatives of the shape functions are calculated by multiplying the local derivatives by the appropriate Jacobian matrices. Typically in the local (ξ, η) reference axes

$$\frac{\partial N_i^{(j)}}{\partial x} = \frac{\partial N_i^{(j)}}{\partial \xi} \frac{\partial \xi}{\partial x} + \frac{\partial N_i^{(j)}}{\partial \eta} \frac{\partial \eta}{\partial x}, \quad (\text{B.13})$$

$$\frac{\partial N_i^{(j)}}{\partial y} = \frac{\partial N_i^{(j)}}{\partial \xi} \frac{\partial \xi}{\partial y} + \frac{\partial N_i^{(j)}}{\partial \eta} \frac{\partial \eta}{\partial y}, \quad (\text{B.14})$$

or

$$\begin{Bmatrix} \frac{\partial N_i^{(j)}}{\partial x}(\xi, \eta) \\ \frac{\partial N_i^{(j)}}{\partial y}(\xi, \eta) \end{Bmatrix} = \begin{bmatrix} \frac{\partial \xi}{\partial x} & \frac{\partial \eta}{\partial x} \\ \frac{\partial \xi}{\partial y} & \frac{\partial \eta}{\partial y} \end{bmatrix} \begin{Bmatrix} \frac{\partial N_i^{(j)}}{\partial \xi} \\ \frac{\partial N_i^{(j)}}{\partial \eta} \end{Bmatrix}, \quad (\text{B.15})$$

in which $j = \alpha$ or β refers to continuous and discontinuous components respectively. The cartesian derivatives in the (r, s) space are obtained by evaluating the Jacobian and shape function derivatives at points $\xi(r, s)$ and $\eta(r, s)$, i.e.

$$\begin{aligned} \begin{Bmatrix} \frac{\partial N_i^{(j)}}{\partial x}(r,s) \\ \frac{\partial N_i^{(j)}}{\partial y}(r,s) \end{Bmatrix} &= \begin{bmatrix} \frac{\partial \xi}{\partial x}(r,s) & \frac{\partial \eta}{\partial x}(r,s) \\ \frac{\partial \xi}{\partial y}(r,s) & \frac{\partial \eta}{\partial y}(r,s) \end{bmatrix} \begin{Bmatrix} \frac{\partial N_i^{(j)}}{\partial \xi}(\xi(r,s), \eta(r,s)) \\ \frac{\partial N_i^{(j)}}{\partial \eta}(\xi(r,s), \eta(r,s)) \end{Bmatrix} \\ &= [J]_{\xi(r,s), \eta(r,s)}^{-1} \begin{Bmatrix} \frac{\partial N_i^{(j)}}{\partial \xi} \\ \frac{\partial N_i^{(j)}}{\partial \eta} \end{Bmatrix}. \end{aligned}$$

(B.16)

It is noted that J and J^* describe the geometry of the element and may be evaluated using different shape functions such that the transformation does not need to be isoparametric in the true sense. It would indeed be either sub-parametric, i.e the geometric mapping is of a lower degree basis or a subset of the interpolant for displacement, or super-parametric if the geometric map is of a higher order than the interpolant as in the case of a linear variation of slip displacements along a curved shear band.

B.4. Calculation of interface stiffness

Consider the geometrical representation of the shear band oriented in an arbitrary manner inside the element as shown in Fig. B.4. Call θ the inclination of the shear band axis with respect to the global x axis. The local coordinate system attached to the shear band are defined by (n,s) .

Since during the discretization process, a linear variation of slip displacement \mathbf{g} was prescribed within the element and along the discontinuity line Γ_s , i.e

$$\mathbf{g}(\xi) = \frac{(1-\xi)}{2} \bar{\mathbf{g}}_1 + \frac{(1+\xi)}{2} \bar{\mathbf{g}}_2, \quad \xi \in \Gamma_s, \quad (\text{B.17})$$

with $\bar{\mathbf{g}}_1$ and $\bar{\mathbf{g}}_2$ the slips vector at localized nodes 1 and 2 respectively. The incremental slip displacement vector in the (n,s) system anywhere along Γ_s becomes

$$\begin{Bmatrix} \Delta g_s \\ \Delta g_n \end{Bmatrix} = \frac{1}{2} \begin{bmatrix} (1-\xi) & 0 & (1+\xi) & 0 \\ 0 & (1-\xi) & 0 & (1+\xi) \end{bmatrix} \begin{Bmatrix} \Delta \bar{g}_{s1} \\ \Delta \bar{g}_{n1} \\ \Delta \bar{g}_{s2} \\ \Delta \bar{g}_{n2} \end{Bmatrix} \quad (\text{B.18})$$

In compact form, the incremental slip displacements in the (n,s) axes is

$$\Delta \mathbf{g} = \mathbf{N}^* \cdot \Delta \bar{\mathbf{g}}. \quad (\text{B.19})$$

The interface stiffness term \mathbf{K}_{ss}^* in the discretized FEM equations, see last term in Eq.(B.11), refers to the global axes (x,y) . Since the contact constitutive tensor $\boldsymbol{\eta}$ is expressed in $s-n$ axes, it has to be pre and post multiplied by the appropriate transformation matrix \mathbf{A} which is

$$\mathbf{A} = \begin{bmatrix} [\mathbf{a}] & [0] \\ [0] & [\mathbf{a}] \end{bmatrix}, \quad (\text{B.20})$$

with

$$[\mathbf{a}] = \begin{bmatrix} \cos \theta & \sin \theta \\ -\sin \theta & \cos \theta \end{bmatrix}. \quad (\text{B.21})$$

Since for a linear shear band, \mathbf{A} remains constant, then the interface stiffness \mathbf{K}_{ss}^* in the $x-y$ reference frame is simply

$$K_{ss(x-y)}^* = \int_{\Gamma^e} \mathbf{N}^{(\beta)T} : \boldsymbol{\eta} : \mathbf{N}^{(\beta)} \, d\Gamma = \mathbf{A}^T \left[\int_{\Gamma^e} \mathbf{N}^{*T} : \boldsymbol{\eta}_{(s-n)} : \mathbf{N}^* \, d\Gamma \right] \mathbf{A}. \quad (\text{B.22})$$

B.5. Evaluation of load vectors

The load terms in the discretized variational principle comprise two basic components, namely:

- Load emanating from the continuous component

$$\begin{aligned} \Delta f_{\Omega} &= \int_{\Omega^e} \mathbf{N}^{(\alpha)T} \Delta f \, d\Omega + \int_{\Gamma_{\sigma}^e} \mathbf{N}^{(\alpha)T} \Delta \bar{\mathbf{T}} \, d\Gamma \\ &= \sum_{i=1}^{NGAUS} \sum_{j=1}^{NGAUS} \mathbf{N}^{(\alpha)T}(\xi_i, \eta_j) \Delta f(\xi_i, \eta_j) w_i w_j (\det J)_{ij} \\ &\quad + \sum_{j=1}^{NGAUS} \mathbf{N}^{(\alpha)T}(\xi_i) \Delta \bar{\mathbf{T}}(\xi_i) \left[\left(\frac{\partial N_j^{(\alpha)}}{\partial \xi} x_j \right)^2 + \left(\frac{\partial N_j^{(\alpha)}}{\partial \xi} y_j \right)^2 \right]^{1/2} w_i. \end{aligned}$$

The computations involved in the above expression are straightforward since they do not include any discontinuous shape functions.

- Load emanating from the discontinuous component

$$\Delta f_s = \int_{\Omega^e} \mathbf{N}^{(\beta)T} \Delta f \, d\Omega + \int_{\Gamma_{\sigma}^e} \mathbf{N}^{(\beta)T} \Delta \bar{\mathbf{T}} \, d\Gamma.$$

The above load expression describes the discontinuous contribution term which has to be added to the boundary loads. It effectively connects the boundary to the discontinuity surface as long as the boundary is part of a shear band element.

The first contribution, i.e. the volume integral over the element domain is integrated by means of the quadrature rule introduced in Section B.2 and results in

$$\int_{\Omega^e} \mathbf{N}^{(\beta)^T} \cdot \Delta \mathbf{f} \, d\Omega = \sum_i \sum_j \mathbf{N}^{(\beta)^+}(r_i, s_j) \Delta \mathbf{f}(r_i, s_j) (\det J^{*+})_{ij} w_i w_j \\ + \sum_i \sum_j \mathbf{N}^{(\beta)^-}(r_i, s_j) \Delta \mathbf{f}(r_i, s_j) (\det J^{*-})_{ij} w_i w_j.$$

The second contribution which is a surface integral will have to be evaluated whenever the load is applied along an edge which is crossed by the shear band, see Fig. B.5. Accordingly,

$$\int_{\Gamma_\sigma^*} \mathbf{N}^{(\beta)^T} \cdot \Delta \bar{\mathbf{T}} \, d\Gamma = \int_{\Gamma_\sigma^{*+}} \mathbf{N}^{(\beta)^+T} \cdot \Delta \bar{\mathbf{T}} \, d\Gamma + \int_{\Gamma_\sigma^{*-}} \mathbf{N}^{(\beta)^-T} \cdot \Delta \bar{\mathbf{T}} \, d\Gamma \\ = \sum_{i=1}^{NGAUS} \mathbf{N}^{\beta^+}(r_i(\xi_p, \eta_p)) \Delta \bar{\mathbf{T}}(r_i) \left[\left(\frac{\partial N_j^*}{\partial \xi} x_j \right)^2 + \left(\frac{\partial N_j^*}{\partial \xi} y_j \right)^2 \right]^{1/2} w_i \\ + \sum_{i=1}^{NGAUS} \mathbf{N}^{\beta^-}(r_i(\xi_p, \eta_p)) \Delta \bar{\mathbf{T}}(r_i) \left[\left(\frac{\partial N_j^*}{\partial \xi} x_j \right)^2 + \left(\frac{\partial N_j^*}{\partial \xi} y_j \right)^2 \right]^{1/2} w_i,$$

where N_j^* is either a linear or quadratic interpolation function for the mapping of (x, y) onto local coordinates ξ . x_j and y_j are the coordinates which define the boundary of the domains along the edge.

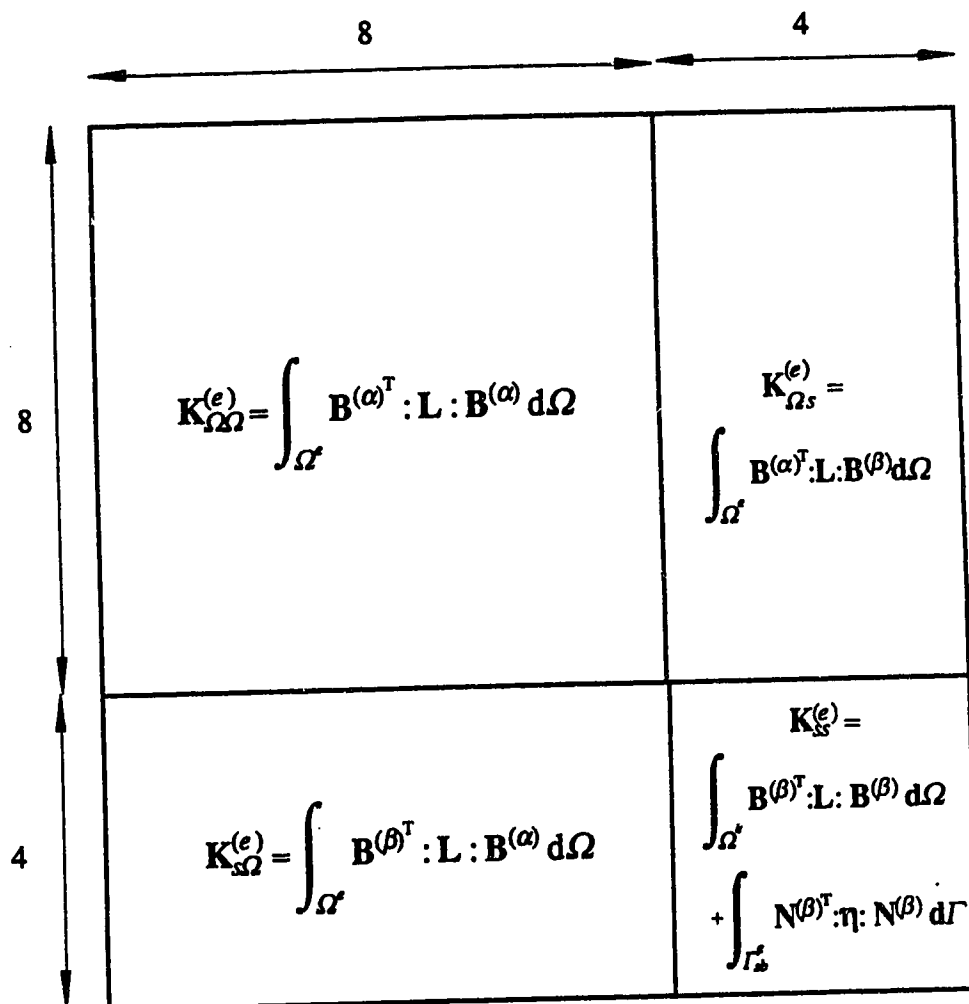


Figure B.1 Structure of typical stiffness matrix for a shear band element

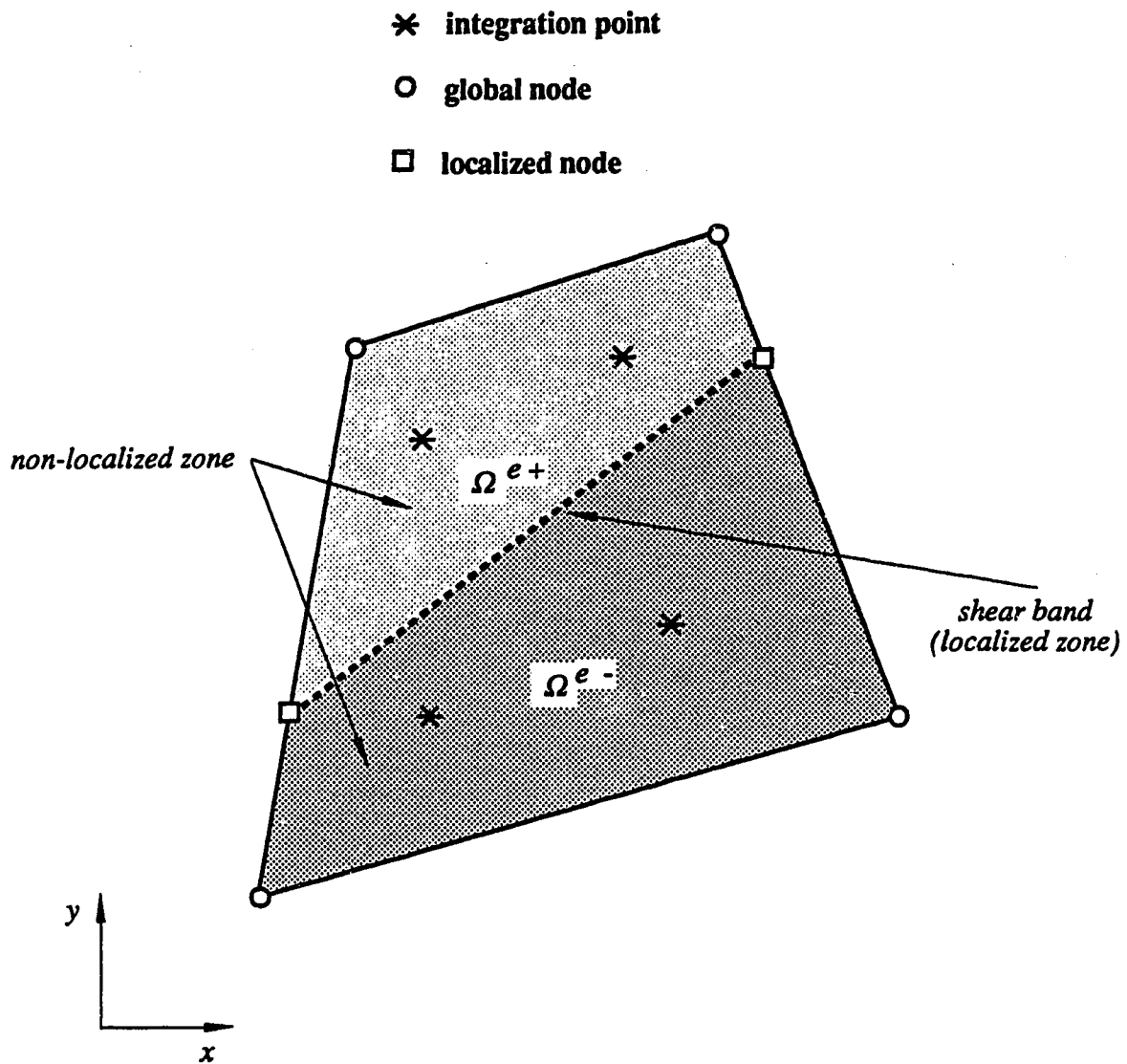


Figure B.2 Smearing effect for normal quadrature rule

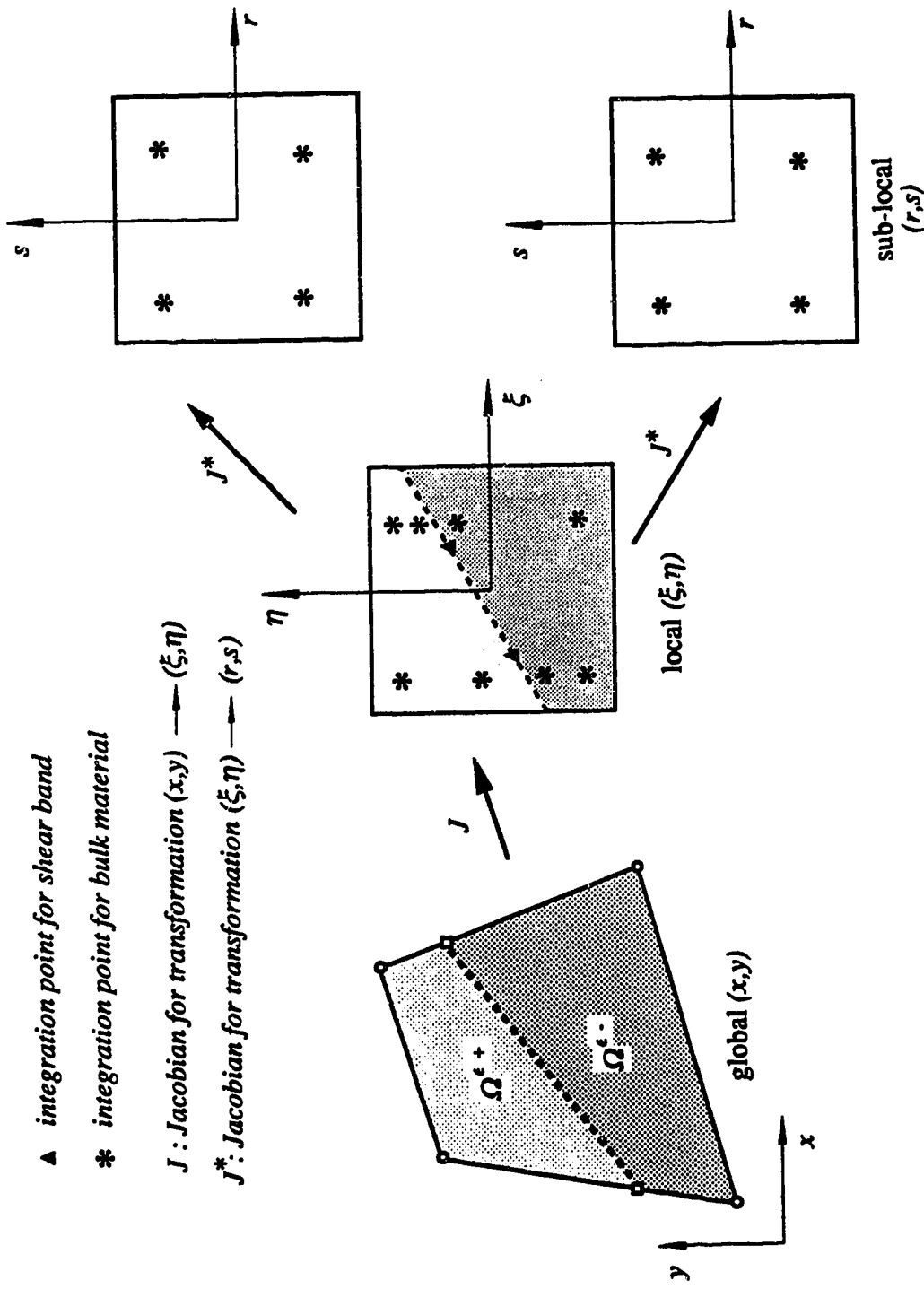


Figure B.3 Dual mapping technique for numerical integration

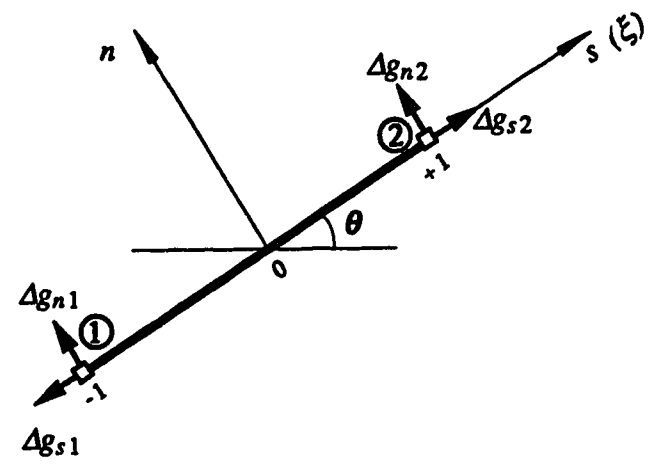
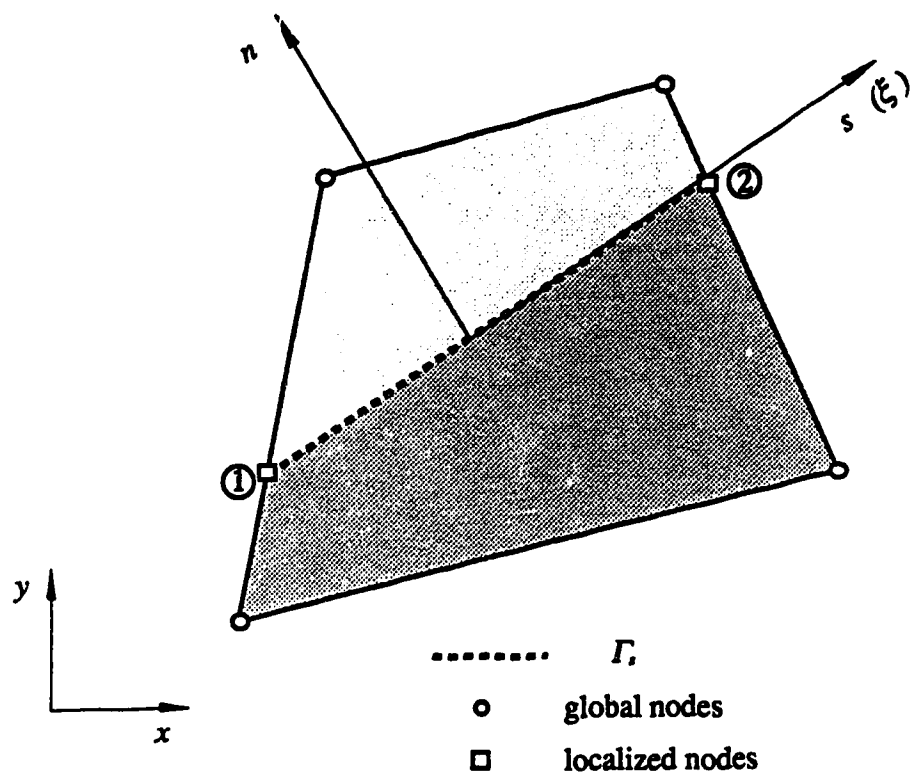


Figure B.4 Shear band geometry in global and local coordinate systems

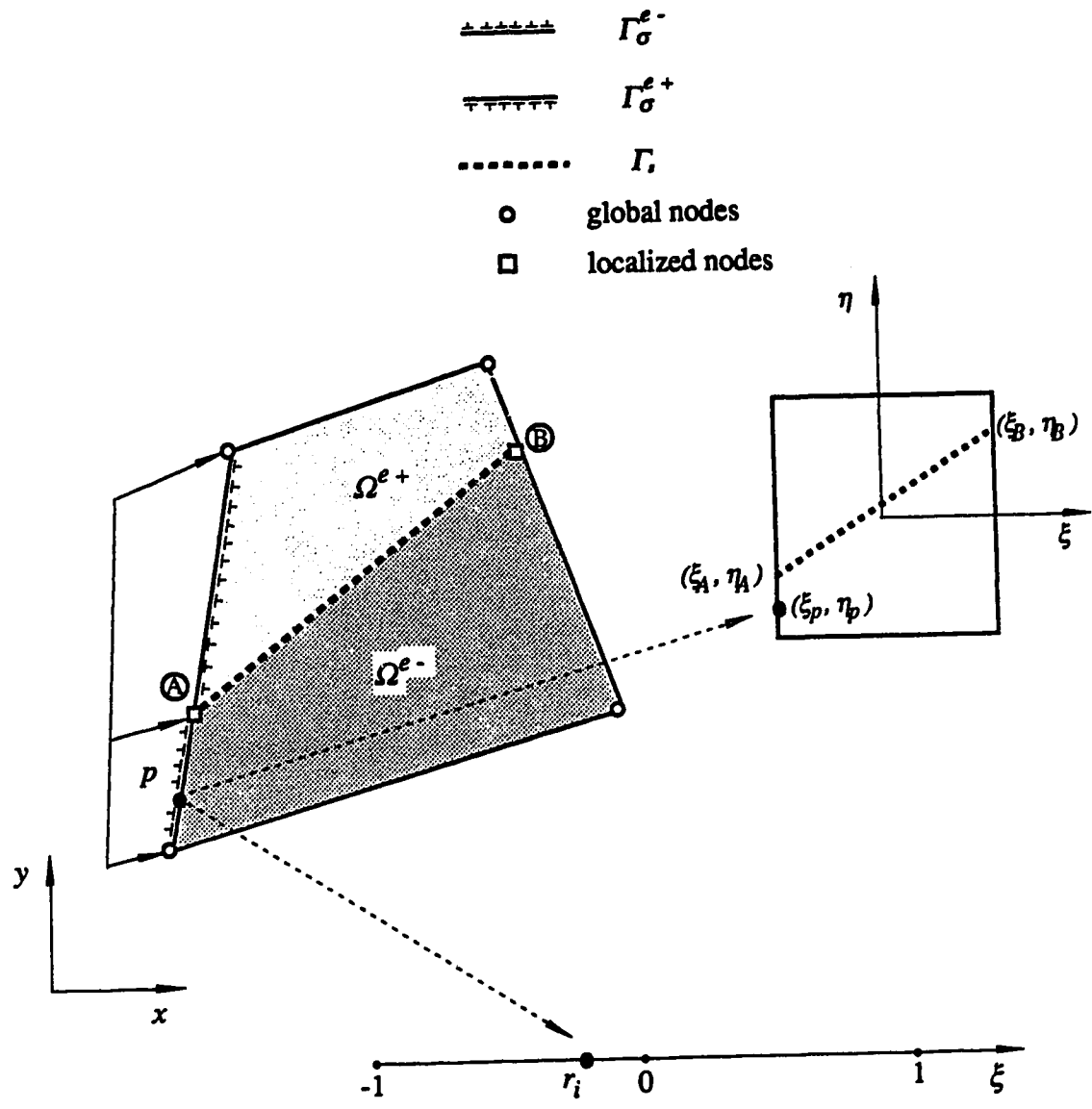


Figure B.5 Integration of loads along a discontinuous edge